TRANSIENT AND PERMANENT WAVEGUIDE EFFECTS IN ELECTRON-BEAM-PUMPED SEMICONDUCTOR LASERS

By

FRANCOIS LOUIS GOUIN, B.Sc.

A Thesis

Submitted to the School of Graduate Studies

in Partial Fulfilment of the Requirements

for the Degree

Doctor of Philosophy

McMaster University

September 1978

TRANSIENT WAVEGUIDE EFFECTS IN E-B-P SEMICONDUCTOR LASERS

DOCTOR OF PHILOSOPHY (1978)
(Physics)

McMASTER UNIVERSITY
Hamilton, Ontario

TITLE: Transient and Permanent Waveguide Effects in Electron-Beam-Pumped Semiconductor Lasers

AUTHOR: François Louis Gouin, B.Sc. (McGill University)

SUPERVISORS: Professor J. Shewchun
and Professor B.K. Garside

NUMBER OF PAGES: xii, 139

ABSTRACT

Most semiconductor laser configurations have an active region width comparable to the wavelength of the radiation giving rise to potentially important diffraction effects. In this work, optically confining mechanisms which can affect the magnitude of those diffraction effects are investigated in electron-beam-pumped GaAs bulk material and GaInAs hetero-epitaxial layers of various thicknesses.

One major aspect of the laser behaviour is the time delay between the start of the excitation and the onset of lasing. It has been reported that various semiconductor lasers can exhibit time delays to threshold which exceed by as much as two orders of magnitude the time required for the gain or the radiation to build up within the resonator. In the first part of this thesis, the dependence of the time delays on the electron-beam voltage and current is studied experimentally and theoretically in GaAs bulk material. A model is proposed which accounts for the long time delays observed on the basis of transient waveguiding. According to this model, there is a growing refractive index difference between the active region and the underlying passive region which progressively confines the radiation thereby reducing the cavity losses and eventually bringing

about lasing threshold. The spatial and temporal variations of the refractive index are attributed to corresponding variations in the temperature and the gain. As an integral part of this model, minority carrier concentration and temperature profiles resulting from the differential energy loss profile of the electron beam are derived.

To test the above hypothesis, the measurements were repeated on GaInAs hetero-epitaxial layers. Incorporated in such structure is a permanent refractive index difference between the epitaxial layer and the substrate which confines the radiation within the epitaxial layer. As suggested by the model, for layer thicknesses of the order of the electron-beam penetration depth, only short time delays to threshold are observed. This demonstrates that a confining structure can affect dramatically the lasing behaviour.

In the second part of this thesis, the transverse distribution of the radiation within hetero-epitaxial layers is studied in more detail. An electromagnetic model for such a cavity is introduced in which the spatial variation of the refractive index within the epitaxial layer is approximated by a step profile. The importance of the permanent confining surface is shown to depend on the cavity parameters such as refractive index difference between active and passive region, absorption in the passive region and thickness of the epitaxial layer compared to the

electron penetration depth. The specific conditions under which transient waveguide effects take preponderance over the permanent optical confinement are derived explicitly. It is found that the spatial distribution can be very sensitive to the permanent waveguide effects. Accordingly, the far-field diffraction patterns of the lasing radiation were measured on hetero-epitaxial layers of various thicknesses and on bulk material under various pumping conditions. The theoretical fit to the experimental data shows that multimode lasing is a common occurence in epitaxial layers. Moreover, the time-resolved spatial measurements on the bulk material confirm that long time delays to lasing threshold are effectively associated with optical confinement of the radiation.

There is evidence that waveguiding mechanisms as described here are also important factors in the behaviour of other semiconductor laser configurations. Time-resolved measurements of the far-field patterns could be used to verify this proposition.

Acknowledgments

I am grateful to my supervisors Dr. J. Shewchun and Dr. B.K. Garside for their guidance during this work. Thanks also go to P. Wong who produced the GaInAs hetero-epitaxial layers.

TABLE OF CONTENTS

TABLE OF CONTENTS (cont)

LIST OF TABLES

LIST OF FIGURES

LIST OF FIGURES (cont)

LIST OF FIGURES (cont)

CHAPTER 1

INTRODUCTION

1.1 Background and Scope

Spurred by the prospect of widespread application in the field of optical communication, huge efforts have been invested in the development of semiconductor lasers. Since the fabrication of the first Zn-diffused GaAs junction lasers [1,2,3], the emphasis in research has been primarily directed toward reducing the lasing threshold current, bringing operation to room temperature and extending the life expectancy of the devices. Improvement of the fabrication process by the use of liquid-phase epitaxial growth led to better control of the doping profile making possible pulsed operation at room temperature for threshold currents of the order of $2.5\text{-}5\times10^4$ A/cm^2 [4,5]. The next stage saw the introduction of the heterojunction [6,7], a structure which can provide partial confinement for the injected carriers and the stimulated radiation within a narrower active region thereby reducing further the threshold current. Finally, more sophisticated devices incorporating a double heterostructure which confines the minority carriers on both sides of the active region have now made possible continuous operation at room temperature

with pumping current densities as low as 500 A/cm^2 [8,9,10]. Furthermore, the expected life of those devices exceeds 10,000 hours. This combination of characteristics has made semiconductor lasers very attractive for use in practical communication systems. The most recent efforts have been directed toward reducing the spectral width of the emission and improving the response time to the excitation pulse in order to increase the information carrying capacity.

In the course of the many investigations conducted, a number of intriguing phenomena have been uncovered relative to the dynamics of lasing in semiconductors. For instance, transient effects such as spectral [11-14] and spatial [15,16] variations of the laser emission during the pump cycle have been observed. But one of the most puzzling aspects concerns the behaviour of the time delay to lasing threshold in homojunction [17-19], single heterojunction [20,21] and electron-beam-pumped bulk material [22,23]. It has been observed that, under certain conditions, the time between the start of the excitation and the onset of lasing can exceed by as much as two orders of magnitude the minority carrier lifetime. Since this effect has been encountered in a range of materials under various pumping conditions, the relevant mechanisms may be dependent not so much on the intrinsic properties of the material as suggested in many theoretical models but on the laser

structure itself. The conspicuous absence of long delays and angular tuning in double-heterostructure lasers [24] suggests that waveguide effects (be it transient or permanent), may be of primary importance in the laser dynamics. In this work, we propose to investigate such optically confining effects in various GaAs and GaInAs structures pumped by an electron beam. It is advantageous to use this pumping method because lasing can then be produced in bulk material thereby avoiding the added complexity of doping gradients necessary for junction lasers and the concomitant effects on the various optical parameters. Moreover, some time-dependent effects such as wavelength and angular tuning in electron-beam-pumped lasers have already been the subject of investigations and have been successfully accounted for on the basis of transient waveguiding in conjunction with the temporal and spatial dependence of the refractive index [15]. However, those measurements are a rather indirect and relatively insensitive reflection of the kinetics of the loss processes in those lasers. Consequently, the first part of this thesis deals with a more sensitive probe of those dynamical effects according to the following rationale.

The mechanism which controls the time delay to lasing threshold depends strongly on the laser medium and resonator characteristics. One mechanism, typical of gas laser

systems is simply due to the time it takes for the laser intensity to build up from an initial noise level. In a long, low gain resonator, this time is typically 0.1 to 1 μsec. Other potential major factors are the time for gain to build up once the pumping mechanism has been established, and any time-dependence of the resonator losses induced by the initiation of pumping. In the case of electron-beam-pumped semiconductor lasers, the time for radiation to build-up in the resonator is exceedingly short ($<10^{-10}$ sec). The time for the gain to build-up, once pumping commences is governed by the lifetime of electron-hole pairs. For materials employed in the work reported here, this lifetime is no more than a few nanoseconds [25-27]. The time delays we have observed vary up to several hundred nanoseconds and, as we shall show, reflect time-dependent variations in the laser resonator losses. The occurrence of spatial variations in the refractive index produces a waveguide effect in the laser medium which can strongly influence the losses incurred by the laser mode as it propagates through the thin active layer. Under appropriate conditions, this effect controls the time which elapses between the onset of electron beam excitation and the occurrence of lasing; this time delay (t_d) is sensitive to small changes in the time-dependent resonator losses. These loss variations, in turn, are a measure of the magnitude and time-dependence of the

refractive index spatial variation. In this way, variations of the refractive index due to heating of the active layer and changes due to the presence of gain are shown to be mechanisms which control optical confinement of the radiation in the pumped region and lead to delays of the magnitude observed experimentally.

In this work, observations of long time delays (over 100 nsec) in GaAs bulk samples are reported. A theoretical-experimental study of the variations of t_d with the electron-beam pumping current and voltage has been used to gain an understanding of how refractive index variations control t_d.

Similar temporal measurements were performed on hetero-epitaxial GaInAs samples which incorporate a permanent refractive index step. The behaviour of the time delays changes drastically for progressively thinner layers, the delays becoming of the order of the minority carrier lifetime for GaInAs layer thicknesses which approach the electron-beam penetration depth. Such a change in the temporal behaviour is attributed to the permanent refractive index step which ensues from the sharp variation in material composition. The effect of this interface on the laser behaviour depends on its separation from the active region and on the optical properties of the medium.

To determine, in a general way, under what conditions

the presence of this interface alters the lasing behaviour, in the second part of this thesis, the transverse distribution of the radiation within the epitaxial layer is evaluated using a simple model to approximate the transverse variation of the complex permittivity. The model also allows the evaluation of the gain required to support such laser modes which are stable in time. The dependence of the gain and the spatial distribution of the radiation on the presence of the interface is studied in detail. Determined explicitly are the specific conditions under which the radiation ceases to see the permanent refractive index step, the laser operation reverting to that characteristic of bulk material. It is found that the spatial field distribution is more sensitive to the presence of the interface than the variation in gain. Consequently, the far-field pattern was measured at lasing threshold in thin and thick hetero-epitaxial samples and bulk material. The results show that in thin samples, the far-field characteristics are determined by the presence of the interface and only short t_d's are observed. On the other hand, in bulk material, large variations in the far-field patterns and t_d occur. In between those two extremes, there are thick epitaxial layers which combine the characteristics of both the bulk material and the permanently confined epitaxial layer.

1.2 Electron-Beam-Pumping of Semiconductors: General Principles

A number of pumping mechanisms have been exploited to generate the excitation necessary to produce lasing effects in semiconductors. Carrier injection through a p-n junction is by far the most extensively used method in device applications. However, the requirement for the fabrication of a p-n junction often imposes unnecessary difficulties for purely investigative work. It is also possible to generate electron-hole pairs directly in the bulk material. Optical pumping by means of an intense light source such as another laser is commonly used. But, electron-beam pumping provides the most versatile tool for inverting the carrier population in semiconductors. It can be used directly to pump bulk samples making it possible to study materials for which the present technology does not permit the fabrication of a p-n junction. Moreover, it does not require matching to the band gap energy of the semiconductor as does optical pumping. Hence, the same apparatus can be used to investigate a wide range of materials. It is also the excitation scheme which most easily allows independent variations of the active region width and pumping intensity.

Fig. 1 illustrates the configuration employed in the present work to generate lasing in semiconductors. In short, the electron-beam impinges on a surface bounded by two parallel cleaved edges which form the mirrors of the

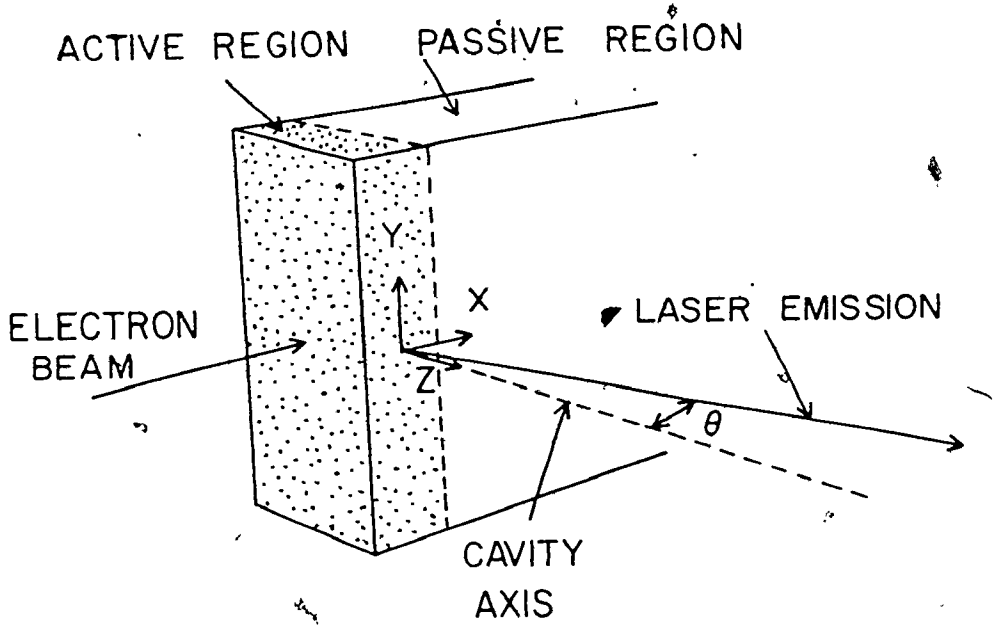

Fig. 1: Electron-beam-pumped semiconductor laser configuration. Also shown is the axis convention to be used throughout this work.

Fabry-Perot cavity and the laser emission is observed in the general direction of the normal to those cleaved edges. This figure also serves to define the axis convention to be used throughout this work.

The entire process from impact of the electron-beam on the sample to laser emission can be broken down into four stages. First, the high energy electrons striking the surface of a semiconductor are progressively slowed down through complex interactions with the material. This stage can be described as the deposition of the electron-beam energy in the semiconductor. A substantial fraction of the electrons are also backscattered at this point due to elastic and inelastic collisions. In a second stage, the deposited energy goes into the production of hot electron-hole pairs and the generation of phonons. It has been shown [28] that the amount of beam energy dissipated per electron-hole pair creation is, on the average, approximately three times the band gap energy. The hot electrons quickly lose their excess energy as they thermalize to the band edge, an effect which results in sizeable heating of the material. In the next stage, the carriers are redistributed according to the continuity equation. Similarly, the heat generated diffuses deeper into the crystal. Finally, the excess carriers recombine through the band gap to produce optical emission.

Klein [28] has already given a relatively accurate account of the electron-beam energy deposition into the material. The next step consists in evaluating the resulting temperature profile and the spatial distribution of the minority carriers. The evaluation of the temperature profile is a boundaty value problem of heat conduction. The time-dependent solution is determined explicitly in Appendix A using the profile suggested by Klein [28] for the heat generation rate. In the case of the minority carrier concentration, it is sufficient to solve the steady-state carrier transport equation since the carrier concentration will reach equilibrium within a few carrier lifetimes and those are much shorter than the time delays of interest. The solution is carried out in Appendix B using Klein's profile [28] as the carrier generation rate. The relevant results will be introduced in the next chapter as the need arises. In order to determine whether the lasing condition is satisfied, it will then be necessary to evaluate explicitly the gain resulting from the stimulated carrier recombination and the optical losses in the cavity. How such mechanisms can lead to time delays much longer than the carrier lifetime is studied in Chapter 2.

CHAPTER 2

TIME DELAY TO LASING THRESHOLD AND TRANSIENT WAVEGUIDING

2.1 General Considerations

The spatial inhomogeneity of the non-equilibrium carrier density, and hence, the gain, which appear when a bulk semiconductor is excited with an electron beam gives rise to important diffraction effects. These have a considerable influence on the characteristics of the laser radiation. In particular, the far-field pattern of the radiation from electron-beam-pumped lasers is not generally symmetrically disposed about the cavity axis, but rather deviates with respect to the axis by angles up to 30°. Not only does the angular deviation of the laser mode exist, but it also changes as a function of time during each pump cycle. Typically, in both GaAs and CdSe, the far-field diffraction patterns of the spatial modes have half-widths of $5\text{-}10^{\circ}$, deviating initially between 10 and 30° from the cavity axis in a direction away from the electron beam [15]. The deviation angle is found to decrease during each pulse by a factor of 2 or more. This general behaviour occurs in both II-VI and III-V materials, but the specific behaviour in each material is dependent upon its optical and thermal properties.

The basic features of the time-dependence of the far-field spatial modes were accounted for in terms of a dynamically varying optical confinement associated with the refractive index difference between the pumped and unpumped regions of the bulk semiconductor [15]. The sources of sufficiently large refractive index variations to produce waveguide effects in the mode propagation characteristics were identified as occuring through the temperature dependence of the medium refractive index and dispersion induced by the presence of gain.

The outflow of energy from the active to the passive region associated with the diffraction effects is an additional loss which must be overcome by the gain if lasing is to occur. Clearly, a mechanism that reduces the losses with time will have a determining influence on the threshold behaviour of the laser. An overall theory should include several aspects of this laser configuration. First, the external parameters such as pumping voltage, current density, and time from the start of the pumping pulse must be related to internal parameters: minority carrier concentration profile and temperature. One may then determine the optical parameters such as gain and refractive index variations which finally allow evaluation of the wavelength and time-dependent cavity losses. A comparison of the calculated gain and losses, taking proper account of

the wavelength dependence of both, determines whether threshold has been reached. Since the time delay to threshold is the quantity of interest, sequential calculations can be carried out until lasing threshold occurs. A complete calculation of the time dependence of the various optical confinement mechanisms is relatively complex; so we first treat the problem in a way which, although approximate, serves to give some overall insight.

2.2 Simple Model

On the average, the creation of one electron-hole pair using an electron beam requires three times the band gap energy [28]. The quasi-Fermi levels lie close to their respective band edges so that a large portion of the initial energy is lost as heat when the carriers thermalize to levels close to the band edge. Moreover, the temperature variations occur on a time scale larger than the time required for the gain or the radiation to build up. This, combined with the considerations of the preceding section, suggests that we should concentrate our attention on the heating effects in relation to diffraction losses.

Consider the following simple model to calculate the time delay to onset of lasing. As time elapses from the start of the electron beam pumping pulse, a temperature difference builds up between the active and passive regions

of the laser resonator. An associated refractive index difference between the two regions is established as a consequence. Accordingly, suppose that the dominant effect in determining the onset of lasing is the dramatic fall in diffraction losses as the temperature difference between the active and passive regions increases. Further, assume that a fixed temperature (and hence refractive index) difference is sufficient to produce confinement and that this is independent of the electron beam current. Consequently, calculation of time delay to threshold as a function of current only requires that we evaluate the time necessary to reach this "threshold temperature" as a function of current.

The determination of the time-dependent temperature profile for a particular heat source is a standard boundary value problem whose solution is given by [29]

$$\Delta T(x,t) = \int_0^{\infty} \int_0^{t} \frac{\alpha}{k} \frac{g(x',t')}{[4\pi\alpha(t-t')]^{1/2}} \left[\exp\left(-\frac{(x-x')^2}{4\alpha(t-t')}\right) + \exp\left(-\frac{(x+x')^2}{4\alpha(t-t')}\right)\right] dt'\,dx' , \tag{2.1}$$

where ΔT is the temperature rise relative to the initial temperature at the start of the pumping cycle as a function of time and depth below the surface, $g(x,t)$ is the heat generation rate, $\alpha = k/C$, k is the thermal conductivity and C is the specific heat. The differential energy loss

described by Klein [28] has been used to specify the spatial distribution of thermal input to the crystal. The analytic integration of Equation (2.1) is given in Appendix A.

We wish to see whether the simple model just described can predict, in a general way, the variations in time delay to onset of lasing. Experimentally, the time delay to threshold is measured as a function of current density for a bulk GaAs sample at a beam voltage of 30 kV. A "threshold temperature difference" can be calculated for each experimental data point. An average "threshold temperature difference" of $12^{o}K$ is obtained from this data. Assuming this average temperature difference determines the threshold condition, the time necessary to reach this temperature difference is plotted as a function of pumping current. This is shown in Fig. 2 along with some experimentally observed time delays. Considering the very approximate nature of the theoretical model employed, the agreement with the experimental observation is qualitatively good.

Furthermore, the average temperature difference is found to give a refractive index step of a size which is approximately correct for optical confinement. This lends a considerable degree of confidence to the overall intepretation of the results. There are, of course, deviations from the simple model: for long delay times, more current is

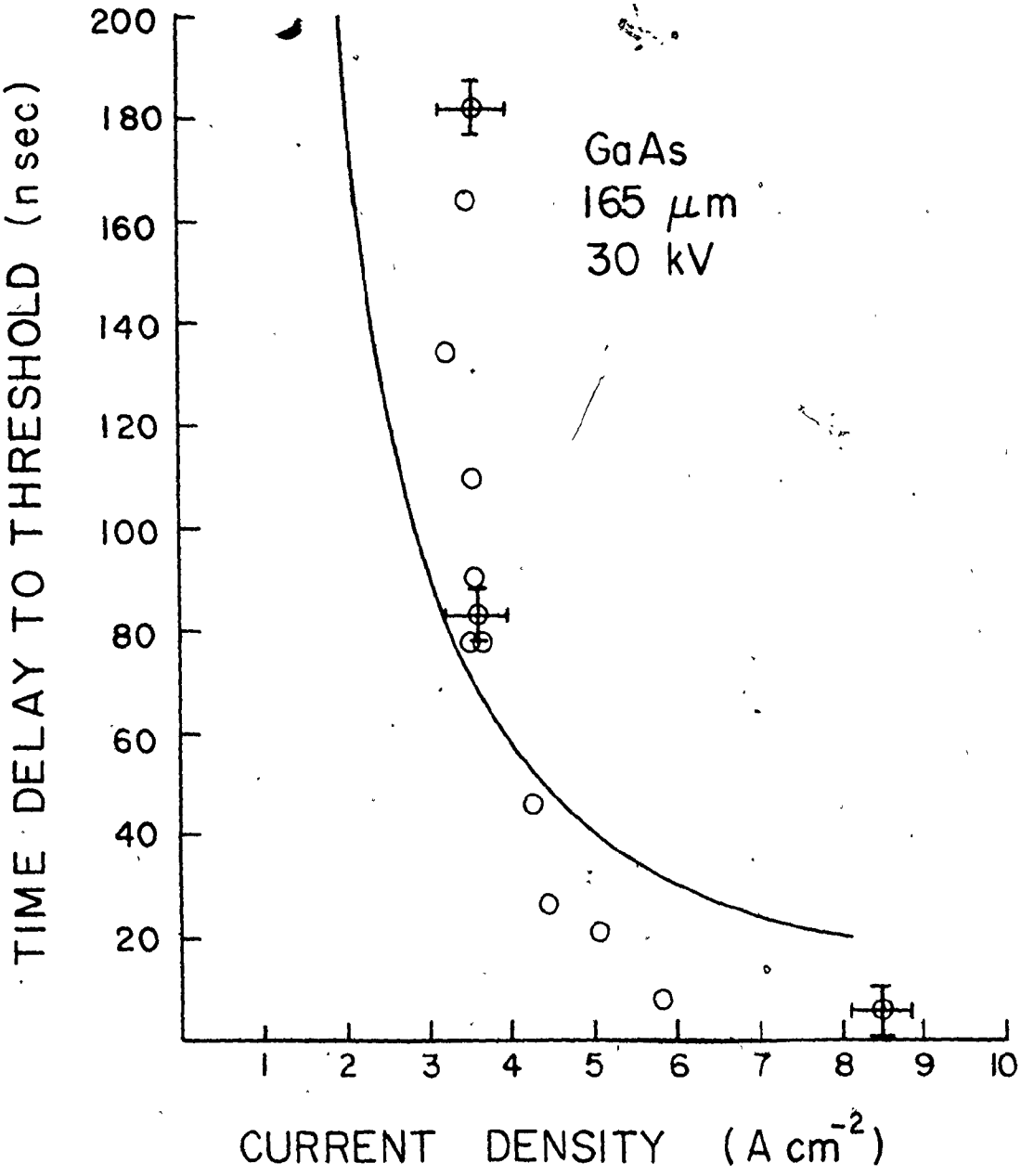

Fig. 2: Experimental current dependence of the time delay to lasing threshold at 30 kV in GaAs compared to the time delay necessary to reach the "average threshold temperature" (88.6°K) calculated using the simple model. The cold finger temperature is 77°K. Error bars indicate the range of reproducibility.

required to reach threshold than predicted, whereas for short delay times, the inverse situation holds.

The simple, somewhat empirical, model we have described in this section has proved capable of qualitatively accounting for observations on a gross scale. In the following section, a more inclusive model is described.

2.3 Comprehensive Model

The problem can be split into three separate parts. First, we determine the carrier concentration and hence the gain needed to reach threshold at a given temperature in the active region using the model described below. Subsequently, we can evaluate the pumping current density required to produce such a carrier density. The time delay to threshold for this particular current is then calculated by determining the time needed to reach this temperature following the formulation described in the previous section.

Now, to determine the carrier concentration needed to reach threshold at a given temperature, we proceed as follows. For a given carrier concentration and temperature, the gain can be calculated using the parabolic band approximation [30]. Next, the evaluation of the cavity losses requires a solution for the propagation of the electromagnetic field in the resonator. Several models can be applied, depending on the distribution of the imaginary

component of the permittivity which is directly related to the gain distribution. One such model has been proposed by Bogdankevich [31] in which $\epsilon''(x)$ is given by the following analytical expression:

$$\epsilon''(x) = (\epsilon_m'' + \epsilon_\infty'')\,\mathrm{sech}^2 px - \epsilon_\infty'' , \qquad (2.2)$$

where ϵ_m'' is the value of the imaginary part of the permittivity at its maximum ($x = 0$), ϵ_∞'' is the value of $\epsilon''(x)$ deep in the unexcited part of the crystal at the laser emission frequency and $p = [(2d)^{-1} \ln(3 + 2\sqrt{2})]$ is related to the width of the distribution of $\epsilon''(x)$ at the midheight coordinate d. This representation for $\epsilon''(x)$ allows analytical solutions to be obtained for the propagating field.

Furthermore, it is assumed in the theory that the distribution of the real components of the permittivity (associated with the refractive index change due to temperature and due to gain) follows the same functional form as $\epsilon''(x)$. That is to say,

$$\delta\epsilon(x) = \delta\epsilon_o \mathrm{sech}^2 px , \qquad (2.3)$$

where $\delta\epsilon_o$ is the change in permittivity due to the change in refractive index at $x = 0$. This functional variation is compared in Fig. 3 to the calculated temperature and carrier concentration profiles which control the spatial

Fig. 3: Comparison of the various spatial distributions related to the permittivity: 1) sech^2 profile for d = 2.7 μm; 2) steady-state minority carrier concentration profile at 30 kV for L = 1 μm, τ = 1 nsec, s = 1 x 10^6 cm-sec^{-1}, and 3) temperature profile at 30 kV and t = 20 nsec. Each curve is normalized such that its maximum is unity.

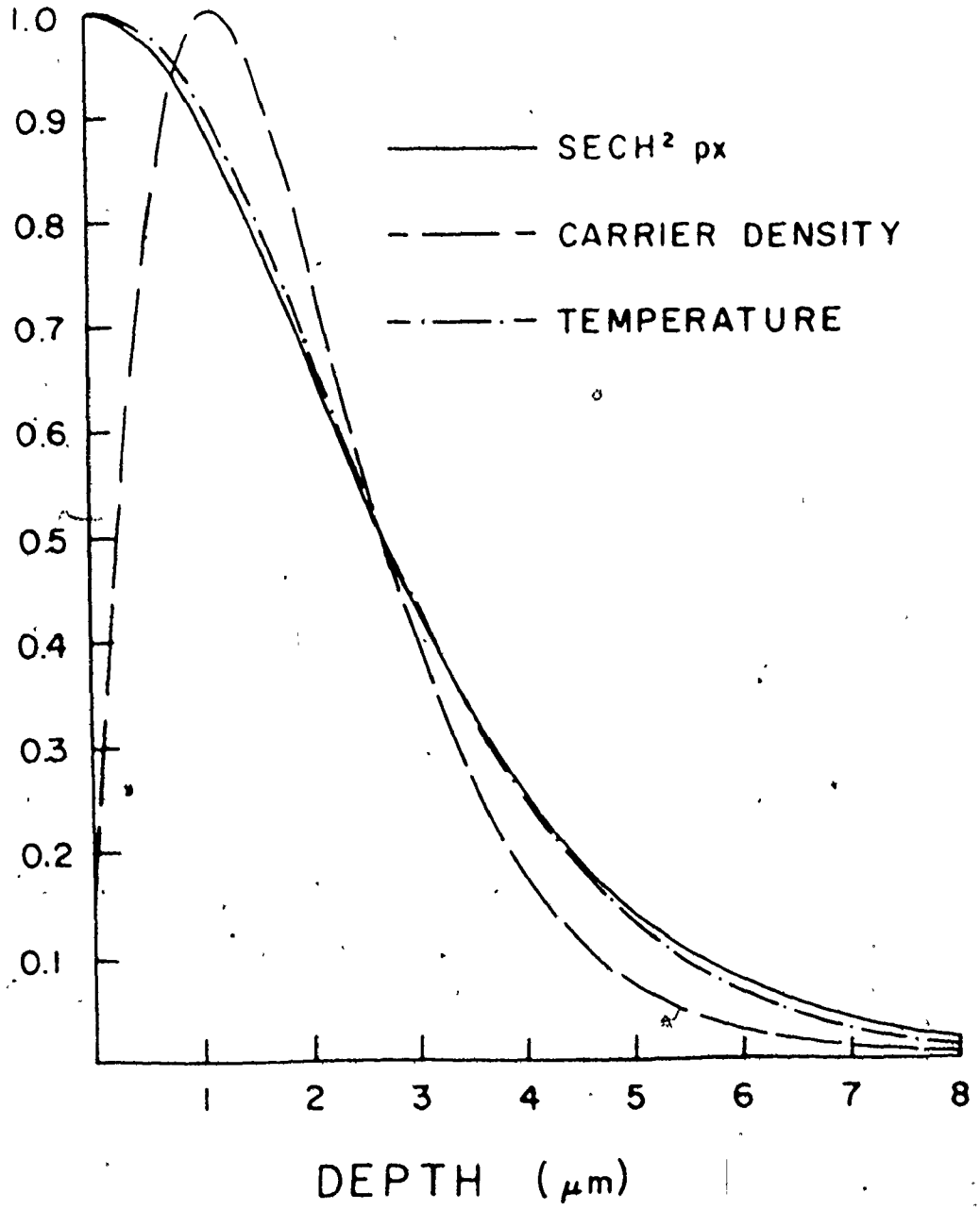
1.0
0.9
0.8
0.7
0.6
0.5
0.4
0.3
0.2
0.1
SECH² px
CARRIER DENSITY
TEMPERATURE
1
2
3
4
5
6
7
8
DEPTH (μm)

distribution of the refractive index and gain respectively. The basis for those calculated dependencies is given in Appendices A and B and is predicated on a model described by Klein [28] for the differential energy loss of the electron beam in the semiconductor material. The coincidence between the calculated temperature dependence and the functional form $\mathrm{sech}^2 px$ is extremely close. The variation of the temperature distribution with time is discussed in Appendix A. The agreement of the profiles is generally good except at the surface for the carrier concentration. This disagreement is due to the surface recombination which has no significant impact on the calculation except that it changes the spatially averaged passive loss. Accordingly we employ this theory to determine a solution for ε_m'' in the steady state. It is shown in Appendix C that

$$\varepsilon_m'' = \varepsilon_o'' + \frac{3}{2}\frac{p^2}{k^2}\varepsilon_o' \left\{\frac{1}{2}\left[\left(1 + 4\frac{k^2}{p^2}\frac{\delta\varepsilon_o}{\varepsilon_o'}\right)^2 + \left(\frac{4k^2}{p^2}\frac{\varepsilon_m'' + \varepsilon_\infty''}{\varepsilon_o'}\right)^2\right]^{1/2} - \frac{1}{2}\left(1 + \frac{4k^2}{p^2}\frac{\delta\varepsilon_o}{\varepsilon_o'}\right)\right\}^{1/2}, \tag{2.4}$$

where k is the wave number and ε_o' is the bulk permittivity.

The value obtained for ε_m'' gives the gain that would be necessary to reach threshold for the selected set of optical parameters $\delta\varepsilon_o$, ε_∞'', and ε_o''. (The calculated dependence of this gain on the optical parameters will be

discussed in more detail in Chapter 4 along with similar models for the lasing cavity.) As mentioned earlier, the change in the real component of the permittivity $\delta\varepsilon_o$ is associated with the refractive index change due to gain and temperature. The former is evaluated using the appropriate Kramers-Kronig relations [15,32] applied to the expression for the gain [30]. To calculate the change in refractive index as a function of temperature we use an extrapolation of a fit to Marple's data [33,34] at 103^oK. The approach taken is in accordance with a model described by Stern [32]. The imaginary part of the permittivity deep in the unexcited part of the semiconductor (ε''_∞) is similarly obtained from an exponential fit to Hill's data [35]. The non-resonant losses (ε''_o), in which the mirror transmission is included as a distributed loss, is given by

$$\varepsilon''_o = \frac{\lambda n}{2\pi}\left(\alpha_{f.c.} - \frac{1}{\ell}\ln R\right), \qquad (2.5)$$

where $\alpha_{f.c.}$ includes losses such as that due to free carriers, ℓ is the cavity length, R is the reflectivity of the mirrors at the cavity ends, λ is the wavelength in vacuo and n is the refractive index.

The gain necessary to reach threshold is compared to the gain generated from the associated minority carrier concentration. The latter is adjusted, and the calculation repeated in a self-consistent manner until the gain available is equal to the gain required for threshold. It

is important to note that both these quantities are wavelength dependent and this has been taken into account. In this way, we evaluate the carrier concentration needed for threshold (N_{th}) as a function of temperature for different values of the active region thickness determined by the pumping voltage as shown in Fig. 4.

The general behaviour of the threshold carrier concentration is similar for the three thicknesses. As the temperature rises, a point is reached at which the carrier concentration needed to reach threshold suddenly drops. This comes about in the following way. At a temperature close to the initial sample temperature, 77°K, the negative change in index due to gain is larger in magnitude than the positive contribution due to temperature. This has the effect of producing an increase in the diffraction losses. Moreover, the rapid variation with wavelength of Δn due to gain pushes the lasing wavelength toward the short wavelength side of the gain peak. When the temperature rise is sufficient to make the total change in refractive index positive, the radiation tends to become confined. This reduces the gain needed to reach threshold which feeds back through the refractive index due to gain and, thereby, enhances the optical confinement. In addition, the reduced dispersion allows laser oscillation at wavelengths closer to the gain peak further reducing the gain needed to attain

Fig. 4: Minority carrier concentration at lasing threshold calculated as a function of surface temperature for 20, 30 and 40 kV electron beam voltages corresponding to depth at half maximum of 1.85 μm, 2.7 μm and 3.7 μm, respectively. The imaginary part of the permittivity due to non-resonant losses is $\varepsilon_o'' = 0.005$.

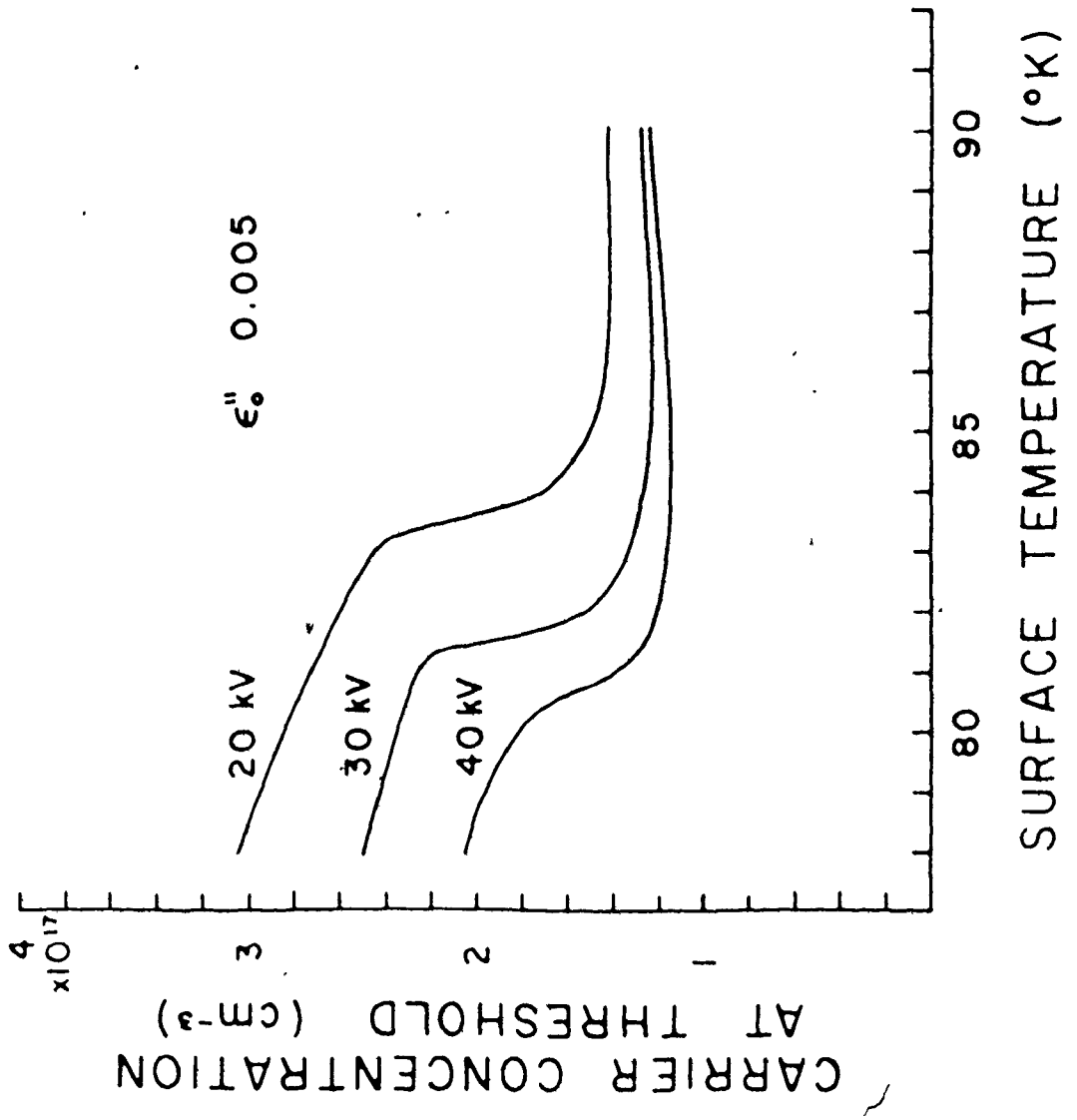
CARRIER CONCENTRATION
AT THRESHOLD (cm⁻³)
4
x10¹⁷
3
2
1
80
85
90
SURFACE TEMPERATURE (°K)
ε₀'' 0.005
20 kV
30 kV
40 kV

lasing threshold. Consequently, by virtue of these strongly coupled feedback effects, a significant fall in the required gain for threshold is produced. Once optical confinement is established, the threshold carrier concentration is almost identical for the three pumping depths. The threshold carrier concentration becomes practically a bulk property independent of the active region width.

Fig. 5 shows how the calculated threshold carrier concentration varies with temperature for four different values of the non-resonant losses for a typical gain region of 1.85 μm (20 kV). The threshold carrier concentration increases with ϵ_o'' for a given temperature and the sudden drop in N_{th} is shifted to higher temperature simply because a higher gain is required to offset the increased loss. The general behaviour is not a specific property of the $\mathrm{sech}^2 px$ model, and similar results have been calculated using the step model [15] for $\epsilon'(x)$ and $\epsilon''(x)$.

To facilitate comparison with the experimental data, the theoretical results are recast in terms of the dependence of the time delay to threshold as a function of current density. It is shown in Appendix B that the excess electron concentration produced by the electron beam in the p-type sample can be described as a function of the distance x below the pumped surface by

Fig. 5: Minority carrier concentration at threshold calculated as a function of surface temperature for four values of the non-resonant losses. The electron-beam voltage is 20 kV.

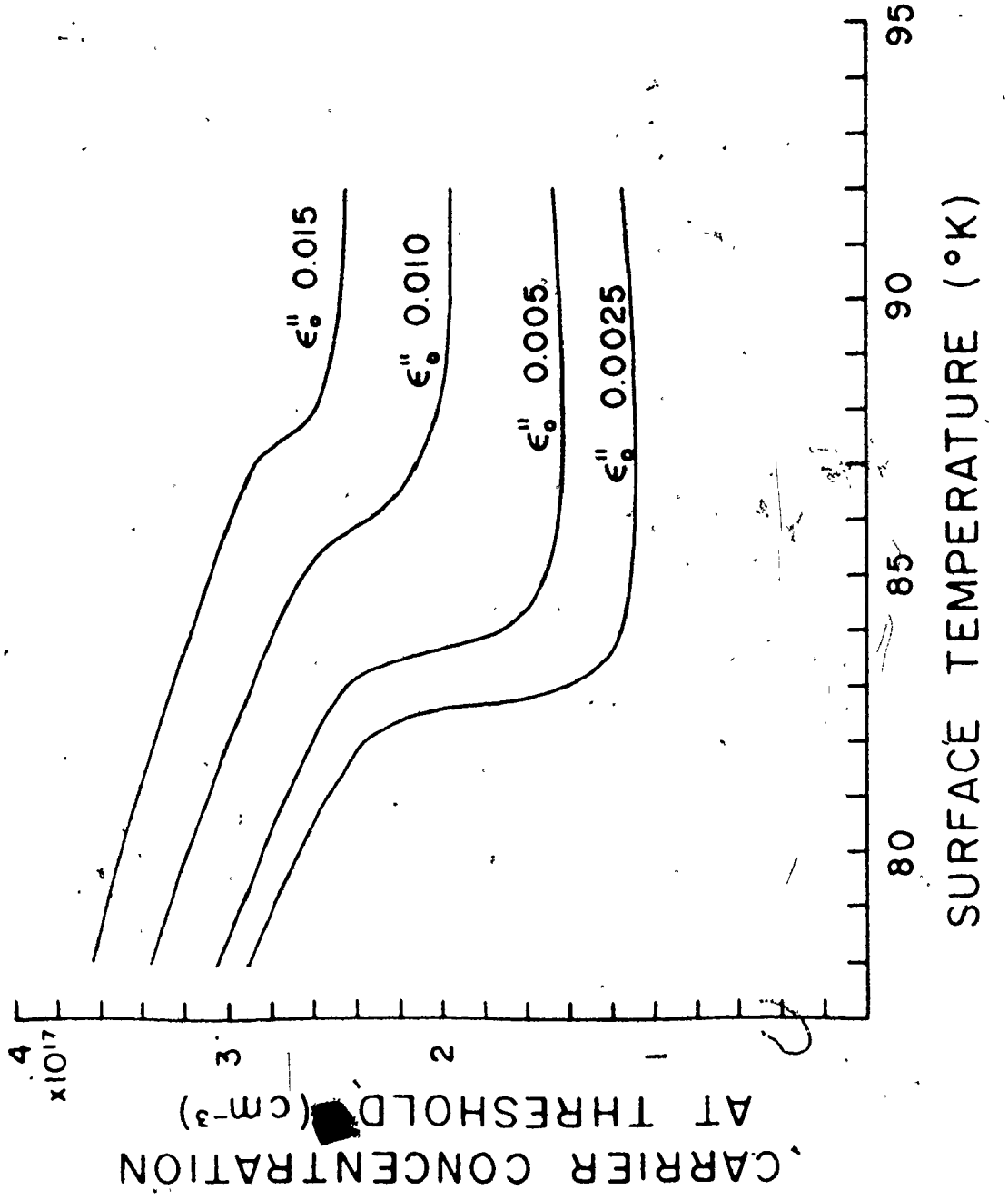
CARRIER CONCENTRATION
AT THRESHOLD (cm⁻³)
x10¹⁷
4
3
2
1
80
85
90
95
SURFACE TEMPERATURE (°K)
ε₀'' 0.015
ε₀'' 0.010
ε₀'' 0.005
ε₀'' 0.0025

$$N(x) = \frac{J}{3eE_g}\frac{E}{R_B}\frac{\mu R_B}{4}\tau\{2\mu^3L^3(\mu^2L^2-1)^{-2}[\exp(-\frac{|a-x|}{L}) + \sigma\exp(-\frac{a+x}{L})]-(\mu^2L^2-1)^{-2}[(1+\mu|a-x|)(\mu^2L^2-1) + 2\mu^2L^2]\exp(-\mu|a-x|) - \frac{1}{2}[\frac{\sigma}{\mu L-1}(1+\mu a+\frac{\mu L}{\mu L-1}) + \frac{1}{\mu L+1}(1+\mu a+\frac{\mu L}{\mu L+1})]\exp(\frac{-x}{L}-\mu a)\}, \quad (2.6)$$

where J and E are the electron-beam current density and voltage, respectively, E_g is the band gap energy in eV, e the electronic charge, L and τ are the diffusion length and the lifetime of the minority carriers while σ is related to the surface recombination velocity s by $\sigma = (1 - s\tau/L)/(1 + s\tau/L)$. The model for the differential energy loss due to Klein [28] is employed in establishing this expression. The other parameters are defined in Appendix A. A steady-state solution to the continuity equation is appropriate in this case because the minority carrier lifetime (≈1 nsec) is much shorter than the time delays of interest. Consequently, given the current density and the electron beam energy, one can determine the minority carrier concentration. Finally, Equation (A.3) provides the relation necessary to determine at what time a given active region temperature will be reached as a function of pumping current density and electron beam energy. In the next chapter, the time delays to threshold calculated using this model will be compared to experimental results.

CHAPTER 3

EXPERIMENTAL TIME DELAYS TO LASING THRESHOLD

3.1 Experimental Apparatus

Fig. 6 shows a schematic diagram of the experimental apparatus used for the time-delay-to-threshold measurements reported in this work. It is composed of an electron-beam-pumping system, a vacuum chamber and an optical detection system.

An electron gun of the type 5AZP was used to generate the electron beam. Originally designed as part of a projection kinescope, this gun has an indirectly heated oxide-coated cathode and is capable of operation at up to 40 kV. The ancillary electronic assembly, which included the three grid bias supplies and the pulsing circuit, was mounted in a Faraday cage floating at the accelerating voltage. The bias power supplies were obtained commercially while the focusing grid circuit and the pulser were built in-house. All the power supplies were of the adjustable type in order to make the bias corrections necessary with a change in accelerating voltage.

The bias for the focusing grid was derived from the accelerating voltage through a voltage divider which included a H-V triode, in series with the resistor chain, to

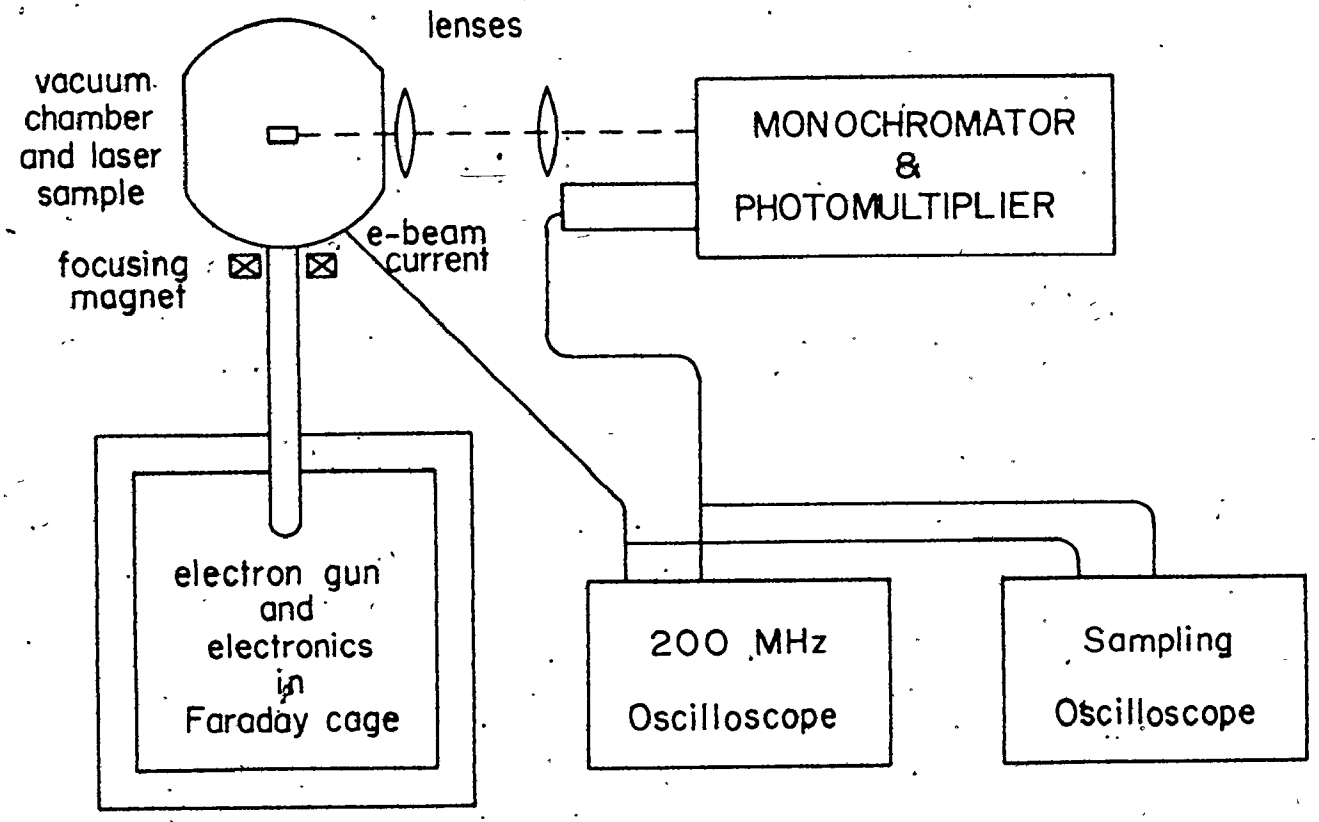

Fig. 6: Schematic diagram of experimental apparatus.

control the potential drop. The pulsing circuit, Fig. 7, consisted of a coaxial delay line which discharged through a mercury reed switch mounted inside a coaxial housing specifically designed to minimize reflection and ringing. The pulse was fed into a 50 ohm termination in parallel with the control grid of the electron gun. The whole pulser circuit floated at ≈ -170 V to provide the hold-off voltage on the control grid. With this pulse generator, electron-beam risetimes of 1 nsec were achieved with a pulse flatness within 10% over the 200 nsec pulse. Such fast flat pulses are necessary to make time delay measurements in the nanosecond range. The mechanical operation of the reed switch limited the pulse repetition rate to approximately 100 p.p.s. but a rate of 60 p.p.s. was chosen to minimize the power line interference. For more details about a similar electron-beam-pumping system, [36] should be consulted.

The electron-beam was positioned on the sample by means of a focusing electromagnet mounted on an x-z micro-positioner. A phosphor-coated brass screen placed near the sample assisted in this procedure. The screen was insulated electrically from the dewar proper and connected to the oscilloscope through a vacuum feedthrough to permit measurement of the beam current and to supply the triggering pulse. By making a second current measurement with the beam

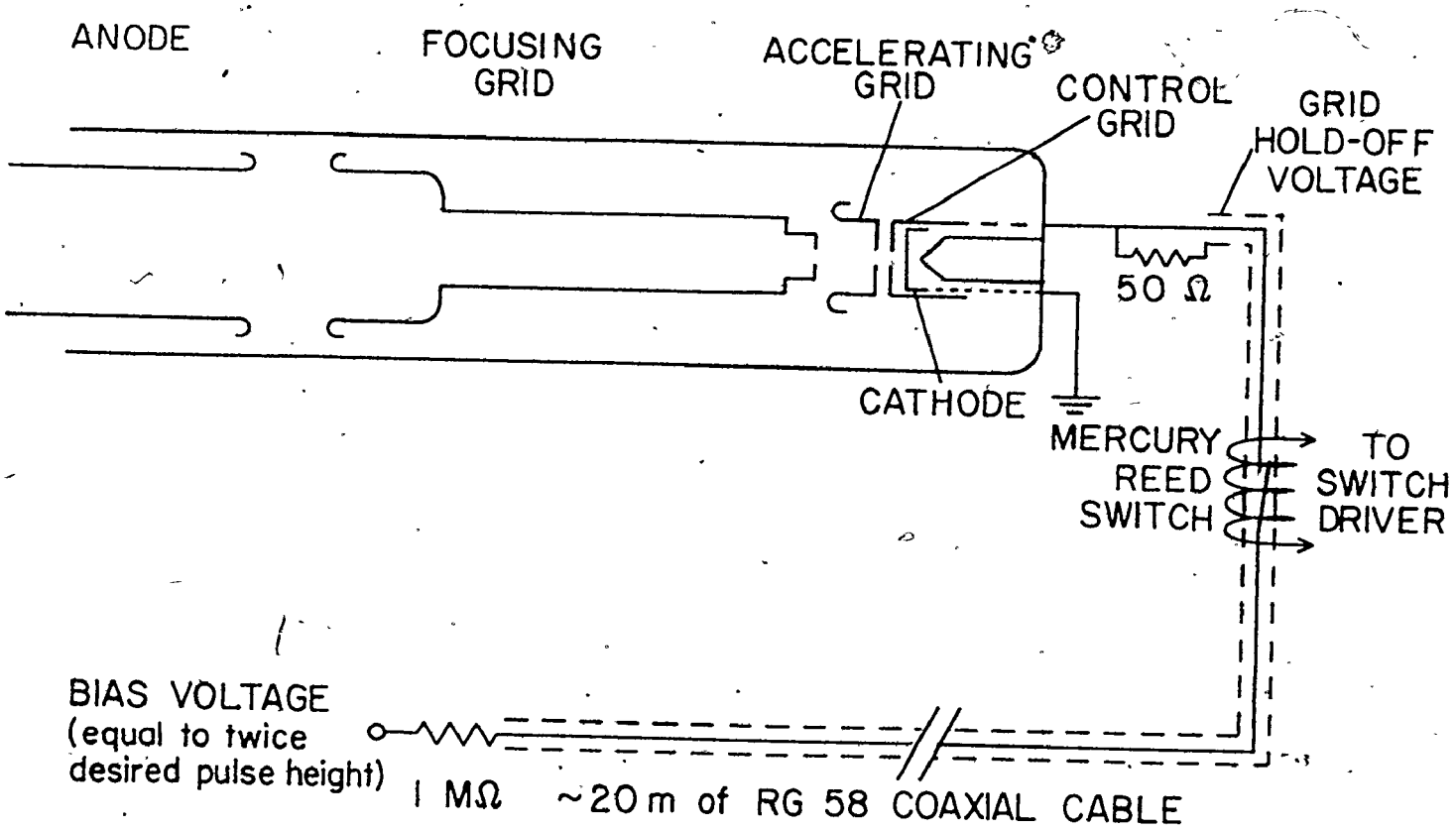

Fig. 7: Schematic diagram of electron gun and pulser circuit.

located over a small hole of known diameter, it was possible to calculate the current density, assuming, as is generally done, that the electron beam has a Gaussian profile.

The laser samples were mounted on the cold finger of a liquid nitrogen dewar which shared the vacuum chamber with the electron gun. A pair of lenses gathered the emitted light over a solid angle of 0.28 sr and focused it on the entrance slit of a 0.5 m Ebert scanning monochromator. The radiation was detected by a cooled S-1 photomultiplier and the signal fed into a sampling oscilloscope. A 200 MHz oscilloscope was also used as a monitor. To complete this description of the experimental apparatus, a list of the most relevant pieces of equipment, their specifications, and the name of the manufacturers is given in Table I.

Zn-doped GaAs ($p = 2 \times 10^{18}$ cm^{-3} at 300 ^{o}K) bulk crystals, obtained from Laser Diode Inc., were used for the main measurements. The pumped surface was polished and chemically etched while the two cavity faces were cleaved. The cavity length varied between 120 and 165 μm.

3.2 Experimental Results

For a given pumping current and voltage, the wavelength spectrum was scanned to find the earliest appearance of a sharp Fabry-Perot mode (see [12] for further discussion on lasing criteria) and the time delay to this event

TABLE I: List of Most Relevant Pieces of Equipment

EQUIPMENT	SPECIFICATIONS	MANUFACTURER (MODEL)
Electron Gun 5AZP	40 kV max ≈ 7 mA ≈ 250 μm beam FWHI	Superior Electronics RCA Electro Scan Thomas Electronics Griffiths Electronics
Mercury Reed Switch	1 nsec risetime	Northern Electric (218A)
0.5 m Ebert Scanning Monochromator	0.4 Å resolution with 590 grooves/mm grating	Jarrell Ash (82-020)
Photomultiplier	S-1 spectral response	RCA (7102)
Sampling Oscilloscope	300 psec risetime 2mV/div sensitivity	Hewlett-Packard (140A, 1410A, 1425A)
Real Time Oscilloscope	1.8 nsec risetime 2mV/div sensitivity	Tektronix (475)

measured with respect to the appearance of the spontaneous emission. This reference was used instead of the rising edge of the electron beam to compensate for the inherent time delays in the optical detection system.

The discrete points in Fig. 8 illustrate the experimental dependence of the time delay to lasing threshold of a GaAs sample as a function of pumping current for three values of the accelerating voltage. The curves are theoretical fits to the experimental data generated using the theoretical model described in the preceding chapter. As the current is increased, the time delay shortens as expected. The threshold current is higher in the case of the lower voltage not only because the resulting carrier concentration is lower for a given pumping current but also because the diffraction losses are higher.

Fig. 9 shows the results obtained from another GaAs sample for which the cavity length was somewhat shorter than that employed in obtaining the data presented in Fig. 8. The overall behaviour in the two cases is very similar, and the differences are typical of what has been observed over a wide range of samples. Note that the 40 kV threshold currents at a given time delay are generally lower for the second sample, despite the fact that the distributed cavity loss due to end reflectivity is expected to be higher. Furthermore, the position of the 30 kV curve is displaced

Fig. 8: Experimental dependence of the time delay to threshold on the pumping current density in GaAs at three electron beam voltages. The continuous curves are theoretical fits generated using the sech^2 model for the spatial distribution of the permittivity. The cavity length is 165 μm and the minority carrier lifetime 0.84 nsec. ε_o'' (20 kV) = 0.015, ε_o'' (30 kV) = 0.015, ε_o'' (40 kV) = 0.008.

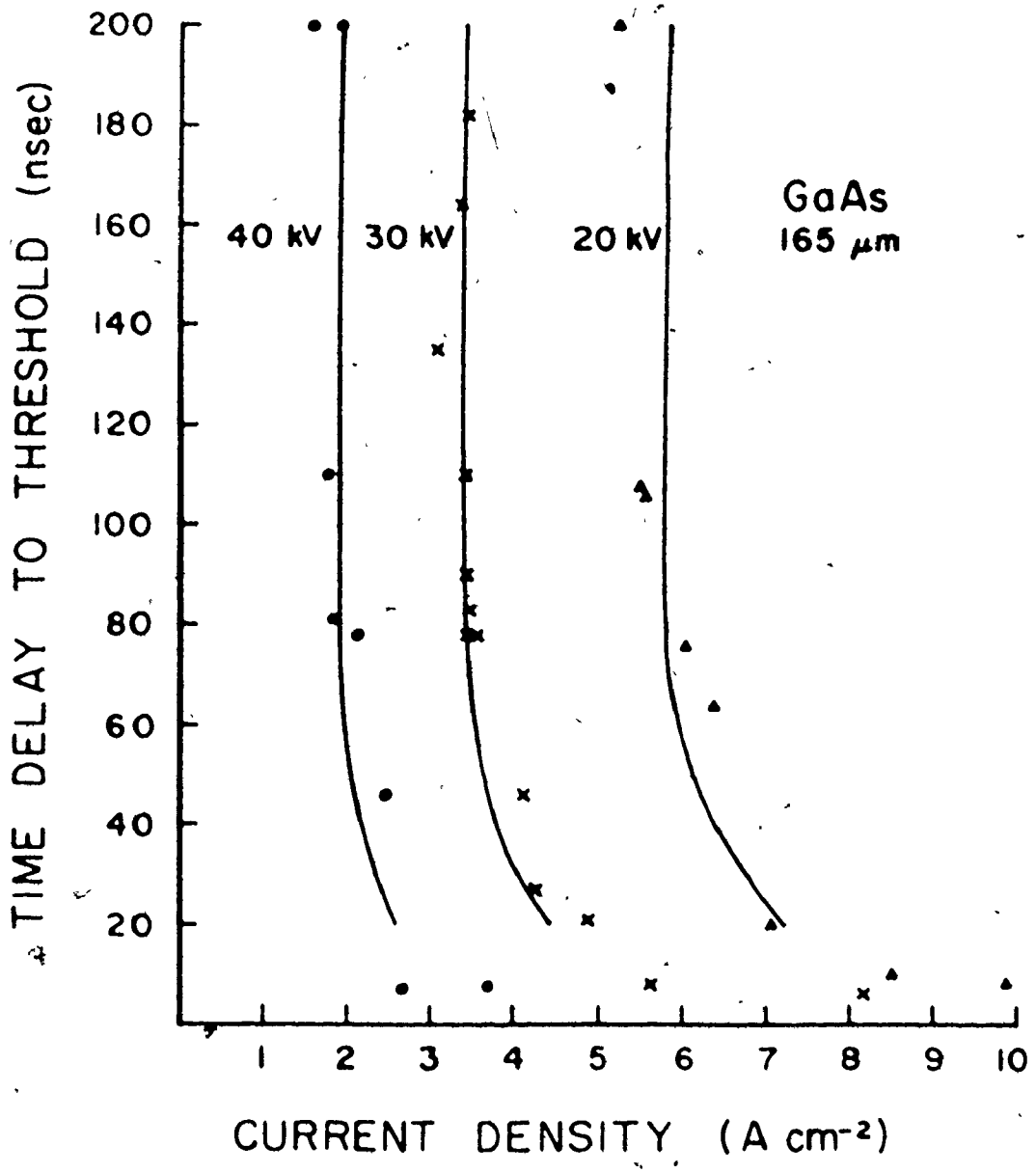
TIME DELAY TO THRESHOLD (nsec)
200
180
160
140
120
100
80
60
40
20
40 kV
30 kV
20 kV
GaAs
165 μm
1
2
3
4
5
6
7
8
9
10
CURRENT DENSITY (A cm⁻²)

Fig. 9: Experimental dependence of the time delay to threshold on the pumping current density in GaAs at three electron beam voltages. The cavity length is 120 μm. The continuous curves are theoretical fits generated using the $sech^2$ model for the spatial distribution of the permittivity. The minority carrier lifetime is 1 nsec. ε_o'' (20 kV) = 0.008, ε_o'' (30 kV) = 0.005, ε_o'' (40 kV) = 0.005. The inset illustrates a typical curve of light output vs time at 30 kV. Lasing which starts at 40 nsec dies out later during the pumping pulse.

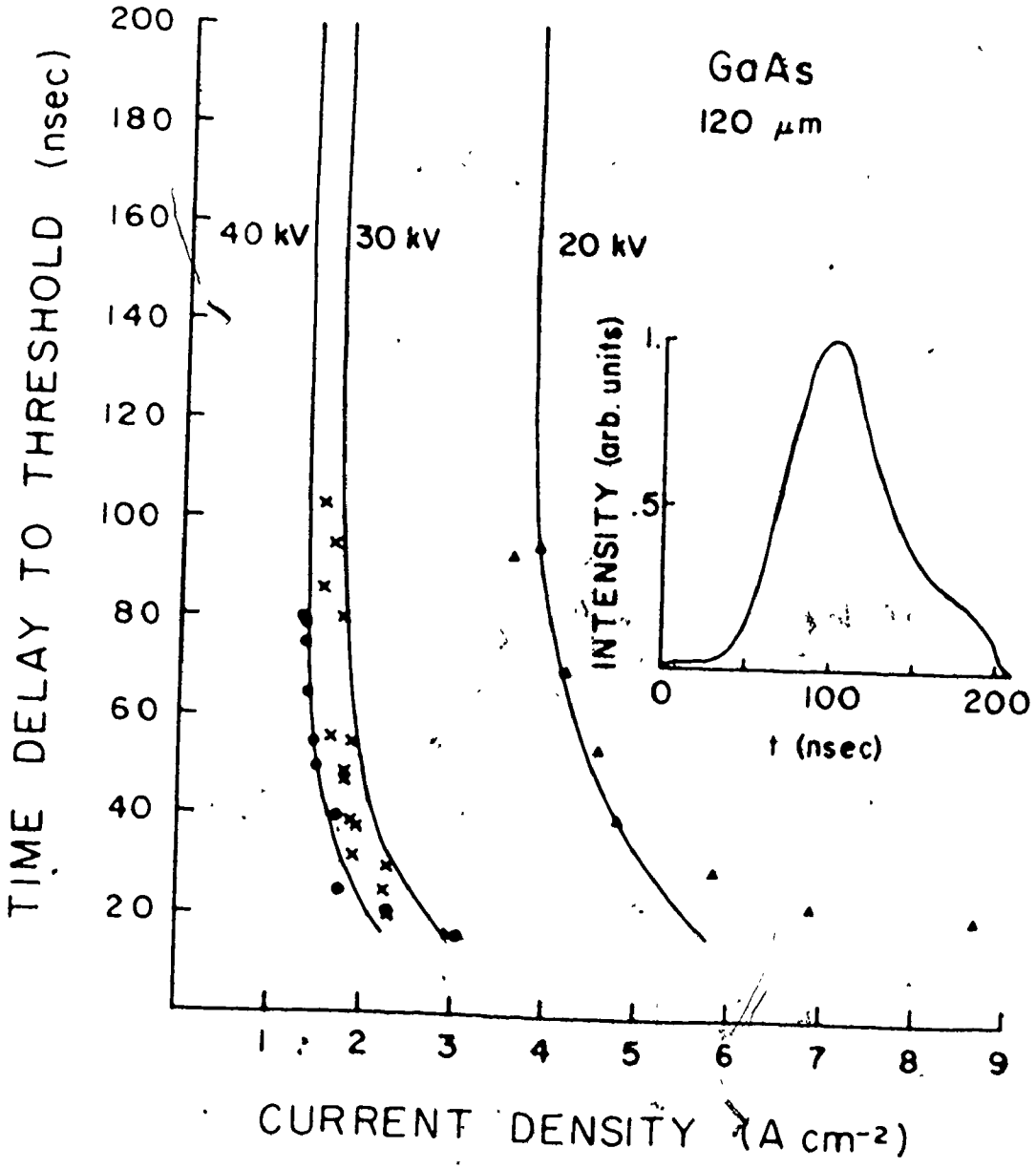
GaAs
120 μm
40 kV
30 kV
20 kV
TIME DELAY TO THRESHOLD (nsec)
200
180
160
140
120
100
80
60
40
20
INTENSITY (arb. units)
1
.5
0
100
200
t (nsec)
1
2
3
4
5
6
7
8
9
CURRENT DENSITY (A cm⁻²)

with respect to the 20 and 40 kV curves. This is not unusual, and reflects the fact that other losses, due to lack of crystalline perfection, etc., are also major contributors to the passive distributed loss. Consequently, in fitting the theory to experiment, the passive loss was treated as a parameter for each voltage. This loss increases with decreasing voltage which is interpreted as a deterioration of the optical quality as we approach the surface. The lifetime used is approximately 1 nsec. It basically determines the ratio of minority carrier to pumping current density in equation (2.6). For the sake of consistency, τ is kept constant for any given sample. Finally, for Zn-doped GaAs at $77^{o}K$, the diffusion length can be taken as $L = 1\mu m$ [27] and the surface recombination velocity as $s \doteq 10^{6}$ cm-sec^{-1} [25,27,37]. The agreement obtained between observation and the theoretical model is very satisfactory.

3.3 Permanent Waveguide Configuration Using GaInAs

At this point, we have shown that the observed lasing time delays are well accounted for by an electron-beam pump induced transient waveguide effect. A further series of experiments was undertaken to confirm that the observed lasing time delays do indeed owe their existence to transient waveguide effects. The essence of the method is

to make an electron-beam-pumped laser system which has a built-in optically confining waveguide. In that case, the laser mode is always confined during the beam pump pulse, and no long time-delays to the onset of lasing should be observed. The approach we followed was to employ a $Ga_xIn_{1-x}As$ layer, grown epitaxially on a GaAs substrate using a gas-phase transport system. The thickness was controlled to be in the same range as the electron beam penetration depth. There was no intentional doping.

For a sample having a thin GaInAs (0.7 μm) layer, the penetration depth was sufficient to produce electron-hole pairs in both the GaAs substrate material and the GaInAs layer. Two spontaneous emission peaks were observed, one at 0.8685 μm from GaInAs and a second at 0.828 μm. This indicates a decrease in band gap of 70 meV which corresponds to a 3.5% Indium composition [38]. A change in bandgap also implies a difference in refractive index between alloy and substrate. A good estimate of the change in index of refraction at the emission wavelength of the alloy region can be easily obtained using published experimental values of the refractive index as a function of wavelength for GaAs [33]. For the low alloy composition considered we assume that the shape of the curve does not change greatly but that it shifts by the same amount as the band gap energy. This results in a value of $\Delta n = 0.054$. Such a built-in

refractive index step due to the change in composition takes preponderance over the effect due to temperature change. Table II shows the longest time delay to threshold observed as a function of pumping voltage on four samples of increasing alloy thickness. The "longest time delay to threshold" is the time delay to lasing at a current below which lasing never occurs regardless of the pumping time.

In a laser specimen with a GaInAs layer thinner than the electron penetration depth, the time delay to threshold should be very short because the index step due to the change in composition forms a permanent waveguide which confines the radiation. Therefore, the time delay doesn't depend on diffraction losses anymore and is controlled by the dynamics of the gain, producing delay times of the order of the minority carrier lifetime. This is exemplified by the first two samples in Table II. For intermediate thicknesses (12 μm) we note that the time delays are significantly longer than those of the thin epitaxial layer but fall short of the bulk sample time delays. Finally, the 16 μm GaInAs layer is so thick that the semiconductor threshold behaviour is basically the same as that observed in bulk GaAs material. This is exemplified by the time-delay curves illustrated in Fig. 10. As expected, the behaviour of a 16 μm thick layer of GaInAs is indistinguishable from that of bulk GaInAs.

TABLE II: Longest time delays to lasing threshold observed in GaInAs epitaxial layers for a range of alloy thicknesses and electron-beam voltages.

Alloy Thickness	Longest Time Delay		
	20 kV	30 kV	40 kV
0.7 μm	8 nsec	5	8
3.5	10	7	6
12.0	58	45	10
16.0	97	125	70

Fig. 10: Experimental dependence of the time delay to lasing threshold on the pumping current density in a 16 μm GaInAs layer at three electron beam voltages. The continuous curves are theoretical fits generated using the $sech^2$ model for the spatial distribution of the permittivity. The minority carrier lifetime is 0.91 nsec and the cavity length 145 μm. ε_o'' (20 kV) = 0.008, ε_o'' (30 kV) = 0.0055, ε_o'' (40 kV) = 0.005.

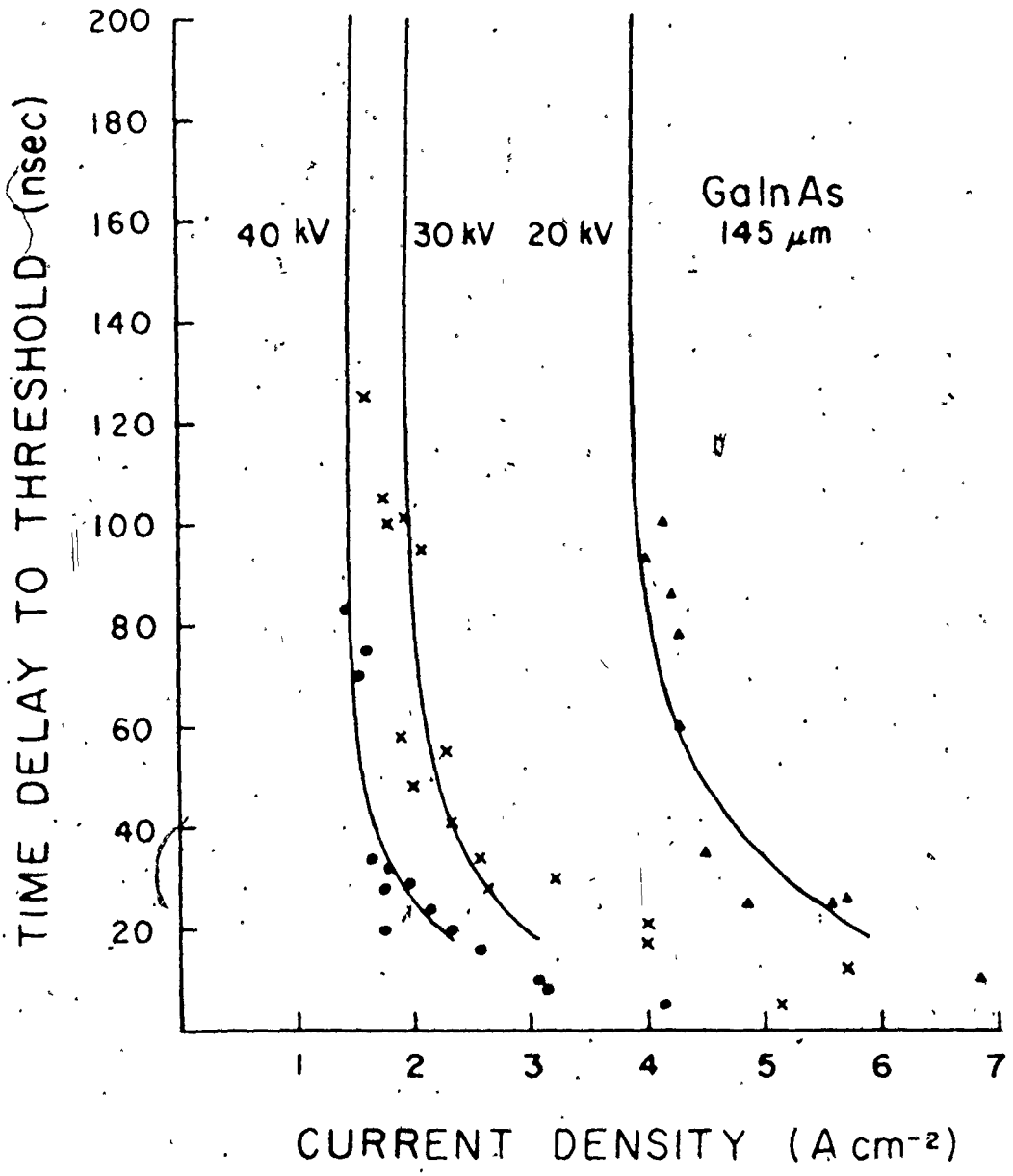
TIME DELAY TO THRESHOLD (nsec)
200
180
160
140
120
100
80
60
40
20
40 kV
30 kV
20 kV
GaInAs
145 μm
1
2
3
4
5
6
7
CURRENT DENSITY (A cm⁻²)

These measurements are a very clear indication that waveguide effects in electron-beam-pumped laser systems dominate the time-dependence of the onset of lasing, and confirm that the long lasing time delays observed in bulk material reflect the pump-induced transient-waveguide effects.

3.4 Discussion

The satisfactory account given by the transient waveguide model for the time delay behaviour in bulk material and thin GaInAs layers confirms that the temporal behaviour of the output is controlled, not by a gain mechanism but by the dynamics of the cavity losses. Several other theories have been presented in the last few years that purport to explain a similar temporal behaviour in junction lasers. For instance, a trapping model [18] has been postulated whereby the traps can capture an electron with an energy close to the valence band, producing a new state close to the conduction band which is now absorbing. At low pumping current, lasing cannot occur until a large proportion of those traps have been neutralized by the capture of a second electron. However, since those traps were reported inactive below 100°K, this model would not be applicable in our case. Furthermore, such a trap-filling model is not in accordance with the observed temporal

behaviour of thin GaInAs hetero-epitaxial layers on a GaAs substrate. The variations in the time delay behaviour as the epi-layer thickness is taken from 16 μm to 0.7 μm indicate that this change in behaviour is not related to a change in the intrinsic properties of the material but to a change in the cavity geometry and its confining properties. The same objection would seem to apply for other models predicated on the existence of unusual distribution of the density of states close to the band edge [21] or anomalous thermalization of hot carriers [21]. But, recently, Nunes et al [39], using an approach similar to the one described here, have successfully accounted for the long time delays in homojunction and single heterojunction lasers.

The advantage of such a model is that no prerequisite assumption about the semiconductor properties are necessary. Only phenomena which are known to occur when a semiconductor is excited by decakilovolt electrons are included such as shallow penetration depth with the concomitant narrow active region and ensuing diffraction effects, heating due to the low pumping efficiency and known thermal properties of the refractive index in the neighborhood of the band edge.

The importance of the transient waveguide effects in the laser dynamics is confirmed by the measurements on thin hetero-epitaxial layers. The absence of long time delays is as expected in a cavity that incorporates a permanently

confined active region. The theoretical model presented for the evaluation of the diffraction losses supposes a semi-infinite crystal and is not generally applicable to the thin epitaxial layer. A permanent index step greatly modifies the solution as confirmed by the experimental results. A complete account of such a situation requires the development of a model in which the unpumped region is of finite depth.

CHAPTER 4

HETERO-EPITAXIAL LAYER AS A LASER CAVITY

4.1 Theoretical Model and Transverse Mode Solutions

The steady-state condition for onset of lasing requires that the gain arising from the stimulated emission overcomes the cavity losses. For a homogeneous medium this condition can be written as

$$\alpha_g = \alpha_o + \ell^{-1} \ln R^{-1}$$

where α_g is the gain, α_o is the residual absorption, ℓ is the cavity length and R is the mirror reflectivity. In transversely excited electron-beam-pumped semiconductor lasers, however, the shallow penetration depth of the decakilovolt electrons results in spatial inhomogeneities of the medium on the scale of the emitted wavelength. The ensuing diffraction effects give rise to an additional loss which can be related to a spill-over of the radiation into the unpumped region. To determine the threshold gain requires the solution of Maxwell's equations for the normal modes in this inhomogeneous cavity. Such a procedure leads, for example, to the expression (2.4) used in Chapter 2 to determine the lasing condition in the bulk material. In that case, the spatial distribution of the complex

permittivity from the active to the passive region was approximated by a $sech^2$ profile. As with other models using a Gaussian profile [40] or a step profile [15], this model assumes that the medium extends to infinity in the direction away from the pumped surface. This assumption is well satisfied in bulk materials. In hetero-epitaxial layers, however, the refractive index change at the interface with the substrate can be sufficiently large to confine the laser radiation to propagation in a direction near the cavity axis. This greatly affects the transverse distribution of the radiation and a new solution for the transverse modes is required. We will assume, as in ref. [15] that the variation of the permittivity can be approximated by a step profile with the difference that a reflecting surface is present at a depth x=L from the pumped surface. The solutions for the normal modes in such a cavity will be expected to yield two important results, the gain necessary to support lasing modes stable in time and the transverse distribution of the electromagnetic field intensity. The latter allows evaluation of the far-field pattern which can then be compared with experimental measurements. But first we derive, from Maxwell's equations, the appropriate wave equation to be solved.

In linear isotropic media, the electric field $\bar{E}$, the electric displacement $\bar{D}$, the magnetic field $\bar{H}$ and the

magnetic flux density $\bar{B}$ are related by the following equations

$$\nabla \times \bar{H} = \frac{\partial \bar{D}}{\partial t} \tag{4.1}$$

$$\nabla \times \bar{E} = -\frac{\partial \bar{B}}{\partial t} \tag{4.2}$$

$$\bar{D} = \epsilon \, \epsilon_o \, \bar{E} \tag{4.3}$$

$$\bar{B} = \mu \, \bar{H} \tag{4.4}$$

where ϵ is the relative dielectric permittivity measured with respect to ϵ_o, the dielectric permittivity in vacuo and μ is known as the magnetic permeability. In non-magnetic media, its value is very nearly equal to the vacuum constant μ_o. Furthermore, in the absence of electric charges, the vector D satisfies the relation

$$\nabla \cdot \bar{D} = 0 \tag{4.5}$$

and the magnetic flux density always obeys the additional relation

$$\nabla \cdot \bar{B} = 0 \tag{4.6}$$

Substitute (4.4) into (4.2) and take the curl of the resulting equation

$$\nabla \times (\nabla \times \bar{E}) = -\mu_o \frac{\partial}{\partial t} (\nabla \times \bar{H}). \tag{4.7}$$

We can obtain an equation which depends solely on $\bar{E}$ by substituting (4.1) and (4.3) into (4.7)

$$\nabla \times (\nabla \times \bar{E}) + \epsilon \, \epsilon_o \, \mu_o \, \frac{\partial^2 \bar{E}}{\partial t^2} = 0.$$

Making use of the following identity which holds for a cartesian coordinate system

$$\nabla \times (\nabla \times \bar{E}) = \nabla \, (\nabla \cdot \bar{E}) - \nabla^2 \bar{E} \, ,$$

we obtain

$$\nabla^2 \bar{E} + \nabla \, (\bar{E} \cdot \frac{\nabla \epsilon}{\epsilon}) = \epsilon \, \epsilon_o \, \mu_o \, \frac{\partial^2 \bar{E}}{\partial t^2} \qquad (4.8)$$

with the help of (4.3) and (4.5). Since we will employ the step profile to approximate the spatial inhomogeneity of the permittivity within the epitaxial layer, ϵ is constant in space over each of the two regions, the gradient of ϵ vanishes and (4.8) in each region takes the form of the wave equation

$$\nabla^2 \bar{E} = \frac{\epsilon}{c^2} \, \frac{\partial^2 \bar{E}}{\partial t^2}$$

where $c = (\epsilon_o \, \mu_o)^{-1/2}$ is the velocity of light in vacuo. This equation holds for each component of the electric field i.e.

$$\nabla^2 E_i = \frac{\epsilon}{c^2} \, \frac{\partial^2 E_i}{\partial t^2} \qquad i = x, \, y, \, z \qquad (4.9)$$

Subsequently, it will be necessary to insure that the boundary conditions on the field are satisfied at the interface where the permittivity is discontinuous.

A few simplifying assumptions are possible at this point. First, because the electron-beam diameter is larger than the sample width, the central area is uniformly pumped. It follows that the optical parameters are not dependent on the spatial variable y. Hence, we can assume that the electric field is also independent of y thereby reducing the problem to the solution of a two-dimensional equation. Moreover, since the variations in permittivity along the x-axis occur over a much shorter distance than along the cavity axis z (the thickness of the active region is much smaller than the cavity length), the transverse modes should not be appreciably affected by the modal distribution along the cavity axis and hence it should be possible to decouple variations of the field along the x-axis from variations along the z-axis. Assuming that the modal distribution along the z-axis takes the form of a standing wave, we write the trial solution as follows

$$\bar{E}(x,z,t) = A(x,t)\, \sin\left(\pi \frac{Nz}{\ell}\right)\, e^{i\omega t}\, \bar{a}_y$$

where A is the field distribution along the x-axis and is left unspecified for the time being, N is the mode order along the z-axis, ℓ is the cavity length and ω is the light

frequency. The electric field is oriented along the y-axis, i.e. TE mode, in accordance with experimental measurement of the polarization. The development is very similar for TM modes but it has been shown for a related problem that there is a preference for the TE over the TM mode polarization [41].

Substituting the above expression for the field into the wave equation (4.7), we obtain

$$\frac{\partial^2 A}{\partial x^2} - \beta^2 A = \frac{\epsilon}{c^2}\left(\frac{\partial^2 A}{\partial t^2} + 2i\omega \frac{\partial A}{\partial t} - \omega^2 A\right) \qquad (4.10)$$

where $\beta = \pi N/\ell$ is the propagation constant along the cavity axis. On the time scale of the light frequency, the other time-dependent variations of the optical parameters are much slower. This justifies the use of the condition for a stationary state. Setting the time-dependent terms in the wave equation equal to zero results in the reduced wave equation

$$\frac{\partial^2 A}{\partial x^2} = \left(\beta^2 - \epsilon \frac{\omega^2}{c^2}\right) A \qquad (4.11)$$

We assume an index step profile of the form

$$\epsilon(x) = \begin{cases} \epsilon_o' + \delta\epsilon - i\,(\epsilon_o'' - \epsilon_g'') & \text{for } 0 \le x \le d \\ \epsilon_o' \qquad\quad - i\,(\epsilon_o'' + \epsilon_\ell'') & d < x \le L \end{cases} \qquad (4.12)$$

where ϵ_o' is the real part of the relative permittivity in the passive material, $\delta\epsilon$ is the change in the real part of the permittivity, ϵ_g'', ϵ_ℓ'', refer to the imaginary part of the permittivity due to gain α_g or absorption α_s respectively, ϵ_o'' is the contribution of the nonresonant losses α_o such as free-carrier absorption and end-mirror distributed losses, d is the thickness of the active region corresponding approximately to the electron-beam penetration depth and L is the thickness of the hetero-epitaxial layer.

Substituting these expression for the permittivity in (4.11), the wave equations in the two regions become

$$\frac{\partial^2 A}{\partial x^2} = [\beta^2 - \epsilon_o' \frac{\omega^2}{c^2}] A + i \frac{\omega^2}{c^2} (\epsilon_o'' - \epsilon_g'') A - \frac{\omega^2}{c^2} \delta\epsilon A \qquad (4.13a)$$

$$\frac{\partial^2 A}{\partial x^2} = [\beta^2 - \epsilon_o' \frac{\omega^2}{c^2}] A + i \frac{\omega^2}{c^2} (\epsilon_o'' + \epsilon_\ell'') A \qquad (4.13b)$$

The boundary conditions, including the continuity conditions at the interface between active and passive regions are

1^o $\quad A = 0 \quad$ at $x = 0, L$ (4.14a)

2^o $\quad A$ is continous at $x = d$ (4.14b)

3^o $\quad \frac{1}{A} \frac{dA}{dx}$ is continuous at $x = d$ (4.14c)

Appropriate solutions are of the form

$A = \sin px \quad$ for $0 \leq x \leq d$ (4.15a)

$A = C \sin q(x-L) \quad$ $d < x \leq L$ (4.15b)

where p, q, C are complex.

Substitution in the wave equation (4.13) gives

$$-p^2 = (\beta^2 - \epsilon_o' \frac{\omega^2}{c^2}) + i \frac{\omega^2}{c^2} (\epsilon_o'' - \epsilon_g'') - \frac{\omega^2}{c^2} \delta\epsilon \qquad (4.16a)$$

$$-q^2 = (\beta^2 - \epsilon_o' \frac{\omega^2}{c^2}) + i \frac{\omega^2}{c^2} (\epsilon_o'' + \epsilon_\ell'') \qquad (4.16b)$$

subject to the following boundary conditions on the field and its derivative

$$\sin pd = C \sin q(d-L)$$

$$\frac{p}{q} = \frac{\tan pd}{\tan q(d-L)}$$

The purpose of the derivation is to solve for the allowed transverse modes and calculate the gain α_g necessary to maintain threshold as a function of the parameters d, L, α_s, α_o, $\delta\epsilon$. The following substitution is made so that the various parameters can be expressed in terms of three normalized independent parameters Q, R, η.

$$u + i\,k = p\,d \qquad (4.17a)$$

$$v + i\,s = q\,d \qquad (4.17b)$$

$$G = \frac{\omega^2 d^2}{c^2} (\epsilon_g'' - \epsilon_o'') = \frac{2\pi n d^2}{\lambda_o} (\alpha_g - \alpha_o) \qquad (4.17c)$$

$$Q = \frac{\omega^2}{c^2} d^2 (\epsilon_\ell'' + \epsilon_o'') = \frac{2\pi n d^2}{\lambda_o} (\alpha_s + \alpha_o) \qquad (4.17d)$$

$$R = \frac{\omega^2}{c^2} d^2 \delta\epsilon \qquad (4.17e)$$

$$\Delta = (\varepsilon_o \frac{\omega^2}{c^2} - \beta^2)\, d^2 \qquad (4.17f)$$

$$\eta = 1 - L/d \qquad (4.17g)$$

The wave equations become

$$(u + i\,k)^2 = \Delta + i\,G + R$$

$$(v + i\,s)^2 = \Delta - i\,Q$$

or separating real and imaginary parts

$$u^2 - k^2 = \Delta + R \qquad (4.18a)$$

$$2\,k\,u = G \qquad (4.18b)$$

$$v^2 - s^2 = \Delta \qquad (4.18c)$$

$$2\,s\,v = -\,Q \qquad (4.18d)$$

Similar substitution in the continuity condition for the derivative and separation into real and imaginary parts yield

$$\frac{u\,v + k\,s}{v^2 + s^2} = \frac{\sin 2u \sin 2\eta v + \sinh 2k \sinh 2\eta s}{4(\cosh^2 k - \sin^2 u)(\sin^2 \eta v + \sinh^2 \eta s)} \qquad (4.19a)$$

$$\frac{k\,v - u\,s}{v^2 + s^2} = \frac{\sinh 2k \sin 2\eta v - \sin 2u \sinh 2\eta s}{4(\cosh^2 k - \sin^2 u)(\sin^2 \eta v + \sinh^2 \eta s)} \qquad (4.19b)$$

The relations resulting from the wave equation (4.18a,c,d) can be used to express the variables v and s in terms of u and k

$$v = [\tfrac{1}{2}\{[(u^2 - k^2 - R)^2 + Q^2]^{1/2} + u^2 - k^2 - R\}]^{1/2} \qquad (4.20a)$$

$$\tilde{s} = -\left[\frac{1}{2}\left\{\left[(u^2 - k^2 - R)^2 + Q^2\right]^{1/2} - (u^2 - k^2 - R)\right\}\right]^{1/2} \tag{4.20b}$$

Thus the boundary condition (4.19) gives a system of two equations in two unknowns u and k which can be solved numerically with the help of a computer as a function of the normalized independent parameters Q, R, η which are expressions respectively of the absorption, refractive index difference and ratio of active region to total thickness. The (u, k) pairs which satisfy both equations simultaneously represent laser mode solutions.

These solutions allow us to calculate the near-field pattern as a function of depth for given material parameters such as α_s, α_o, $\delta\varepsilon$, d, L, and, (through (4.18b) and (4.17c)) the gain α_g required to support such a mode which is stable in time. A few words are in order to clarify the meaning of this gain and its relationship to the normalized gain G and other parameters. Write (4.17c) and (4.17d) as

$$G = (\alpha_g - \alpha_o)/g_o \equiv \alpha_d/g_o \tag{4.17c'}$$

$$Q = (\alpha_s + \alpha_o)/g_o \equiv \alpha_p/g_o \tag{4.17d'}$$

where $$g_o = \frac{\lambda_o}{2\pi n d^2}$$

Physically, we know that the gain α_g at lasing threshold must be sufficiently high to offset the losses, which can be divided into two parts. A first portion of the gain is required to compensate for nonresonant losses α_o

which are present in the active region. The only other loss that must be overcome is the loss due to radiation leaving the active region by diffraction. This part we call the diffraction loss α_d and define it by (4.17c'). Therefore, the normalized gain G is equal to the diffraction loss α_d, within a multiplying factor g_o. (Note that g_o is similar to the expression for the diffraction angle produced by a slit of width d except for the extra factor $2\pi d$ in the denominator). Since (4.17') is the only other equation in which α_o appears, and since it always appears in combination with α_s, we conclude that, as far as absorption is concerned, the normalized gain G, and hence the diffraction loss α_d, depend only on the total absorption in the passive region α_p (defined by (4.17d')) and are independent of the specific distribution of losses between α_s and α_o.

The merit of such a realization is that, in our investigation, it is unnecessary to consider in detail independent variation of α_s and α_o. For example, if we have calculated how α_g varies as a function of the refractive index step $\delta\epsilon$ for $\alpha_o = 0$ and a given value of α_s, say α_s^o, for any other combination of α_s and α_o which add up to the same total $\alpha_s + \alpha_o = \alpha_s^o$, the gain α_g will still vary the same way with $\delta\epsilon$ to within an additive constant α_o and the solution pair (u, k), the near and far fields will remain the same.

4.2 Analysis of Theoretical Results

4.2.1 Diffraction Loss

There are many possible solutions for any given set of parameters. They correspond to transverse modes of various orders, that is modes with different number of maxima between the pumped surface and the epi-layer interface. In a study of lasing effects, the most important modes are obviously those which exhibit low loss. In most cases, these modes have a single maximum in the active region and correspond to solutions for which u, the normalized spatial frequency, lies in the range $\pi/2$ to π. Let us determine the dependence of the diffraction loss of the lowest loss mode on the various cavity parameters.

Figure 11 shows the variation of the diffraction loss G as a function of the refractive index R in terms of normalized parameters for a passive loss Q = 1 and various ratios of epi-layer to active region thickness. To facilitate the interpretation of the results, a second set of axes is shown in which typical physical parameters α_d and $\delta\varepsilon$ have been used for a particular active region thickness d = 2.5 μm. For comparison, the results derived from a similar model for an infinitely thick cavity are also shown (see Appendix D for derivation).

The diffraction loss and hence the gain required for lasing decreases with increasing index change, i.e. with

Fig. 11: Normalized diffraction loss, or equivalently, gain necessary to reach lasing threshold as a function of the normalized refractive index step for a passive loss Q = 1 and for various ratios of epi-layer to active region thickness. A second set of axes is shown in which physical parameters α_d and $\delta\varepsilon$ have been used for a typical active region thickness d = 2.5 μm and λ = .84 μm, n = 3.6. In this case, Q = 1 corresponds to a passive loss α_p = 59.4 cm^{-1}.

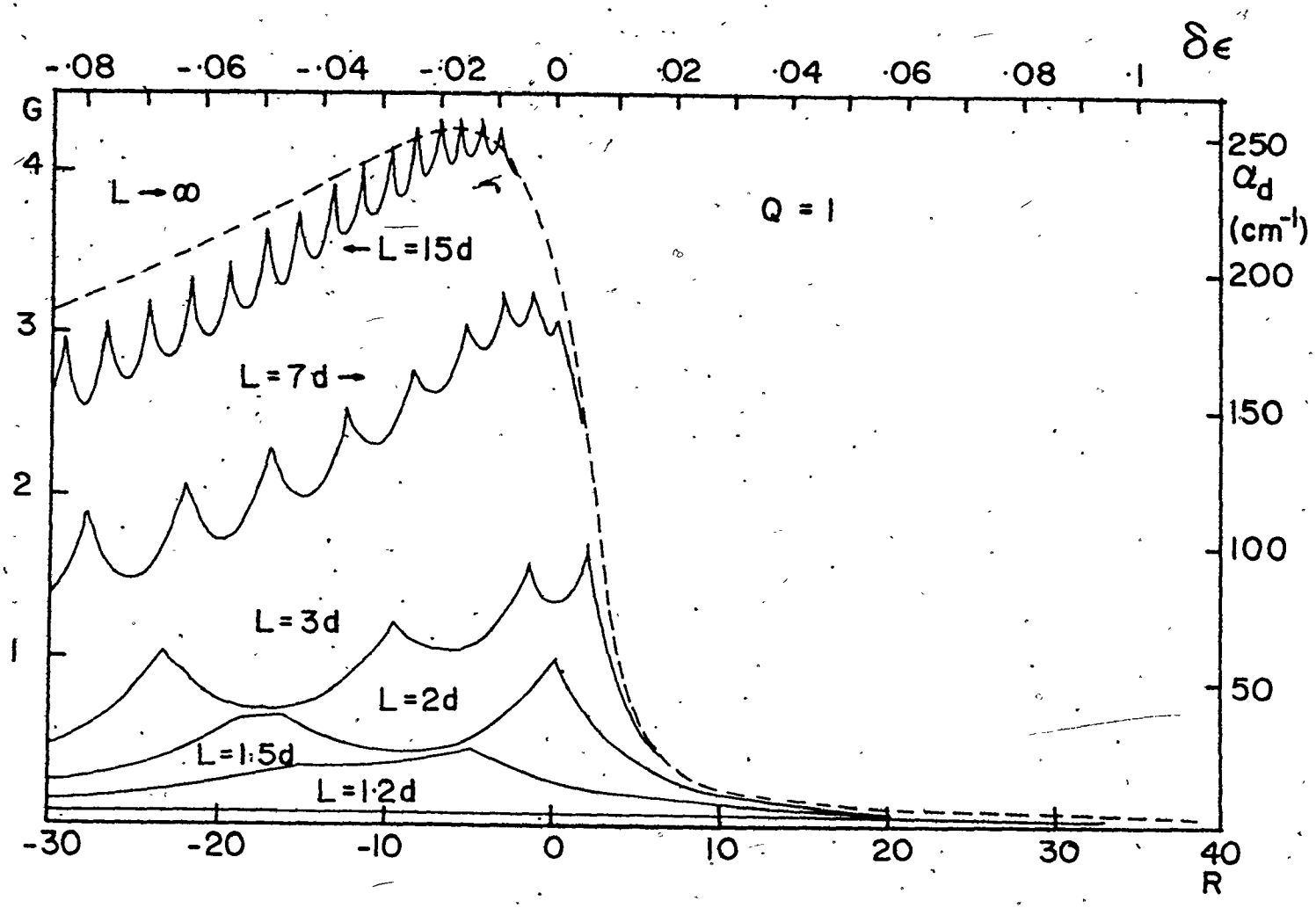
δε
-·08
-·06
-·04
-·02
0
·02
·04
·06
·08
·1
G
4
3
2
1
L→∞
←L=15d
L=7d→
L=3d
L=2d
L=1·5d
L=1·2d
Q = 1
250
α_d
(cm^{-1})
200
150
100
50
-30
-20
-10
0
10
20
30
40
R

improved optical confinement in the active region. For a value of $\delta\epsilon = 0.03$, the diffraction loss has reached low values regardless of the epi-layer thickness. It is also worth noting that the loss decreases with large negative index step, particularly for thicker cavities. A study of this effect as a function of the passive loss Q shows that the diffraction loss decreases with increasing absorption in the passive region. This is akin to optical confinement by the imaginary part of the permittivity. Such behaviour is characteristic of this model. A sech^2 profile for the refractive index distribution always leads to larger losses with increasingly negative index change.

For thick epi-layers, the diffraction loss exhibits a number of local minima. This arises because the attenuation suffered by each mode reaches a minimum for a different value of the refractive index step. Hence, as $\delta\epsilon$ varies, modes of various orders become, in succession, the lowest-loss mode. For example, consider the curve L = 7d in Fig. 11. Each individual section in the shape of a cusp corresponds to the range over which a particular mode is the lowest-loss mode.

It is also quite evident that the diffraction loss increases with epi-layer thickness L. For values of L much larger than fifteen times the active region thickness, the dependence of the loss on the refractive index becomes very

similar to that of an infinitely thick cavity. This is quite understandable. The further away the back reflecting surface, the larger the attrition suffered by the radiation and hence the smaller the intensity of the light that makes its way back to the active region to reinforce the radiation there. The same argument holds as the absorption in the passive region increases for a given value of L. Figure 12 exemplifies such an effect. The diffraction loss is again displayed as a function of the refractive index but the absorption is now ten times larger. For a given L, the diffraction loss has increased significantly with the larger absorption and for a value of L only three times the active region thickness, the losses are already equivalent to those of an infinite cavity and do not increase further with increasing L. Observe also that large refractive index changes are required to reduce the loss to a value equivalent to the preceding case (Q = 1). That is to say, even if the absorption has a confining effect for negative refractive index changes, it has the opposite effect when the index change is positive.

The relationship between the diffraction loss and the various optical parameters discussed above will strongly affect the lasing behaviour of the epi-layer cavity. In Chapter 2 and 3, the effect of the refractive index change on the time delay to threshold variations were demonstrated

Fig. 12: Normalized gain necessary to reach lasing threshold as a function of the normalized refractive index step for a passive loss Q = 10 and for various ratios of epi-layer to active region thickness. A second set of axes is shown in which physical parameters α_d and $\delta\varepsilon$ have been used for a typical active region thickness d = 2.5 μm and λ = .84 μm, n = 3.6. Q = 10 corresponds to a passive loss α_p = 594 cm^{-1}.

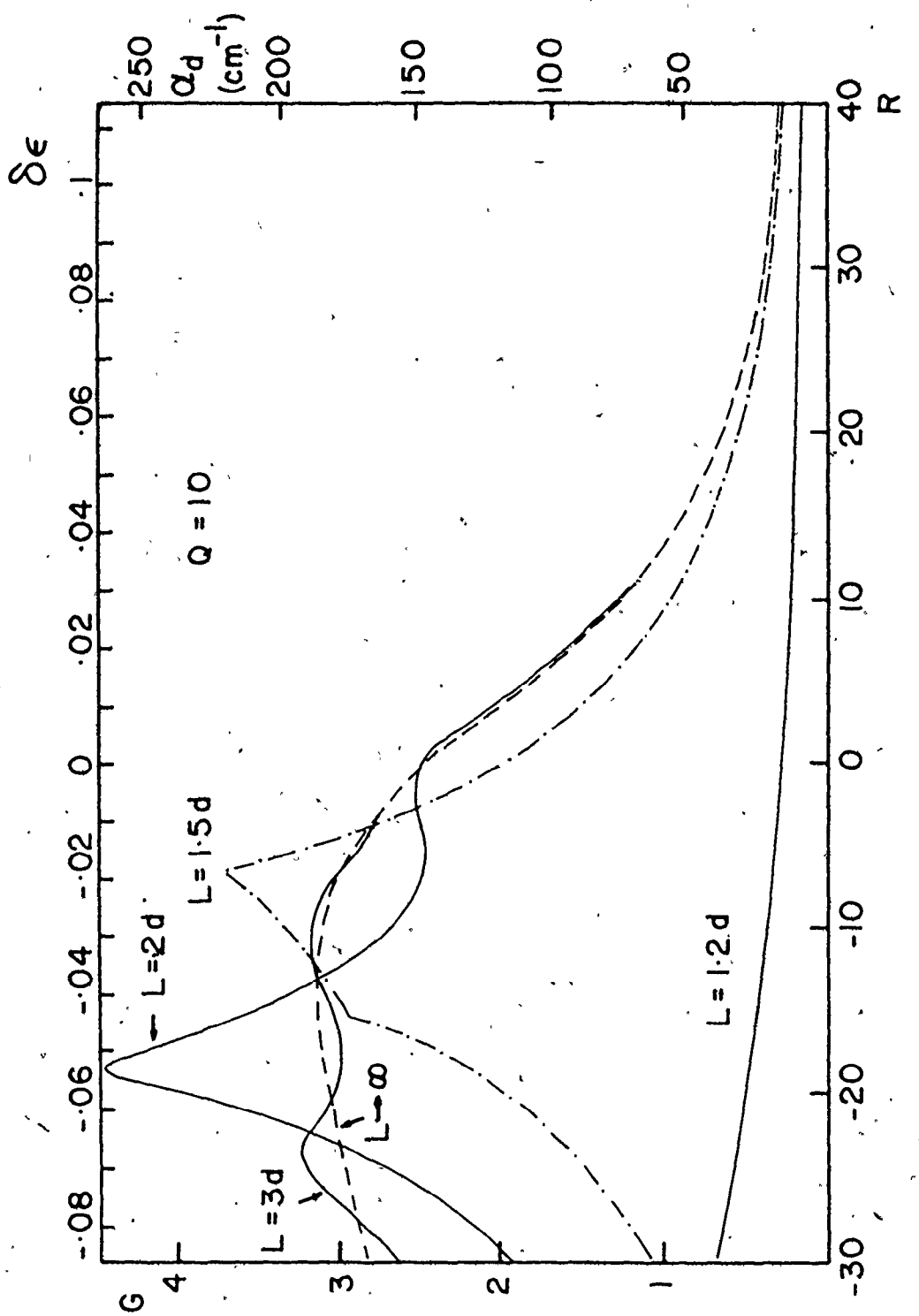
δε
α_d (cm^{-1})
250
200
150
100
50
R
40
30
20
10
0
-10
-20
-30
.1
.08
.06
.04
.02
0
-.02
-.04
-.06
-.08
G
4
3
2
1
Q = 10
L = 2d
L = 1.5d
L = 3d
L → ∞
L = 1.2d

for bulk materials. In this case, the combined effect of the temperature rise (positive contribution) and the dispersion due to the presence of gain (negative contribution) on the refractive index result in an increasing refractive index difference between the active and passive regions which can bring about a sizeable decrease in cavity losses and possibly lasing long after the gain itself has reached equilibrium. On the other hand, the theoretical results just presented show that, for layers of the order of the active region thickness, there is very little variation in diffraction loss with either refractive index or absorption changes. Therefore, the time delays to threshold would not be expected to exceed by much the minority carrier lifetime. This was also observed experimentally. There is an intermediate range of L and Q for which the presence of the epi-layer interface has an effect on the diffraction loss as exemplified by the reduced loss compared to that of an infinite cavity. However, the variations in refractive index still affect the cavity loss and sizeable reductions are observed for increasing R. The mechanism necessary for long time-delay-to-threshold behaviour is therefore present and the near-field intensity distribution has behaviour characteristic of optically confined epi-layers, such as oscillatory fine structure. This produces associated details in the angular distribution of the far-field

patterns as will be shown experimentally later.

4.2.2 Transition from Finite to Infinite Cavity

Comparison of the results for finite and infinite cavity has shown that they tend to converge as the epi-layer thickness, the refractive index step and the absorption increase. This raises an important question. In an epi-layer, under what condition does the effect of the reflecting interface become negligible? Obviously, this depends on the three parameters Q, R, η or, in terms of physical parameters, on the refractive index change $\delta\varepsilon$, the absorption in the passive region α_p, the epi-layer thickness L and the active region thickness d. As a first step, let us determine the condition imposed on L which marks the transition from a finite to an infinite cavity behaviour.

A glance at the theoretical derivation shows that the finite and infinite cavity solutions (Section 4.1 and Appendix D) followed identical paths except for the form of the trial solution and the resulting expression for the boundary condition. For the finite cavity, the latter contains extra terms in $\eta=(1 - L/d)$ which are directly related to the position of the reflecting interface. As L increases, η becomes increasingly negative. The corresponding trigonometric functions stay bounded in the range -1 to +1, but the hyperbolic functions in ηs become increasingly positive (remember from (4.20) that $s<0$).

Thus, we can approximate the hyperbolic function of η by an exponential function and rewrite the boundary condition on the derivative (4.19) as

$$\frac{u\,v + k\,s}{v^2 + s^2} = \frac{\sin 2u \sin 2\eta v + \sinh 2k \exp(2\eta s)/2}{4(\cosh^2 k - \sin^2 u)(\sin^2 \eta v + \exp(2\eta s)/4)}$$

$$\frac{k\,v - u\,s}{v^2 + s^2} = \frac{\sinh 2k \sin 2\eta v - \sin 2u \exp(2\eta s)/2}{4(\cosh^2 k - \sin^2 u)(\sin^2 \eta v + \exp(2\eta s)/4)}$$

As ηs increases, the terms associated with the exponential predominate and the exponential factors in the numerator and denominator cancel. The resulting expressions are identical to the boundary condition for the infinite cavity, that is, for large ηs, the solution for the finite cavity will be identical to the infinite cavity solutions. The requirement is that the product ηs be larger than some constant, say m, which makes the hyperbolic functions much larger than the trigonometric functions, i.e.

$$\eta s > m$$

A choice of $m = 5$ appears reasonable since, for such a value of the argument, the hyperbolic function of interest in the denominator, $\sinh^2 \eta s$, is equal to $(74.2)^2 = 5506$ which is much larger than any values taken by the sine function. Using the definition for η and s ((4.17g) and (4.20b)), this relation can be rewritten to obtain the conditions imposed on L in order for the effect due to the interface to become negligible.

$$L > d\left[1 - \frac{m}{s}\right] = d\left[1 + \frac{m}{(((\Delta^2 + Q^2)^{1/2} - \Delta)/2)^{1/2}}\right],$$

where Δ is the change in the propagation constant (normalized) and is defined in terms of the other parameters by (4.17f). Let us apply this relation to a few particular cases. Assuming there is no spatial variation of the refractive index, i.e. $\delta\epsilon = 0$, take the case $\alpha_p = 594\ cm^{-1}$, $d = 2.5\ \mu m$, $\lambda_o = .84\ \mu m$ and $n = 3.6$. Strictly speaking, one should then evaluate the solution pair (u, k) for a particular L but generally $u = 2.5$ and $k/u \lesssim 0.2$ are reasonable values for a first approximation. The use of the above relation results in $L > 4d$ as the condition for infinite cavity behaviour. This is in agreement with Fig. 12 where the dependence of α_d on the refractive index step for $L = 3d$ is identical to that of the infinite cavity for $\delta\epsilon \geq 0$. Similarly, if the passive loss is taken as $\alpha_p = 59.4\ cm^{-1}$, the relevant inequality is $L > 25d$ which is in agreement with Fig. 11. It should be pointed out that the above relation is not only applicable to epitaxial layers but to any type of cavity which has a reflecting surface at the back. CdS is an example of another material which has been used in electron-beam-pumped semiconductor laser experiments. The samples often come in the form of thin platelets. The above relation can be used to determine the minimum sample thickness beyond which the back surface of

the device has no bearing on the laser behaviour.

Returning to the theoretical analysis, if the absorption is large ($Q^2 >> \Delta^2$), the above expression can be approximated by

$$L > d + m \left[\frac{2}{\frac{\omega n}{c}\alpha_p + \frac{\omega^2}{c^2}\delta\varepsilon - \left(\frac{u^2 - k^2}{d^2}\right)}\right]^{1/2}$$

The larger the absorption, the smaller the L required to go from the finite to the infinite cavity solution. Moreover, a positive refractive index change $\delta\varepsilon$ emphasizes the effect due to absorption. Note that the condition on L also depends on the mode order through the spatial frequency u/d. Higher order modes are more likely to see the interface because their diffraction loss is larger.

If, on the other hand, $\Delta^2 >> Q^2$ we obtain the following approximation:

$$L > d\left[1 + \frac{2m/\Delta}{Q}\right] = d + \frac{2m\left[(u^2 - k^2)/d^2 - \omega^2\delta\varepsilon/c^2\right]^{1/2}}{\omega n\alpha_p/c}$$

Again, as the passive loss α_p increases, the critical value for L becomes smaller. As the refractive index $\delta\varepsilon$ increases, the argument under the square root quickly becomes negative, the second term becomes imaginary and L is only required to be somewhat larger than d. However, if $\delta\varepsilon$ is becoming increasingly negative, L is required to be larger. This occurs because a negative index change

accentuates the deflection of the propagation direction away from the cavity axis. The light is diffracted at a larger angle and, therefore, is more likely to reach the interface. The same effect results if the mode order is increased.

The inequality $ns > m$ can be used not only to determine the condition on n in order for the effect of the interface to become negligible but it can also be used to determine the conditions on s for a given n, that is the conditions on the refractive index or the absorption, the other parameters being held constant. The expression can be easily rearranged to yield the constraint on the absorption.

$$\alpha_p > \frac{2cm}{\omega n(L - d)} \left[\frac{m^2}{(L - d)^2} - \frac{\omega^2}{c^2} \delta\varepsilon + \frac{u^2 - k^2}{d^2}\right]^{1/2}$$

The minimum absorption necessary in order for most of the diffracted light to be absorbed before it can reinforce the radiation in the active region is most strongly dependent on the thickness of the passive region $(L - d)$. The α_p required also decreases with positive refractive index change and increases with mode order u or more accurately with the spatial frequency in the active region u/d.

The same inequality leads to the following constraint on the refractive index change:

$$\delta\varepsilon > \frac{c^2}{\omega^2}\left\{\frac{u^2 - k^2}{d^2} + \frac{m^2}{(L-d)^2} - \frac{\omega^2 n^2 (L-d)^2 \alpha^2}{4m^2c^2}\right\}$$

The required refractive index change decreases with increasing passive region thickness and absorption, but increases with the spatial frequency u/d.

Up to this point, the dependence of the solutions on the active region thickness d has not been discussed because of the complexity of its effect since it enters into the definition of the normalizing factor, in the parameter η and is also part of the definition for the spatial frequency u/d. Figure 13a shows the diffraction loss as a function of d for a few values of the epi-layer thickness. The change in the refractive index is assumed to be zero and the absorption in the passive region is taken to be 80 cm^{-1}. This corresponds approximately to the equivalent distributed loss of the mirror facets for a cavity 200 μm long plus a small contribution due to band-to-band absorption. This contribution is small because the rise in temperature and the carrier concentration both reduce the band gap energy in the active region with respect to the passive region. Figure 13a demonstrates as expected that the diffraction loss decreases with active region thickness.

It is also of interest to determine the importance of the back reflecting surface on α_d as d varies. Ideally we would want to evaluate the product ηs as a function of d.

Fig. 13: a) Diffraction loss as a function of active region thickness d for four values of the epi-layer thickness and for a semi-infinite cavity.

b) Ratio of the diffraction loss for a finite cavity to that for a semi-infinite cavity as a function of d ($\delta\varepsilon = 0$).

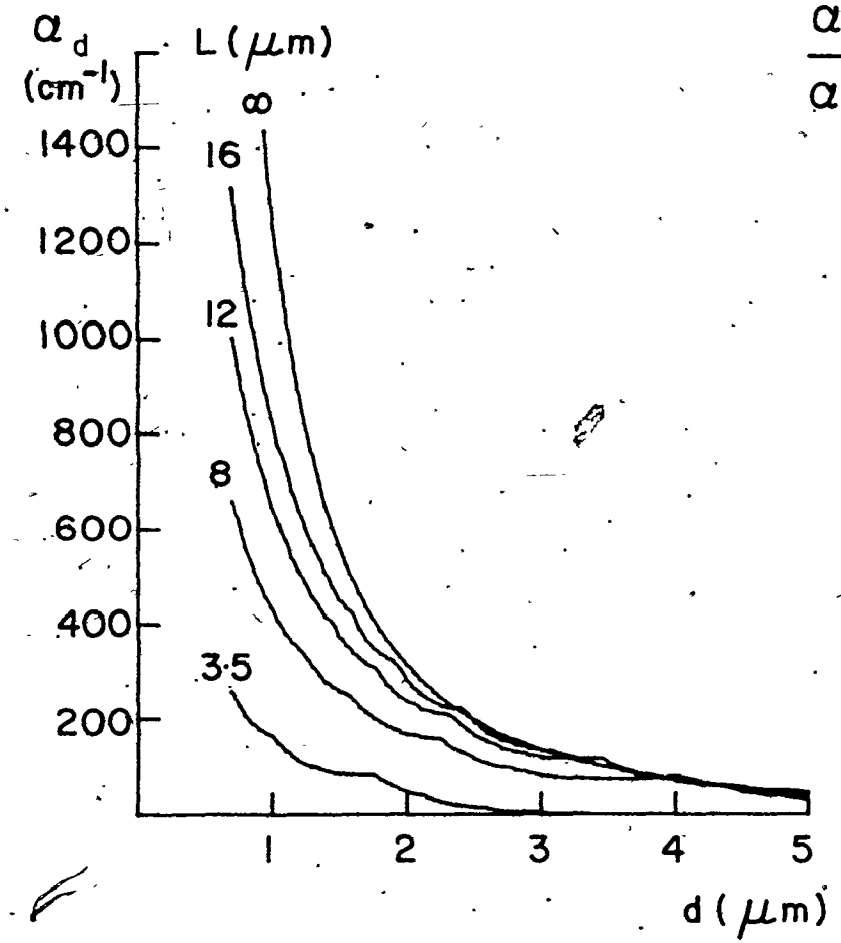
α_d (cm^{-1})
L (μm)
∞
16
12
8
3·5
1400
1200
1000
800
600
400
200
1
2
3
4
5
d (μm)

a

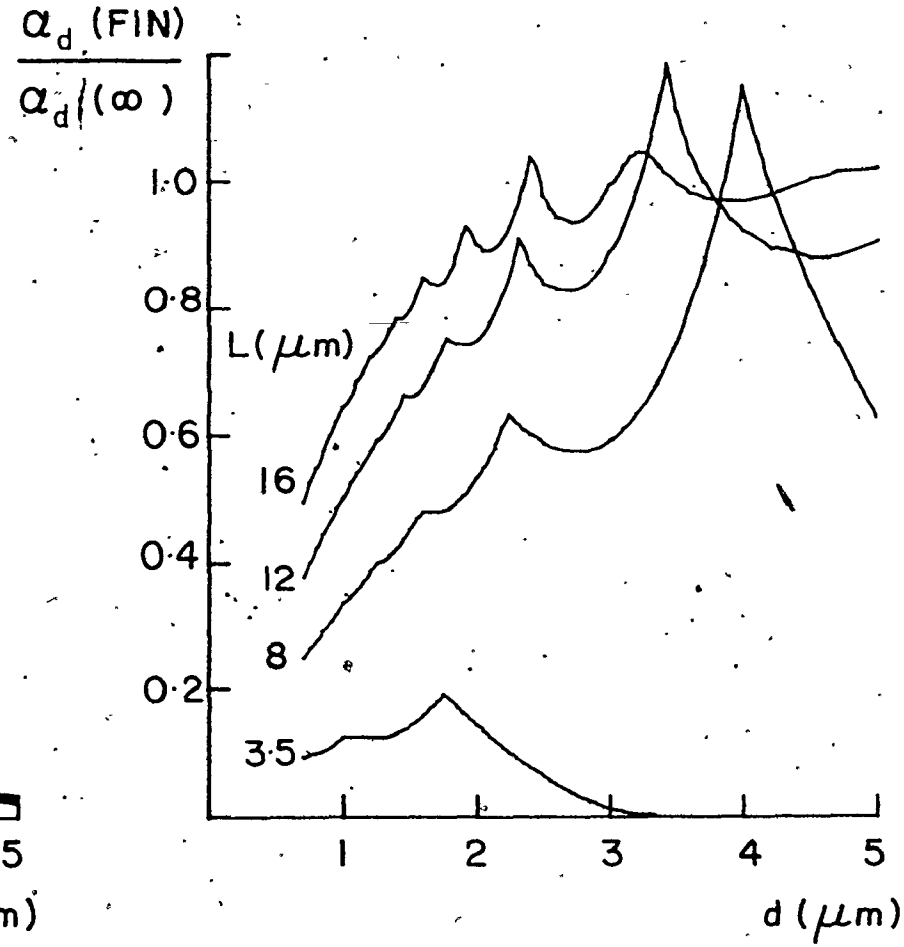
$\frac{\alpha_d\ (FIN)}{\alpha_d\ (\infty)}$
1·0
0·8
0·6
0·4
0·2
L (μm)
16
12
8
3·5
1
2
3
4
5
d (μm)

b

The larger the product, the less the radiation sees the interface. But this factor is not readily interpreted. It is conceptually simpler to think in terms of diffraction loss or gain required for lasing. For this reason, the importance of the interface is determined here by calculating the ratio of the finite cavity diffraction loss to that of the infinite cavity as a function of d. This is illustrated in Fig. 13b. For values of d in the 1 μm range, the ratio increases with d which means that the radiation sees less of the back surface although the active region is getting closer to the interface. This is a somewhat surprising result. It occurs because, for d of the order of λ, the deflection of the radiation into the unpumped region due to diffraction is large but decreases rapidly with increasing d. This effect is more important than the decrease in loss associated with the shift of the active-passive boundary toward the epi-layer interface. Therefore, the relative importance of the interface is reduced. The loss for the finite cavity starts decreasing with respect to that of the infinite cavity as d gets closer to L. Interpreted in terms of the theoretical solution, these variations mean that the effects of d, through the normalizing factor g_o, on the loss Q, the refractive index change R and particularly the spatial frequency u/d predominate for values of d in the range of the wavelength

while the effect on the parameter $n = (d - L)/d$ becomes more important as d approaches L. Sharp increases in the cavity loss occur again in the transition from one transverse mode to another.

To summarize this section, starting with a thin epi-layer, the gain required for lasing increases as the thickness increases. Moreover, it becomes more dependent on the refractive index change which can bring sizeable reductions in losses if sufficiently positive. An increase of the absorption in the active region also results in an increase of the diffraction loss. This loss doesn't increase indefinitely with L. A maximum is reached when the radiation originating in the active region ceases to see the reflecting interface. In that case, the dependence of α_d on the refractive index change becomes identical to that of an infinite cavity model appropriate for bulk material. The conditions necessary to bring the operation of the epi-layer into this regime were determined explicity for the absorption, the refractive index change, the epi-layer thickness, and finally the effect of the active region thickness was discussed at length.

4.2.3 Mode Propagation Direction and Condition for Total Internal Reflection

In Chapter 3, the wavelengths of the optical emission from the epi-layer and the substrate respectively were used to determine successively the change in band gap energy at

the interface and the alloy composition. The resulting change in refractive index at the interface was estimated as $\Delta n = .054$. The solutions to the transverse modes can now be used to determine whether this refractive index step is sufficient to totally confine the radiation within the epi-layer i.e., whether the angle of incidence of the radiation exceeds the critical angle for internal reflection which is given by

$$\theta_c = \sin^{-1}\left(\frac{3.6}{3.654}\right) = 80.1^{o} \quad .$$

The propagation direction of the radiation depends on the propagation constant along the cavity axis, β, and the propagation constant normal to the axis, u/d in the active region or v/d in the passive region. By making use of (4.17f) and (4.18a), the following expression for β is obtained

$$\beta = \left\{\frac{\omega^2}{c^2}(\epsilon_o' + \delta\epsilon) - \frac{(u^2 - k^2)}{d^2}\right\}^{1/2} \quad .$$

For a given transverse mode, β can be calculated once the corresponding (u, k) pair solution has been obtained for a specific combination of parameters. In the active region, the propagation direction with respect to the normal to the interface is then given by

$$\theta_{act} = \tan^{-1} \left(\frac{\beta}{u/d}\right) .$$

Similarly, in the passive region, the propagation direction is

$$\theta_{pass} = \tan^{-1} \left(\frac{\beta}{v/d}\right)$$

The propagation direction in the passive region for a number of representative cases are given in Table III. For all those modes, which are typical of the ones observed experimentally, the angle which the propagation direction makes with the normal to the epi-layer interface exceeds the critical angle for internal reflection. This justifies the assumption made at the beginning of the theoretical development. Only when the transverse spatial frequency is very large (large mode order), for large negative $\delta\epsilon$ do we encounter incidence angles which would not lead to internal reflection.

4.2.4 Near- and Far-Field Patterns.

Once a solution is obtained for a combination of cavity parameters, the transverse distribution of the complex field amplitude is given by (4.15). Taking the magnitude of this expression yields

$$|A| = \left[\sin^2 \frac{ux}{d} + \sinh^2 \frac{kx}{d}\right]^{1/2} \quad \text{for } 0 < x < d$$

$$|A| = |C| \left[\sin^2 v \left(\frac{x - L}{d}\right) + \sinh^2 s \left(\frac{x - L}{d}\right)\right]^{1/2} \quad \text{for } d < x < L$$

TABLE III: Comparison between the critical angle for internal reflection at the epi-layer interface (80.1^{o}) and the angle of incidence of the lasing modes propagating in the passive region. The modes selected are typical of the ones observed experimentally. They were calculated for a passive loss of 80 cm^{-1}, λ = .84 μm and n = 3.6

$\delta\varepsilon$	d(μm)	L (μm)	mode order	θ_{pass}
0.	2.5	3.5	1	88.07
			3	84.26
-0.01	1.5	12.	6	86.59
			10	84.41
0.0	1.5	12.	6	86.68
			10	84.42
0.01	1.5	12.	6	86.88
			10	84.44
0.1	1.5	12.	1	89.87
			10	84.71
0.0	2.5	12.	3	88.26
			6	86.66
			10	84.43
0.0	3.5	12.	2	88.62
			6	86.66
			10	84.43
0.0	2.5	16.	4	88.22
			10	85.81

The amplitude of the lowest-loss mode as a function of depth is illustrated in Fig. 14 for a 17.5 μm thick cavity having a 2.5 μm active region, a passive loss of 60 cm^{-1} for four values of the refractive index step. These solutions were chosen from the curve L = 7d in Fig. 11. The corresponding near field for an infinite cavity is also shown for comparison. The vertical axis marks the position of the boundary between pumped and unpumped regions. As the refractive index increases, the optical confinement within the active region improves. For example, at $\delta\varepsilon = 0.01$, strong indications of optical waveguiding appear concurrent with a sizeable reduction in cavity loss as can be seen from Fig. 11. The spatial frequency in the passive region decreases with respect to that of the active layer producing a change in the order of the lowest-loss mode.

For large values of the index step, the finite cavity profile becomes identical to that of the infinite cavity because the radiation is so well confined that practically no light reaches the epi-layer interface. If the thickness of the cavity is increased while the active region thickness is held constant, the spatial frequency in the passive region stays approximately the same but the number of maxima increases while an increase in d leads to a reduction in spatial frequency. The dependence of the near field on the passive loss is somewhat predictable, the intensity

Fig. 14: Transverse electric field distribution for a 17.5 μm thick cavity and a semi-infinite cavity excited to a depth d = 2.5 μm for four values of the permittivity step. The passive loss is α_p = 60 cm^{-1}.

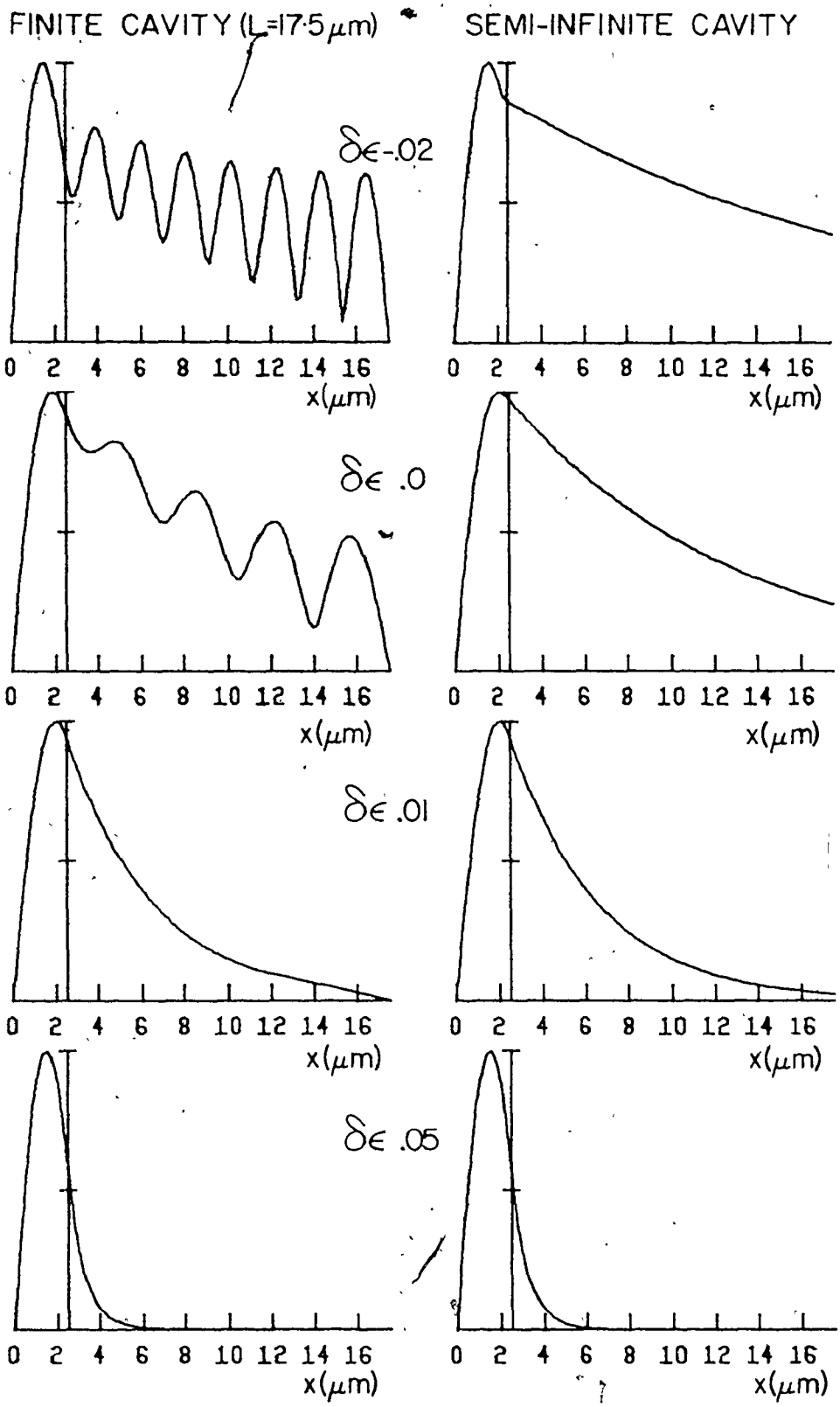
FINITE CAVITY (L=17.5μm)
SEMI-INFINITE CAVITY
δε-.02
δε .0
δε .01
δε .05
0 2 4 6 8 10 12 14 16
x(μm)

decreasing faster with depth.

Because the vacuum chamber did not permit close access to the laser sample, we chose to measure the far-field pattern produced by the emitted radiation. The angular distribution of the intensity in the far field can be computed by taking the Fourier transform of the near-field intensity distribution (see Appendix E). Examples of angular distribution are shown in Fig. 15 for the same parameters as in Fig. 14. The most striking differences between the far fields calculated for finite and infinite cavities are evident at low absorption and refractive index step. Under those conditions, aside from the major peak in the quadrant away from the electron beam which is common to both models, the finite cavity exhibits a secondary peak symmetrically disposed about the cavity axis together with a number of regularly spaced minor peaks or ripples between the two major peaks. Note that for a negative index change, the far field for the infinite cavity is much narrower because the radiation distribution at the emitting facet extends further into the crystal effectively acting as a wider source.

As the refractive index grows, a shift of the two major peaks toward the cavity axis is observed, in conjunction with a reduction in the number of ripples (shift to lower order mode) and the secondary peak intensity

Fig. 15: Angular distribution of the far-field intensity for a 17.5 μm thick cavity and a semi-infinite cavity excited to a depth d = 2.5 μm for four values of the permittivity step. The passive loss is α_p = 60 cm^{-1}.

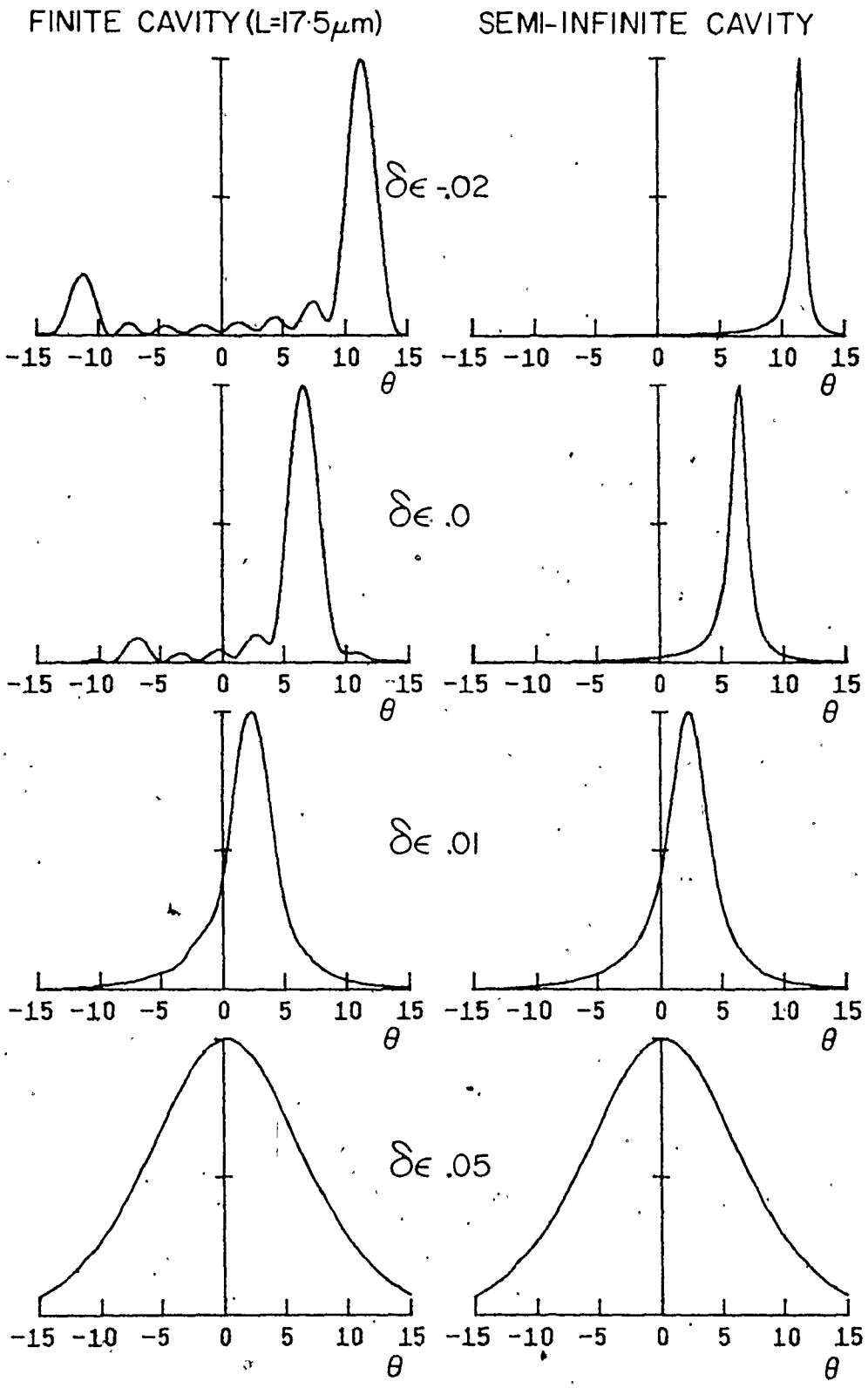
FINITE CAVITY (L=17·5μm)
SEMI-INFINITE CAVITY
δε -.02
δε .0
δε .01
δε .05
-15 -10 -5 0 5 10 15
θ

decreases. Ultimately, the active region becomes optically confined and the far fields for finite and infinite cavities become identical.

Figure 16 illustrates how the far-field is affected by a reduction of the cavity thickness. An increase in the ripple separation is observed concurrent with a decrease in the number of ripples. However, particularly evident for the thinner active region $d = 1.5$ μm is the fact that the angular separation between the primary and secondary peaks remains approximately constant. This is because the spatial frequency within the epi-layer doesn't change appreciably. For L larger than a few d, the spatial frequency is determined primarily by the active region thickness and the refractive index step.

The far-field patterns described above can be correlated easily to the angular distribution of intensity produced by multiple slits. Consider a set of N slits at interval a. If the light is incident normal to the plane of slits, the dependence of the far-field intensity on the angle γ due to the interference factor is $\sin^2(\pi\gamma Na/\lambda)/\sin^2(\pi\gamma a/\lambda)$. Primary maxima occur for $\gamma a/\lambda = 0, \pm 1, \ldots$ or $\Delta\gamma = \lambda/a$. In other words, the separation between the primary maxima is inversely proportional to the slit separation or, by analogy with the modes of an epi-layer, proportional to the spatial frequency or mode order. The diffraction term

Fig. 16: Angular distribution of the far-field intensity for two values of the active region thickness (d = 1.5, 2.5 μm) and four values of the cavity thickness. The passive loss is $\alpha_p = 80\ cm^{-1}$ and the permittivity step is $\delta\varepsilon = 0$.

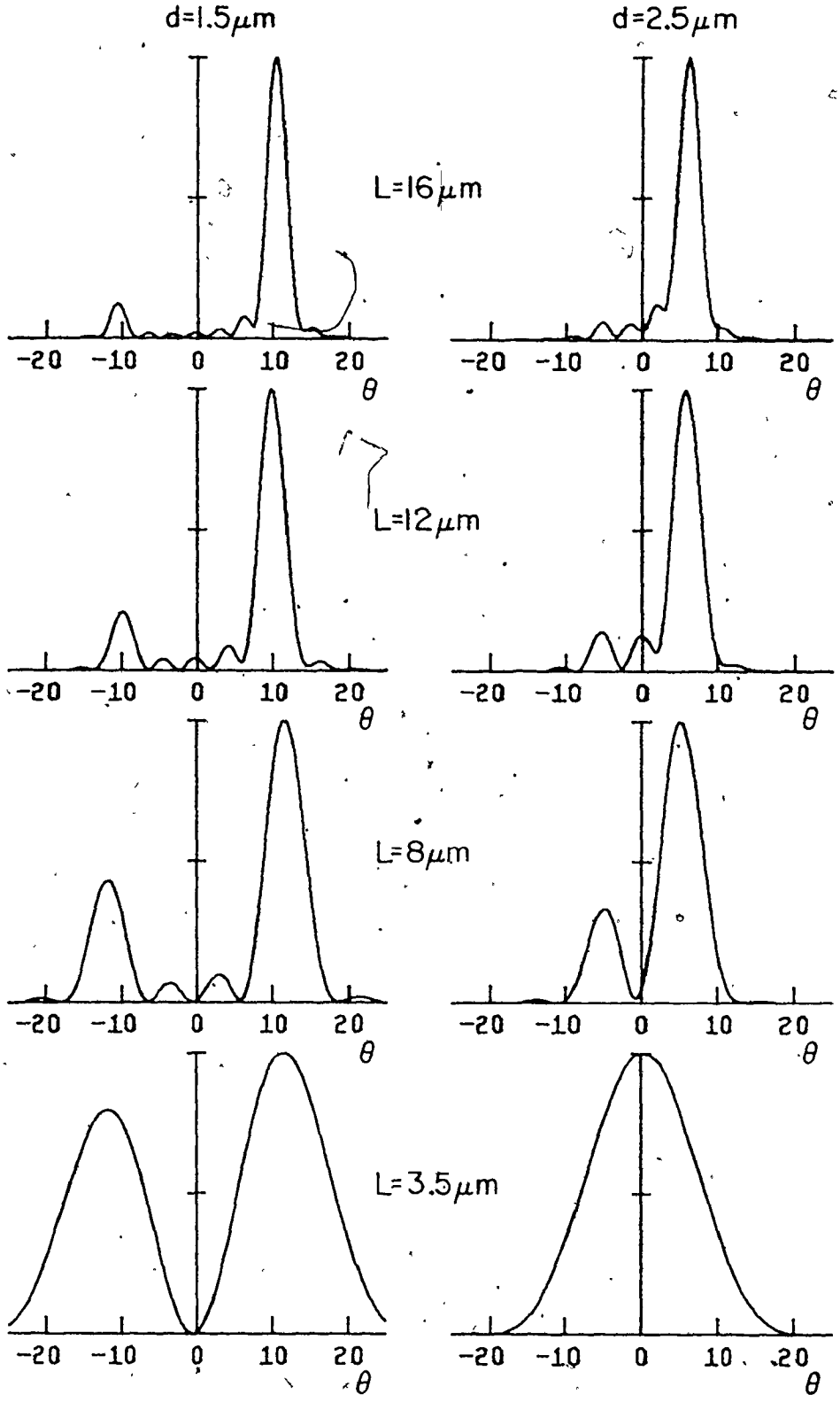
d=1.5μm
d=2.5μm
L=16μm
L=12μm
L=8μm
L=3.5μm
-20 -10 0 10 20
θ

has minima for $\gamma a/\lambda = i/N$ ($i \neq 0, N, 2N$). The angular separation between minima is then $\Delta\gamma = \lambda/Na$. But $(N-1)a$ is the overall width of the set of slits. Therefore, if N is large, the secondary maxima separation is inversely proportional to the overall width of the set of slits or, applied to our lasing cavity, inversely proportional to the epi-layer thickness. Furthermore, the mode order is equal, in the far field, to the number of secondary maxima plus 2. Obviously, as the lasing cavity diverges further from a homogeneous cavity with increasing index step or absorption, the far field diverges further from this idealized picture. In particular, a larger absorption leads to a smaller near-field intensity at the interface which is reflected, in the far-field by a smaller intensity of the secondary peak.

Finally, on the basis of the preceding discussion, we conclude that, even though both the threshold gain and the far-field distribution are affected by the reflecting surface, the far field would seem to be a more sensitive parameter to determine the presence of the permanent waveguide effects because experimentally observable features of the angular distribution characteristic of a finite cavity (such as secondary peak and regularly spaced ripples) persist even when the dependence of the gain on the refractive index step has become experimentally indistinguishable from that of the bulk material. This is because

our means of probing the gain, the measurement of the time delay to threshold, is sensitive to the dynamics of the diffraction loss but not to its permanent change, for L a few times larger than d. Thus, in that range, transient waveguide effects can be detected experimentally by measurements of the time delay to threshold but not permanent waveguide effects.

4.3 Electromagnetic Models for a Cavity of Semi-Infinite Thickness.

In Section 4.2, we studied the dependence of the diffraction loss on the various cavity parameters in a thin confined layer. The presence of the epi-layer interface, however, masks the transient waveguide effects. In this section, we examine briefly the calculated results for two models which assume the cavity to be semi-infinite, firstly because of their greater simplicity, and secondly, to determine how the results are profile dependent. Consider first a bulk sample of semi-infinite thickness in which the transverse distribution of the permittivity is approximated by a step function [15]. The derivation in Appendix D shows that the number of independent normalized parameters is now reduced to two, one proportional to the refractive index step, the other proportional to the absorption. As in Section 4.1, $\lambda/2\pi nd^2$ remains the normalizing parameter.

Figure 17 illustrates the diffraction loss as a

Fig. 17: Gain necessary to reach lasing threshold as a function of the refractive index step for four values of the absorption calculated using the step model for a cavity semi-infinite in thickness. One set of axes is labelled in terms of the normalized parameters G and R, the other in terms of the physical parameters α_d and $\delta\varepsilon$ for the particular case λ = .84 μm, n = 3.6, d = 2.5 μm.

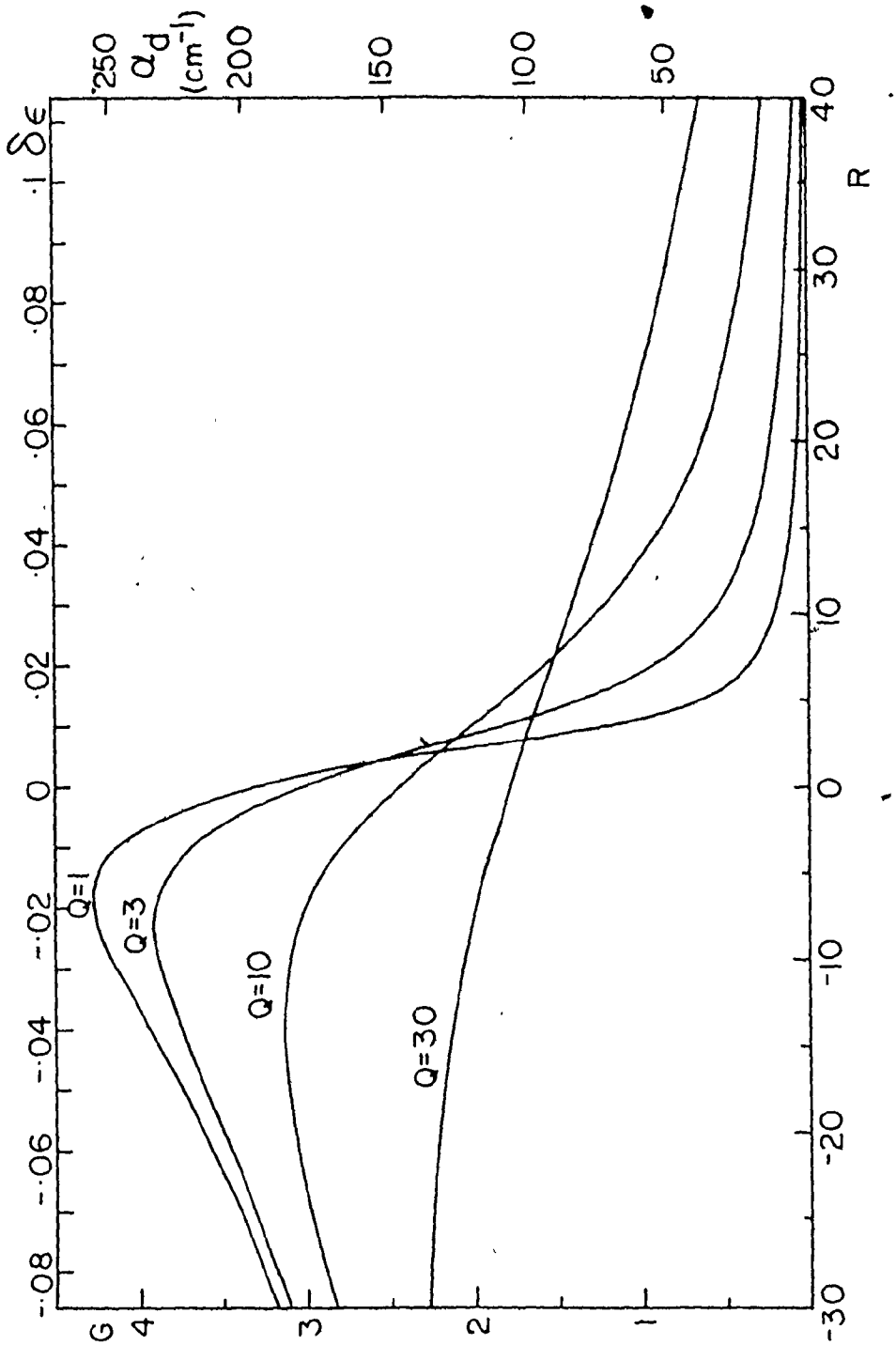
250
200
150
100
50
α_d (cm^{-1})
.1
.08
.06
.04
.02
0
-.02
-.04
-.06
-.08
$\delta\epsilon$
40
30
20
10
0
-10
-20
-30
R
Q=1
Q=3
Q=10
Q=30
G
4
3
2
1

function of the refractive index step for four values of the absorption in the passive region. One set of axes is labelled in terms of the normalized parameters G and R, the other in terms of the more physical parameters α_d and $\delta\epsilon$ for the particular case λ = .84 μm, n = 3.6, d = 2.5 μm. The diffraction loss decreases with increasing refractive index as the radiation becomes confined within the active layer. The effect of the absorption is now clearly seen. It reduces the dependence of the diffraction loss on the refractive index step. For positive $\delta\epsilon$, where α_d is relatively small, a larger absorption leads to a larger diffraction loss. Conversely, for negative $\delta\epsilon$, the relatively large α_d's decrease with increasing absorption.

Another model was used in Chapter 2 to evaluate the time delay to threshold. In that case, the spatial distribution of the permittivity was approximated by a sech^2 function. The transverse mode solution for this profile (given in Appendix C) leads to the dependence of the diffraction loss on the permittivity change illustrated in Fig. 18 for four values of the absorption. The normalizing factor is now $\lambda/2\pi n(d/.88)^2$. This small difference does not affect significantly the comparison with the step model.

The diffraction loss is reduced with increasing refractive index difference as the optical confinement improves. For positive $\delta\epsilon$, the larger the absorption, the

Fig. 18: Gain necessary to reach lasing threshold as a function of the refractive index change for four values of the absorption calculated using the $sech^2$ model. One set of axes is labelled in terms of the normalized parameters G and R, the other in terms of the physical parameters α_d and $\delta\varepsilon$ for the case λ = .84 μm, n = 3.6 and a depth at half-maximum of 2.5 μm.

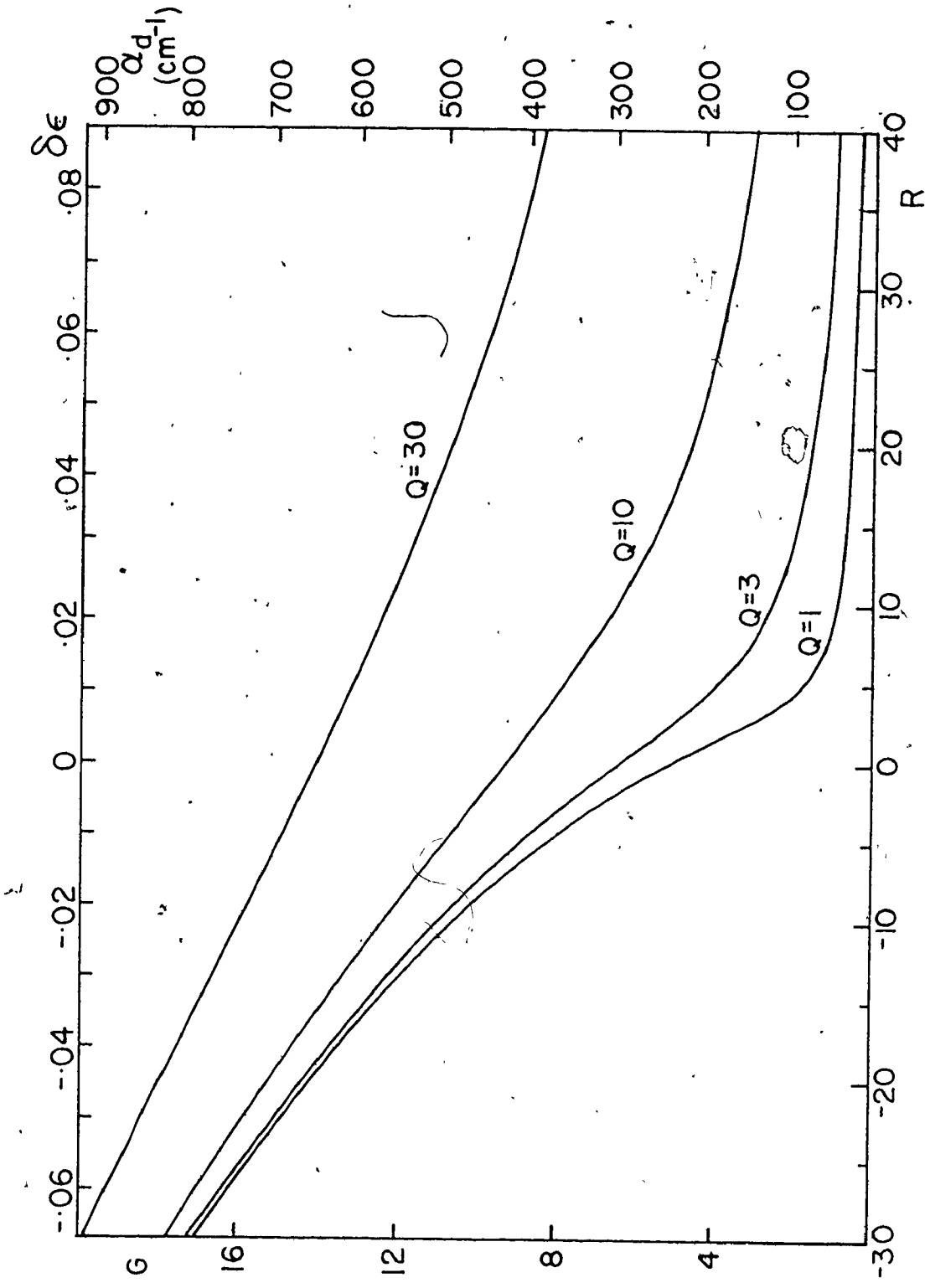
α_d (cm^{-1})
900
800
700
600
500
400
300
200
100
$\delta\epsilon$
.08
.06
.04
.02
0
-.02
-.04
-.06
R
40
30
20
10
0
-10
-20
-30
G
16
12
8
4
Q=30
Q=10
Q=3
Q=1

larger the diffraction loss. Moreover, the dependence on the refractive index is reduced. This behaviour is very similar to that of the step model. The diffraction loss is not reduced for increasingly negative index step nor does it decrease with increasing absorption in that range of index step. Fortunately, large negative refractive index changes are obtained only under conditions such as large gain and small temperature rise which occur only at the beginning of the pulse. In the application of the $sech^2$ solution to the model presented in Chapter 2, we were mainly interested in long t_d where $\delta\epsilon$ is usually positive. Therefore, the differences between the solutions for the step profile and the $sech^2$ profile for negative refractive index changes are not critical. In any case, the model for the time delay to threshold is not expected to be accurate when the time delay becomes of the order of the minority carrier lifetime since, in this range, the time dependence of the minority carrier concentration should be taken into account.

One may note also that the gain required for threshold is approximately twice as large as for the step model. This is due to the fact that the former does not use the gain as efficiently, since the peak of the radiation distribution cannot coincide with the position of the gain maximum. Moreover, the $sech^2$ profile is not quite as effective in confining the radiation. This can be seen in

Fig. 19 where the spatial distribution of the field amplitude is shown for four values of the refractive index change. The absorption is 60 cm^{-1} and the width of the profile was chosen so that, at $d = 2.5$ μm, the function $sech^2$ has fallen to half of its maximum value. Also shown on the same figure are the corresponding far-field diffraction patterns evaluated numerically using Fast-Fourier-Transform techniques.

Comparing with the calculated results of Fig. 14 for the step model we note that, at low $\delta\varepsilon$, the radiation peaks at a greater depth simply because there is no sharp boundary to prevent it from spreading beyond a certain depth as in the step model. However, the resulting far-field patterns do not differ significantly.

Fig. 19: Near- and far-field distributions of the lasing radiation for four values of the refractive index change evaluated using the sech^2 profile to approximate the spatial variation of the refractive index. This profile is shown as a dotted line. The depth at half maximum is 2.5 μm and the absorption in the passive material is 60 cm^{-1} (λ = .84 μm, n = 3.6).

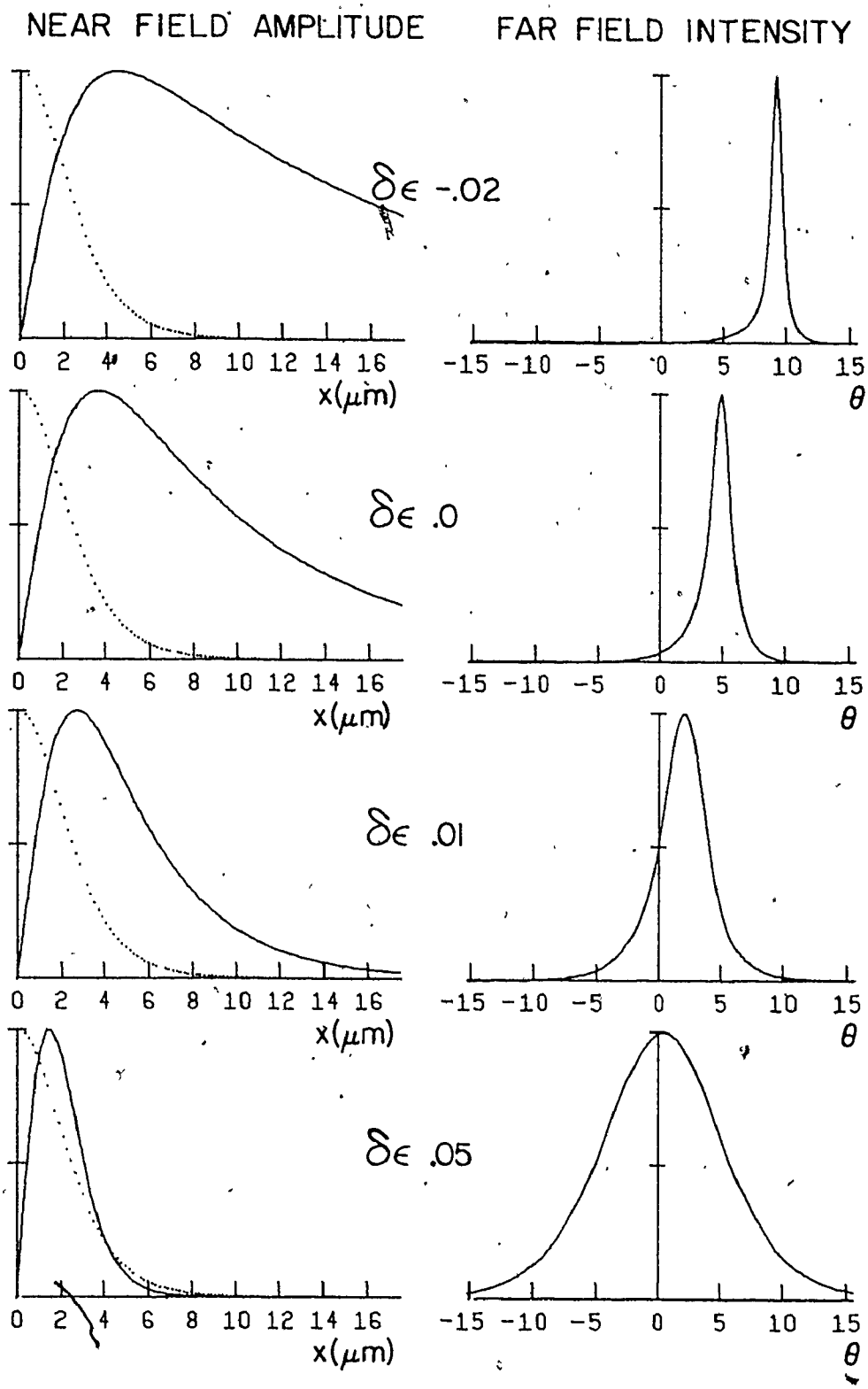
NEAR FIELD AMPLITUDE
FAR FIELD INTENSITY
δε -.02
δε .0
δε .01
δε .05
0 2 4 6 8 10 12 14 16
x(μm)
-15 -10 -5 0 5 10 15
θ

CHAPTER 5

EXPERIMENTAL FAR-FIELD PATTERNS

5.1 Experimental Apparatus

The semiconductor samples were mounted on the cold finger of a liquid nitrogen dewar and pumped using a 200 nsec electron-beam pulse as described in Chapter 3. The far-field patterns were scanned in the plane defined by the electron beam and the cavity axis using a glass fiber bundle (3.2 mm diam.) round-to-slit converter mounted on a support which could rotate about the vacuum chamber axis. A schematic diagram of the apparatus is shown in Fig. 20. The emitted light first passed through a slit (1.3° aperture). A lens integrated the emission in the direction perpendicular to the plane of rotation and focused it on the round aperture of the fibre bundle. The emission from the flat end was fed directly into a 0.5 m Ebert scanning monochromator and detected by a cooled photomultiplier. A sampling oscilloscope was used to display the intensity at any given time after the start of the pumping pulse.

The output window of the vacuum chamber allowed scanning over a range of 50°. The sample mount within the vacuum chamber was free to rotate about the same axis as the goniometer and could translate in the plane of rotation to

Fig. 20: Schematic diagram of the apparatus used to make the time-resolved measurements of the far-field patterns.

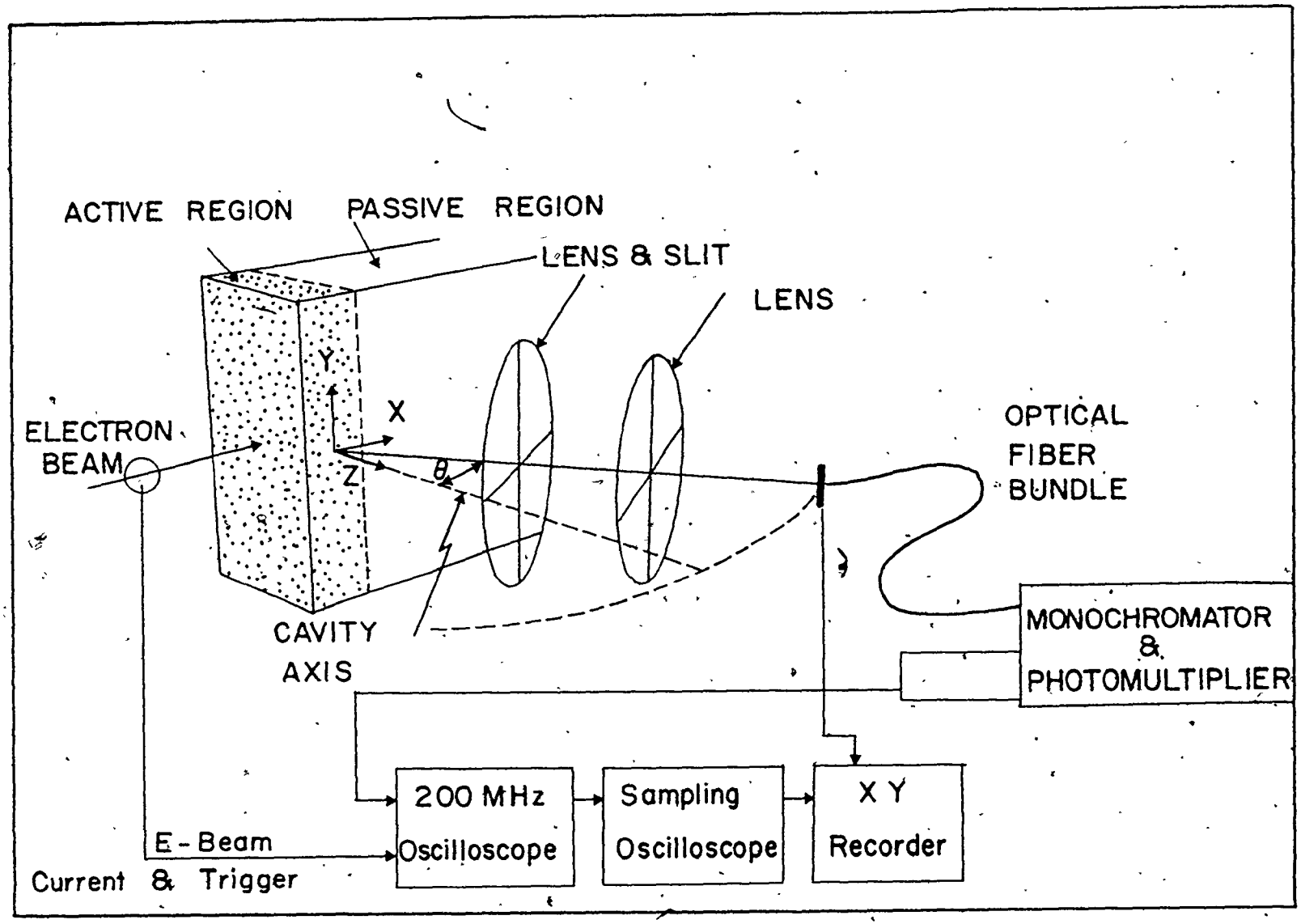
ACTIVE REGION
PASSIVE REGION
LENS & SLIT
LENS
Y
X
Z
θ
ELECTRON BEAM
OPTICAL FIBER BUNDLE
CAVITY AXIS
MONOCHROMATOR & PHOTOMULTIPLIER
200 MHz Oscilloscope
Sampling Oscilloscope
X Y Recorder
E-Beam Current & Trigger

some extent, allowing fine adjustments of the laser position. The orientation of the laser cavity axis was then measured by observing the reflection of a fine pencil of light off the semiconductor mirror facet.

Measurements of the far-field diffraction patterns were generally restricted to times immediately following the onset of lasing because the related theoretical development strictly applies only in that case. The significance of any data taken later on is likely to be obscured by saturation effects and multimode lasing. For instance, if the radiation level in the cavity sufficiently exceeds the threshold level, the radiation in the cavity will affect the gain profile. Consequently, for a given pumping voltage and current, the emitted radiation was first observed over a wide angular and spectral range in order to determine the time and wavelength at which lasing threshold first occurred. The far field was then scanned at these specific times and wavelengths, the monochromator slits now narrowed sufficiently to resolve the longitudinal modes (resolution $\approx$2A). The output of the sampling scope was plotted on an x-y recorder as the goniometer scanned the far field, the angular position being monitored by a wire wound tracking resistor.

The experimental measurements were made on the Zn-doped GaAs ($p = 2 \times 10^{18}$ cm^{-3} at 300^{o}K) bulk crystals and on

the hetero-epitaxial $Ga_xIn_{1-x}As$ layers of 16, 12, 3.5 μm thickness, described in Chapter 3. Only one representative set of data for the bulk sample and the 3.5 μm epi-layer are presented because the same general features were found on other samples. For the 16 and 12 μm epi-layers however, the variations between samples made it difficult to identify one representative example. Therefore, two sets of data for each epi-layer thickness are presented. The variations are attributed to the fact that, for this range of thicknesses, the important fine structures in the near and far fields are strongly affected by small inhomogeneities in the samples whereas the bulk samples and the 3.5 μm epi-layers exhibit gross features which are less affected by crystal inhomogeneities.

5.2 Experimental Results

Figure 21 shows far-field diffraction patterns from a GaAs bulk sample. Illustrated are two far fields for each of three pumping voltages, one measured at the lowest pumping current to bring about lasing and the second taken at a somewhat higher current which leads to a short time delay to threshold (t_d). A negative angle represents a deviation toward the electron beam. Associated with each experimental pattern is a far field calculated using the step model for an infinite cavity. The active region depth

Fig. 21: Experimental and theoretical far-field patterns at lasing threshold from a GaAs bulk sample for a high and a low value of the pumping intensity at each of three accelerating voltages. The parameters for the theoretical fits are given in Table IV.

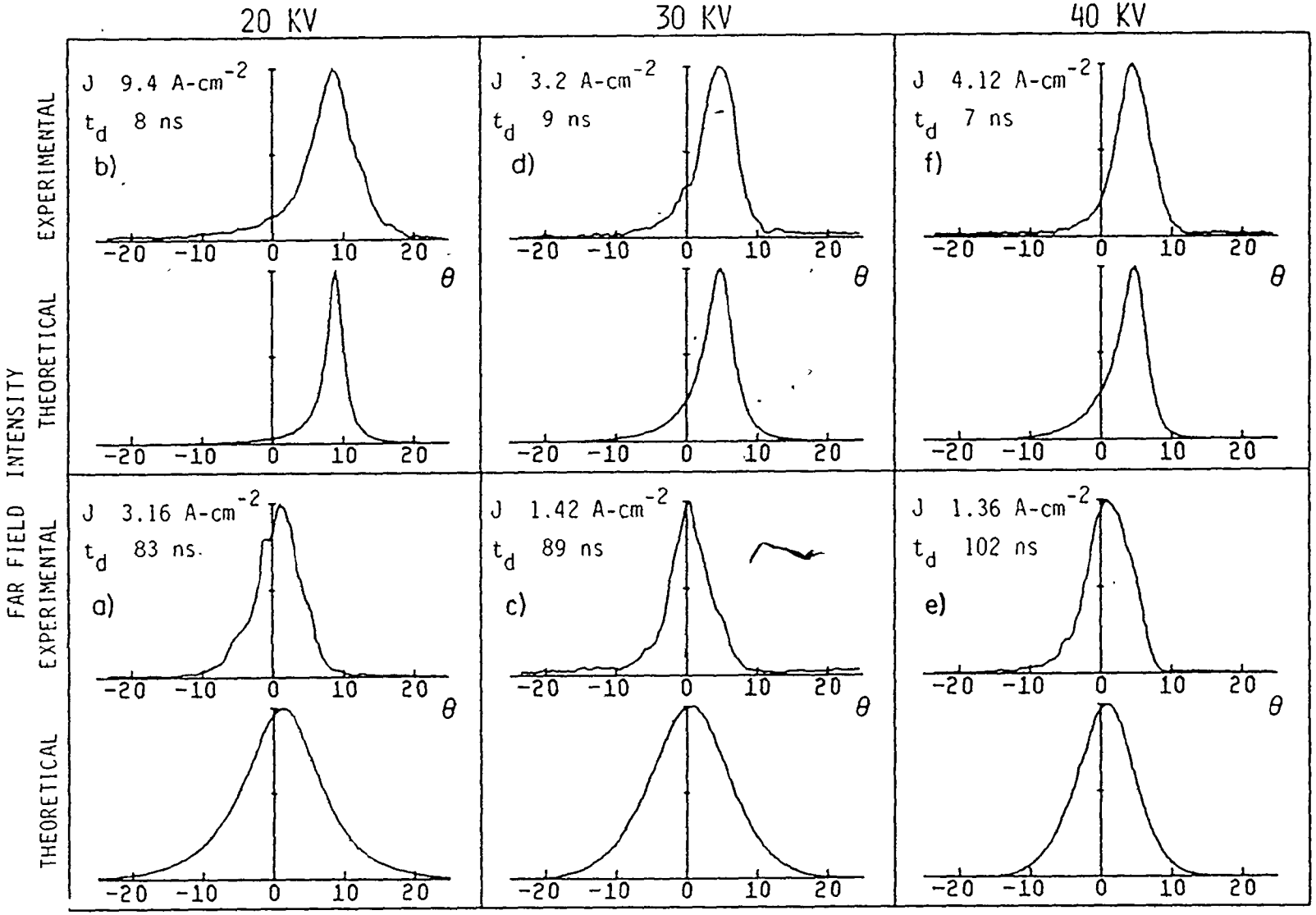
20 KV
30 KV
40 KV
FAR FIELD INTENSITY
EXPERIMENTAL
THEORETICAL
EXPERIMENTAL
THEORETICAL
J 9.4 A-cm^{-2}
t_d 8 ns
b)
J 3.2 A-cm^{-2}
t_d 9 ns
d)
J 4.12 A-cm^{-2}
t_d 7 ns
f)
J 3.16 A-cm^{-2}
t_d 83 ns.
a)
J 1.42 A-cm^{-2}
t_d 89 ns
c)
J 1.36 A-cm^{-2}
t_d 102 ns
e)
-20 -10 0 10 20
θ

corresponds to the width of the carrier concentration profile at half maximum calculated by solving the steady-state carrier transport equation (Appendix B) using Klein's profile [28] for the carrier generation rate. The absorption in the passive region is 150 cm^{-1}. The remaining parameter $\delta\epsilon$ is chosen so that the the peak position corresponds to that observed experimentally. Those values are consistent with the $\delta\epsilon$ calculated in Chapter 3 using the theoretical model which predicts the time delay to lasing threshold on the basis of transient waveguide effects. The far-field patterns measured after a long t_d are seen to be practically aligned along the cavity axis. The associated theoretical far fields have a positive $\delta\epsilon$. At higher pumping currents, all patterns exhibit a deviation which generally decreases with increasing voltage. The experimental conditions are listed in Table IV. Included are the threshold wavelength and the surface temperature at threshold calculated from J_{th}, t_d, E by solving the one-dimensional heat transport equation (Appendix A) using Klein's electron differential energy loss profile [28] to specify the thermal input to the crystal.

Figure 22 shows the far-field patterns emitted by a 16 μm epitaxial layer for two pumping currents at each of three electron beam voltages. Compared to the bulk sample far-field patterns, the most noticeable distinction is the

TABLE IV: Experimental conditions for the time-resolved far-field measurements and parameters used for the theoretical fits. The active region thicknesses were taken as 1.85, 2.7, and 3.7 μm for electron-beam voltages of 20, 30, and 40 kV respectively. A passive loss of 150 cm^{-1} was used for GaAs bulk material and 80 cm^{-1} for all the GaInAs hetero-epitaxial samples.

Fig.	Sample	V (kV)	J ($A-cm^{-2}$)	t_d (nsec)	λ (Å)	ΔT (°K)	L (μm)	δε	Mode (Phase)
21 a	GaAs	20	3.2	83	8429	8.3	∞	.04	E_1
b	"	"	9.4	8	8378	5.7	"	.0	"
c	"	30	1.4	89	8432	5.4	"	.04	"
d	"	"	3.2	9	8394	2.3	"	.005	"
e	"	40	1.36	102	8432	6.6	"	.02	"
f	"	"	4.12	7	8394	2.5	"	.0	"
22 a	GaInAs 107D	20	2.4	21	8602	3.0	16	-.01	$E_7+E_8(1.25\pi)$
b	"	"	6.0	10	8592	4.5	"	-.01	E_7
c	"	30	1.6	55	8598	4.5	"	-.005	E_5
d	"	"	4.0	12	8577	3.8	"	-.01	E_6
e	"	40	.92	53	8594	2.9	"	.0	E_3
f	"	"	1.6	12	8588	1.5	"	.0	$E_3(.6\pi)+E_7+.47E_9(.3\pi)$
23 a	GaInAs 107B	20	2.0	38	8624	3.4	16	-.005	$E_6+E_7(.5\pi)+2.22E_{13}(1.5\pi)$
b	"	"	5.6	12	8576	4.8	"	-.02	$.67E_8(.8\pi)+.45E_{10}(.93\pi)+.534E_{15}+E_{17}(.3\pi)$
c	"	30	1.6	30	8592	3.0	"	.01	$.86E_8(1.93\pi)+.95E_{10}+E_{12}(.3\pi)$

TABLE IV (cont.)

Fig.	Sample	V (kV)	J ($A\text{-}cm^{-2}$)	t_d (nsec)	λ (Å)	ΔT (°K)	L (μm)	δε	Mode (phase)
23 d	GaInAs 107B	30	3.2	12	8588	3.1	16	-.01	$1.35E_{10}(.2\pi)+1.06E_{13}(1.9\pi)+1.24E_{15}(.47\pi)+E_{17}+E_{18}(.25\pi)$
e	"	40	.92	81	8602	3.8	"	.005	$.6E_2+.4E_6(1.33\pi)+.72E_8(1.42\pi)+.72E_{10}(1.66\pi)+E_{12}$
f	"	"	2.0	12	8586	1.9	"	.0	$.75E_7(1.93\pi)+.75E_9(.2\pi)+1.05E_{11}(1.78\pi)+2E_{17}(.5\pi)$
24 a	GaInAs 106C	20	3.68	16	8792	3.8	12	.0	$.45E_4(.4\pi)+E_6+E_7(1.05\pi)+.88E_8(.32\pi)$
b	"	"	5.4	11	8786	4.7	"	.0	$.44E_4(1.937\pi)+.8E_6+E_8(.219\pi)$
c	"	30	1.8	34	8786	3.7	"	.01	$E_8+E_{10}(.5\pi)+.83E_{11}(1.47\pi)$
d	"	"	2.4	12	8788	2.3	"	.0	$.51E_3+E_6(1.882\pi)+.52E_9(.25\pi)$
e	"	40	1.2	37	8786	2.9	"	.01	$.3E_6(.32\pi)+E_8+.95E_{10}(1.62\pi)$
f	"	"	2.44	12	8785	2.3	"	.01	$.9E_8(1.45\pi)+E_{10}+E_{11}(.5\pi)$
25 a	GaInAs 101D	20	2.68	13	8802	2.4	12	.0	$.9E_5(1.75\pi)+E_7+E_8(.5\pi)+1.4E_{10}(.8\pi)$
b	"	"	5.72	13	8806	5.2	"	.0	$.43E_4(1.75\pi)+E_6+.35E_8(1.688\pi)$
c	"	30	1.52	12	8801	1.5	"	.0	$E_9+E_{10}(.5\pi)$
d	"	"	4.8	10	8800	4.0	"	-.002	$.9E_3+E_4(1.54\pi)+.36E_6(.12\pi)+.6E_8(1.6\pi)$
e	"	40	.88	12	8800	.83	"	.0	$E_8+E_9(.5\pi)$
f	"	"	1.76	200	8844	12.	"	.018	$E_1+.4E_4(1.5\pi)+.2E_5(1.7\pi)+.15E_6(1.5\pi)$
26 a	GaInAs 103D	20	1.64	11	8782	1.3	3.5	.0	$E_1+E_2(1.25\pi)$
b	"	30	1.08	12	8796	1.0	"	.0	$E_1+.6E_2(1.25\pi)$
c	"	40	.8	6	8790	.4	"	.0	$E_1+E_2(1.25\pi)$

Fig. 22: Experimental and theoretical far-field patterns at lasing threshold from a 16 μm GaInAs heteroepitaxial layer (sample 107D) for a high and a low pumping intensity at each of three accelerating voltages. The parameters for the theoretical fits are given in Table IV.

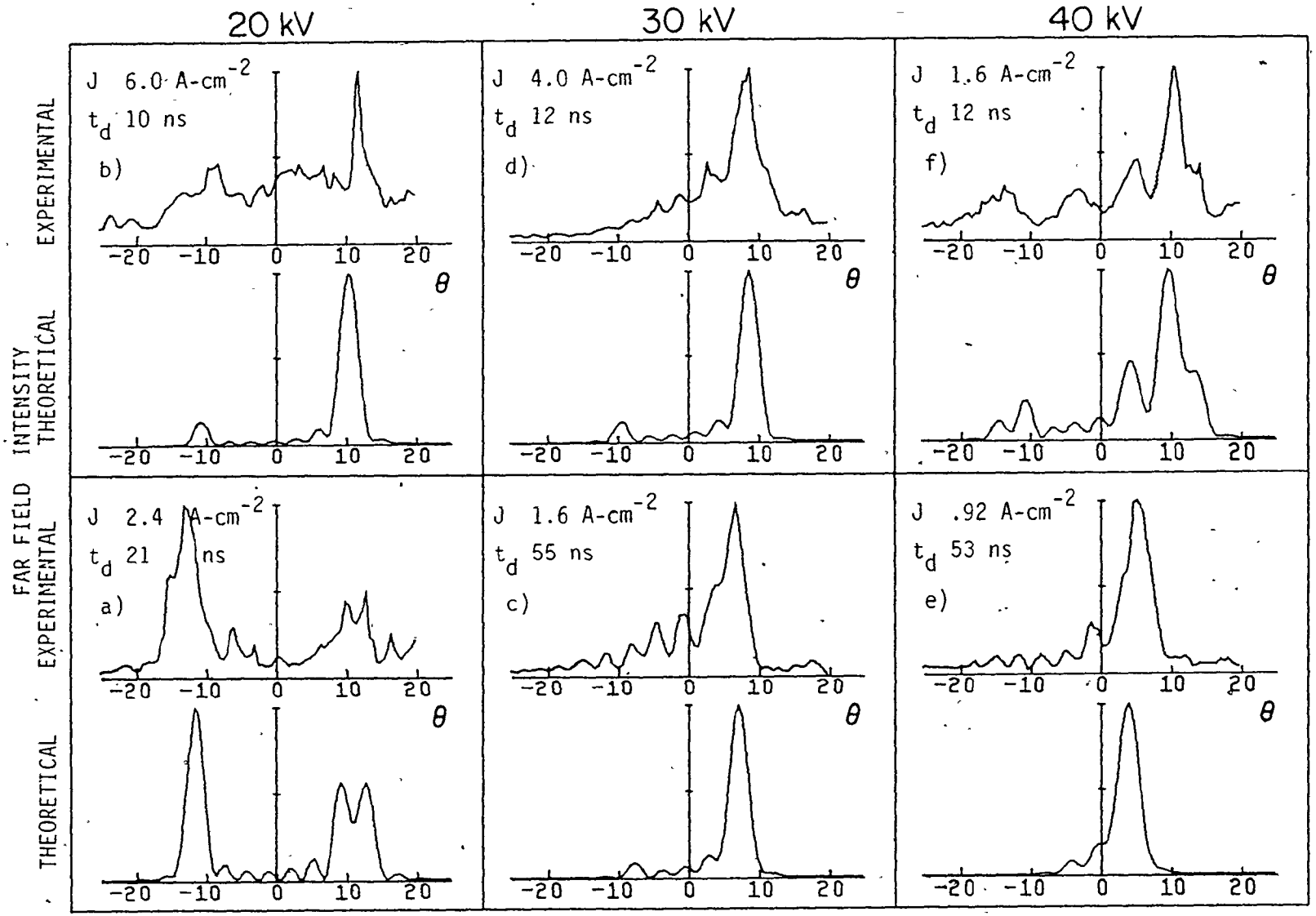
20 kV
30 kV
40 kV
FAR FIELD INTENSITY
EXPERIMENTAL
THEORETICAL
EXPERIMENTAL
THEORETICAL
J 6.0 A-cm^{-2}
t_d 10 ns
b)
J 4.0 A-cm^{-2}
t_d 12 ns
d)
J 1.6 A-cm^{-2}
t_d 12 ns
f)
J 2.4 A-cm^{-2}
t_d 21 ns
a)
J 1.6 A-cm^{-2}
t_d 55 ns
c)
J .92 A-cm^{-2}
t_d 53 ns
e)
-20 -10 0 10 20
θ

appearance of many smaller peaks beside the major emission peak. The regularly spaced ripples are particularly evident at 30 kV (Fig. 22c,d) and at 40 kV, low current (e). The 3.5^{o} interval between peaks is roughly the separation that could be expected from diffraction theory for a source 16 μm wide.

The theoretical lowest loss modes for the appropriate $\delta\epsilon$ lead to far fields which exhibit features similar to four of the far-field patterns (Fig. 22b,c,d,e) although the tail of the experimental far fields extends further into the e-beam quadrant and the ripples are more prominent. The values of $\delta\epsilon$ were chosen to fit the position of the major peak but $\delta\epsilon$ deviates only slightly from zero, taking small negative values for higher currents. The smaller values with larger current are expected because the dispersion due to the gain gives a negative contribution to the refractive index change.

A very surprising feature is noticed at 20 kV, low pumping current (Fig. 22a). The largest peak occurs in the electron beam quadrant. This is unexpected since the single mode emission generally deviates toward the quadrant which corresponds, in the near field, to the absorbing passive region. But it is not necessary to call upon any special redistribution of the optical parameters within the cavity. A far field with the very same features is obtained from our

model if two modes E_7 and E_8 are superposed, out-of-phase by $5\pi/4$. The implications of such a superposition will be commented upon in the discussion following this section. Suffice it to say for the moment that, in finite cavities, multimode lasing is not unexpected because many modes can share approximately the same diffraction loss. To simplify the notation, instead of using the values of u and k to designate a given mode, we will use the number of maxima "i" in the near field (or, in other words, the mode order) and identify it by E_i. In the far field, this usually corresponds to the number of ripples plus two. For some low-order modes and large $\delta\varepsilon$, the exact number of maxima is not always apparent but the ambiguity can be resolved if we define the mode order as the integer closest to $(u + \eta v)/\pi$ (see (4.15) and (4.17)).

At high voltage and current (Fig. 22f), we note the presence of three smaller peaks aside from the major peak. It is difficult to explain why, in this particular case, the angular separation is larger than the model would predict. Mode superposition allows us to fit the emission pattern in the positive quadrant but not in the negative quadrant. Note also that time delays of up to 55 nsec were observed indicating that the temporal behaviour retains some characteristics of the bulk material.

The far-field patterns produced by another 16 μm

sample are shown in Fig. 23. Although we observe again small, regularly-spaced features every 3.5° which are easily associated with a 16 μm source, the overall far fields differ from the previous sample. In particular, the emission appears at larger deviation corresponding to higher order modes. Note that the emission at low pumping current is closer to the cavity axis than at high current. Again it proved possible to calculate theoretical far field patterns in agreement with experiment by superposing a few low loss modes.

For a 12 μm epi-layer, the ripple separation has increased to approximately 4.5° (Fig. 24). Both far fields at 20 kV (Fig. 24a,b) and the one at 30 kV, high current (Fig. 24d) are typical of single lasing modes although the theoretical fits are somewhat improved by superposing more than one mode. The other three far fields (Fig. 24c,e,f) are characterized by their emission at large deviation. Notice also the relatively small secondary peak in the e-beam quadrant. Such a feature occurs as a result of the superposition of two neighbouring modes out-of-phase by $\pi/2$. At 40 kV and low current (Fig 24e), no simple summation of modes leads to a far field combining a forked major peak and a small secondary peak. The phase condition for a small secondary peak was described above. However, a forked major peak results from the combination of two odd or two even

Fig. 23: Experimental and theoretical far-field patterns at lasing threshold from a 16 μm GaInAs heteroepitaxial layer (sample 107B) for a high and a low pumping intensity at each of three accelerating voltages. The parameters for the theoretical fits are given in Table IV.

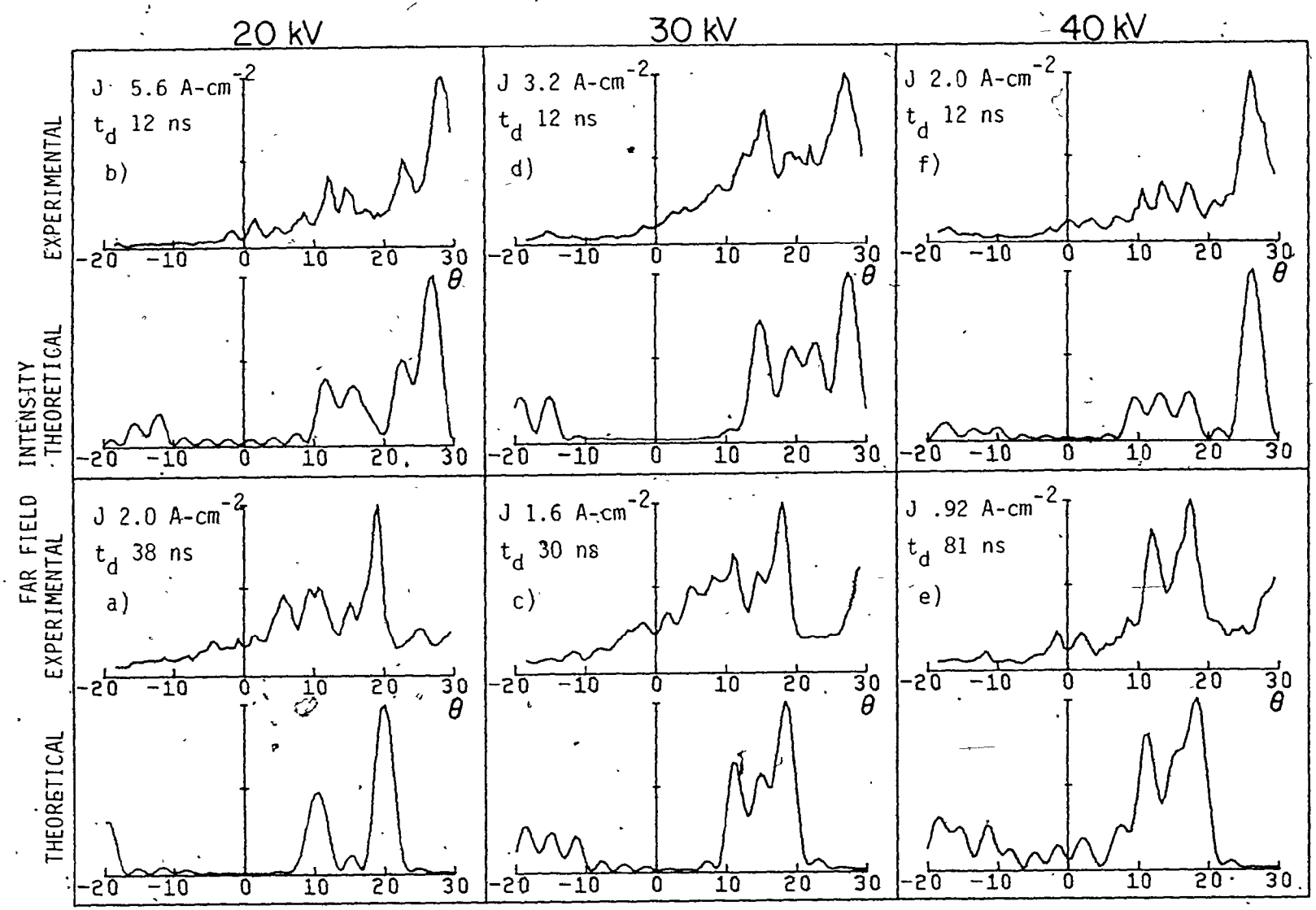
20 kV
30 kV
40 kV
FAR FIELD INTENSITY
EXPERIMENTAL
THEORETICAL
EXPERIMENTAL
THEORETICAL
J 5.6 A-cm^{-2}
t_d 12 ns
b)
J 3.2 A-cm^{-2}
t_d 12 ns
d)
J 2.0 A-cm^{-2}
t_d 12 ns
f)
J 2.0 A-cm^{-2}
t_d 38 ns
a)
J 1.6 A-cm^{-2}
t_d 30 ns
c)
J .92 A-cm^{-2}
t_d 81 ns
e)
θ
-20 -10 0 10 20 30

Fig. 24: Experimental and theoretical far-field patterns at lasing threshold from a 12 μm GaInAs hetero-epitaxial layer (sample 106C) for a high and a low pumping intensity at each of three accelerating voltages. The parameters for the theoretical fits are given in Table IV.

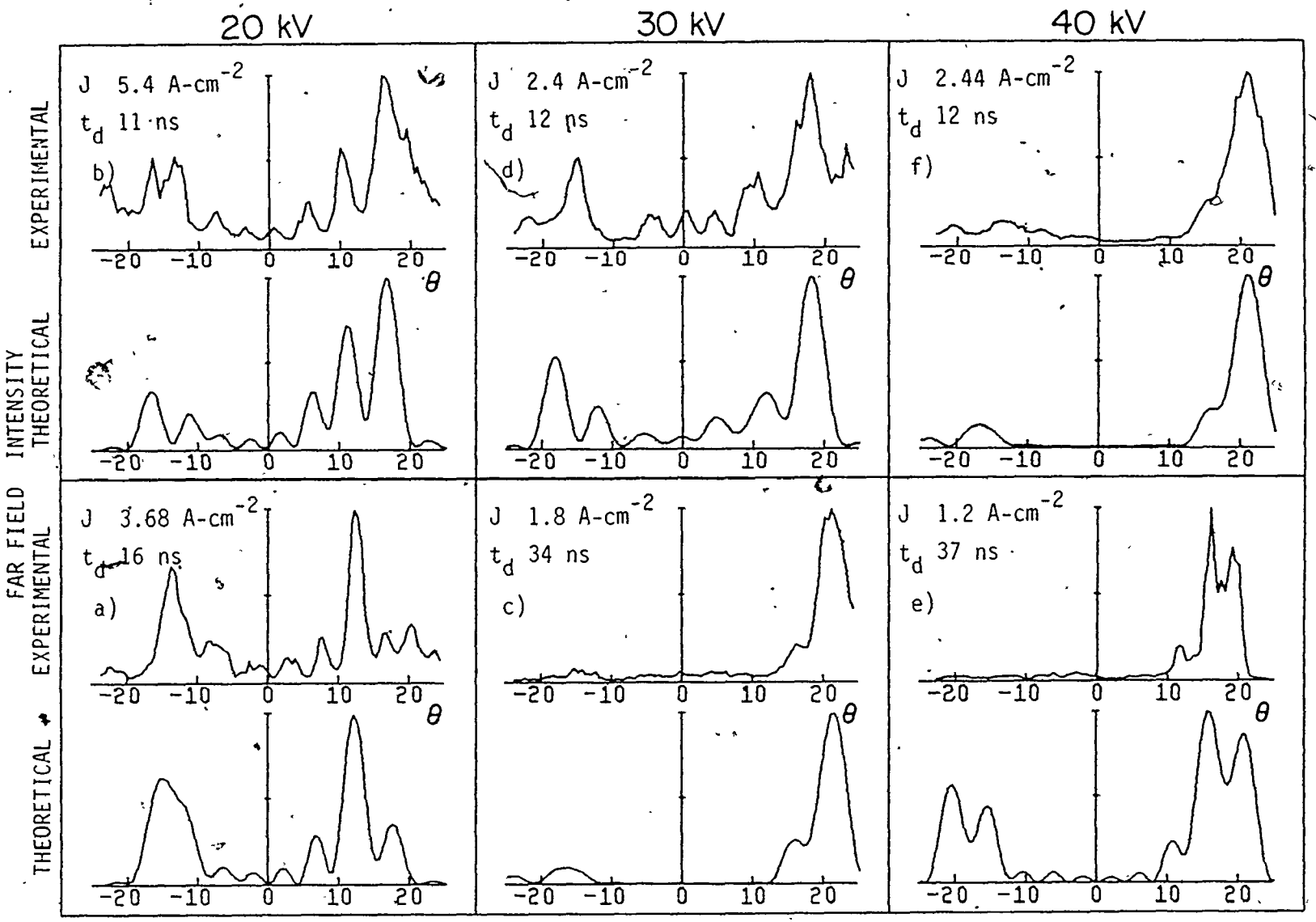
20 kV
30 kV
40 kV
FAR FIELD INTENSITY
EXPERIMENTAL
THEORETICAL
EXPERIMENTAL
THEORETICAL
J 5.4 A-cm^{-2}
t_d 11 ns
b)
J 2.4 A-cm^{-2}
t_d 12 ns
d)
J 2.44 A-cm^{-2}
t_d 12 ns
f)
J 3.68 A-cm^{-2}
t_d 16 ns
a)
J 1.8 A-cm^{-2}
t_d 34 ns
c)
J 1.2 A-cm^{-2}
t_d 37 ns
e)
θ
-20 -10 0 10 20

neighbouring modes out-of-phase by approximately $\pi/2$. Here we show a mode combination which produces a forked major peak, but as a result, the emission in the e-beam quadrant exceeds the intensity observed experimentally.

Sample 101D exhibited little variation of the time delay to lasing threshold, t_d always fell in the range of 10 to 13 nsec. The far-field patterns are shown in Fig. 25. The peaks appear to move in as the current increases because t_d is approximately constant. Hence the temperature at threshold is itself increasing thereby improving confinement. At 20 and 30 kV, the experimental far fields are better fitted by modes other than the calculated lowest loss modes. The ripples are not quite as evident as for sample 106C but it is possible to distinguish the characteristic 4.5^o to 5^o separation for a 12 μm layer. At an electron beam energy of 40 keV, the major peak is at a surprisingly large angle corresponding to modes which again are not the calculated lowest-loss modes. If we compare to the results at other voltages, it appears that at low current, the far field is constrained into large deflection angles. In fact, even at twice the pumping current, the far field at threshold at 40 kV had not changed. For that reason, an example of a mode taken long after threshold is plotted to show how the radiation is eventually confined on axis when the temperature of the active region rises

Fig. 25: Experimental and theoretical far-field patterns at lasing threshold from a 12 μm GaInAs heteroepitaxial layer (sample 101D) for a high and a low pumping intensity at each of three accelerating voltages. The parameters for the theoretical fits are given in Table IV.

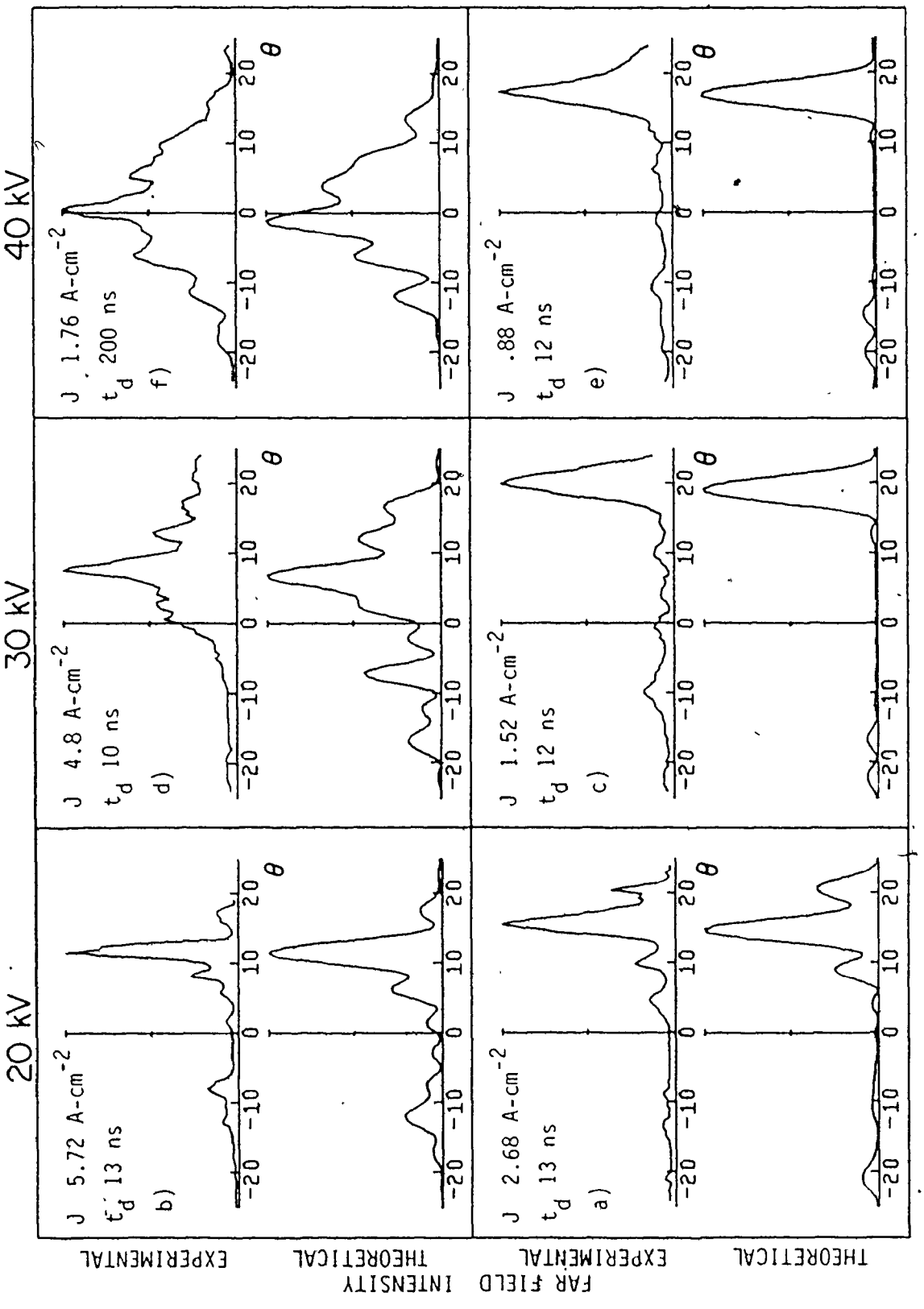
20 kV
30 kV
40 kV
J 5.72 A-cm^{-2}
t_d 13 ns
b)
J 4.8 A-cm^{-2}
t_d 10 ns
d)
J 1.76 A-cm^{-2}
t_d 200 ns
f)
J 2.68 A-cm^{-2}
t_d 13 ns
a)
J 1.52 A-cm^{-2}
t_d 12 ns
c)
J .88 A-cm^{-2}
t_d 12 ns
e)
θ
-20 -10 0 10 20
EXPERIMENTAL
THEORETICAL
FAR FIELD INTENSITY
EXPERIMENTAL
THEORETICAL

sufficiently. However the confinement doesn't preclude the observation of a fine structure superimposed on the wide peak. This again appears to be the result of multimode lasing particularly under these conditions of high pumping and long time delay.

The far-field patterns of a thin hetero-epitaxial layer are characterized by a wide peak with little fine structure. Patterns for pumping currents just above threshold are shown in Fig. 26 for a 3.5 μm thick layer. Such emission is expected from a uniformly pumped narrow source. Moreover, because the radiation is confined from the start, there are no transient waveguide effects and the time delays to threshold are of short duration. Since there is little variation with time and current, only one far field for each voltage is shown. The peaks deviate by up to 8^{o} into the e-beam quadrant. Superposition of two lasing modes, out-of-phase by $5\pi/4$, produces the asymmetric shape of the output and the deviation into the e-beam quadrant.

Although not in the mainstream of the data presented, it is of interest to mention the observation of intriguing far-field patterns on another sample. Figure 27a shows the far-field distribution of a 16 μm epi-layer pumped by 20 keV electrons at relatively low current density. The diffraction pattern exhibits large oscillatory features but most of the emitted energy is concentrated close to the

Fig. 26: Experimental and theoretical far-field patterns at lasing threshold from a 3.5 μm GaInAs hetero-epitaxial layer (sample 103D) at each of three accelerating voltages. The parameters for the theoretical fits are given in Table IV.

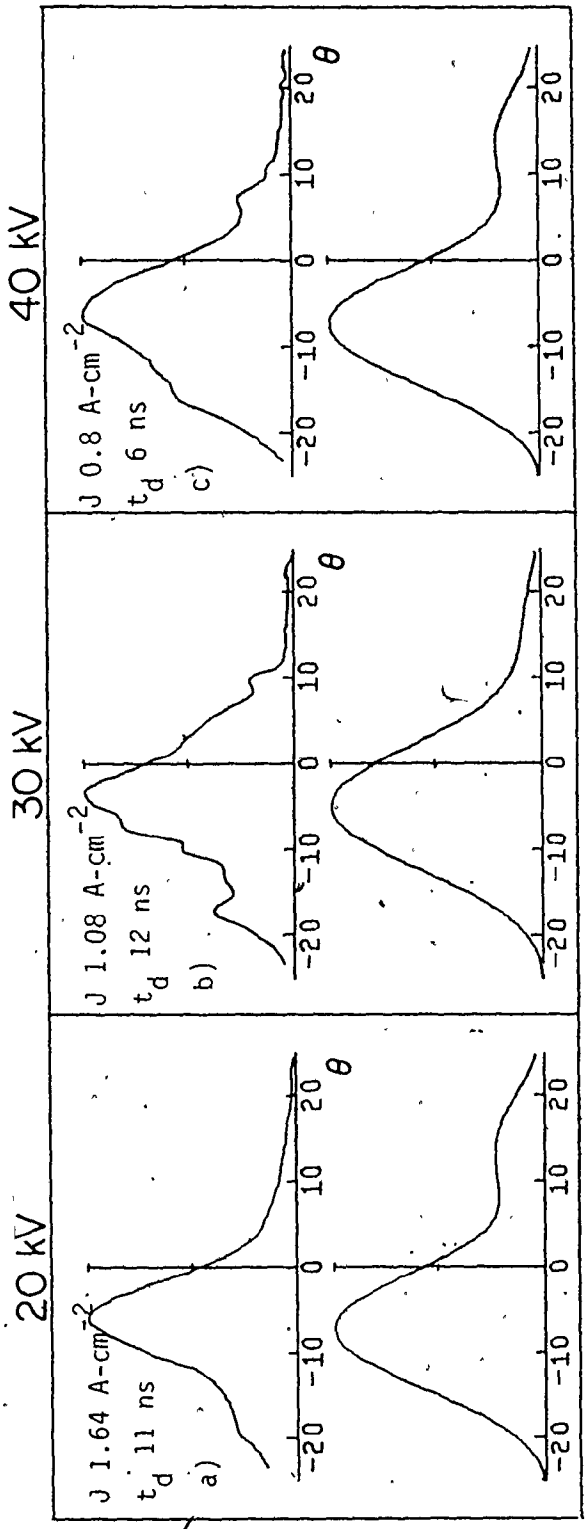
20 kV
30 kV
40 kV
J 1.64 A-cm^{-2}
t_d 11 ns
a)
J 1.08 A-cm^{-2}
t_d 12 ns
b)
J 0.8 A-cm^{-2}
t_d 6 ns
c)
θ
-20 -10 0 10 20
FAR FIELD INTENSITY
THEORETICAL EXPERIMENTAL

Fig. 27: a) Experimental far-field pattern emitted from a 16 μm GaInAs hetero-epitaxial layer pumped using a 20 kV electron beam.

b) Theoretical fit generated by the superposition of two modes, one calculated for a 16 μm layer, the other for a 13.7 μm layer (α_p = 80 cm^{-1}, $\delta\varepsilon$ = 0.0, d = 1.5 μm).

c) Magnified picture of the sample showing the partially masked emitting facet.

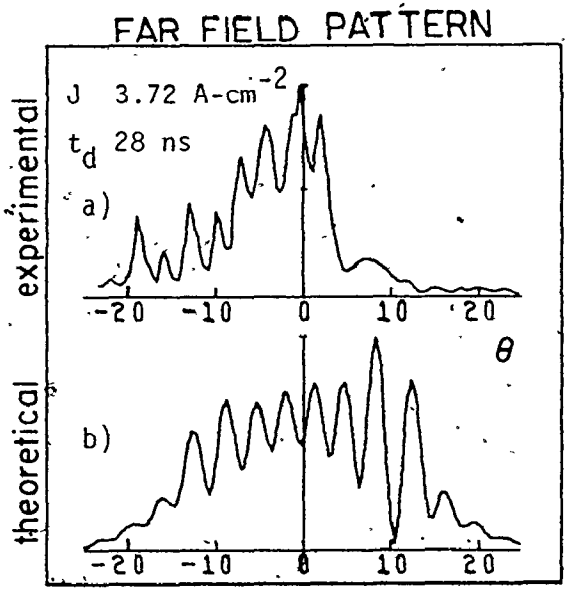
FAR FIELD PATTERN
J 3.72 A-cm^{-2}
t_d 28 ns
a)
experimental
-20 -10 0 10 20
θ
b)
theoretical
-20 -10 0 10 20

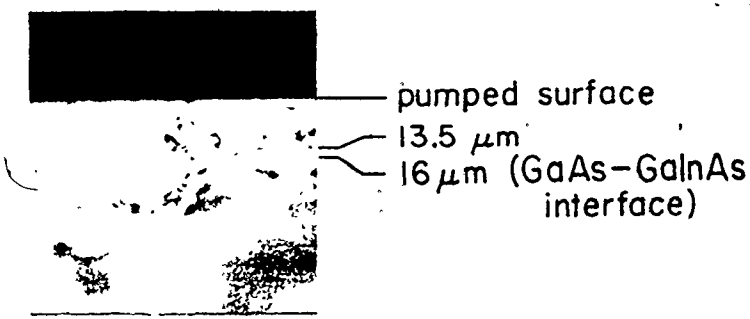
pumped surface
13.5 μm
16 μm (GaAs–GaInAs interface)
EMITTING FACET
(photomicrograph)

c)

cavity axis. The closely-spaced peaks are evidence of higher order lasing modes. But, according to the calculations of Chapter 4, most of the light of higher order modes should appear in two widely separated peaks. Attempts at reproducing theoretically the observations by superposing the modes of a 16 μm cavity were unsuccessful. However, the superposition of two modes, one from a 16 μm cavity and the other from a 13.7 μm cavity resulted in the calculated pattern shown in Fig. 27b. This procedure appears, at first, difficult to justify from a physical point of view. The explanation is to be found in Fig. 27c which shows a magnified picture of the laser emitting facet. The solder used to mount the sample has spread to cover part of the emitting region, in one place leaving the 16 μm epi-layer unmasked to a depth of only ≈13.5 μm. Lasing emission from a region of the epi-layer partially masked by the solder was superposed on the light originating from an unobstructed region. This is exactly what the far-field pattern suggested. The indications were that two separate structures limited the spread of the radiation along the x-axis to depths of 16 and 13.7 μm. Had no obstruction been visible, this could have been interpreted as evidence for the presence of a sudden change in the epi-layer thickness. This serves to show how the far-field pattern can be used to gain some information about the radiation distribution in

the near field.

5.3 Discussion

Most measurements were made early after the appearance of a lasing mode to avoid saturation and to reduce the number of transverse and longitudinal modes lasing simultaneously. However, the threshold region is particularly difficult to study because the emission intensity is inherently low and has a superlinear dependence on pumping current. Hence we must contend with some instability and relatively low signal-to-noise ratio.

Despite those difficulties, it is possible to clearly see the angular variations of the emission from the bulk sample with pumping current and time delay. The theoretical model shows that the angular position of the peak is most affected by the refractive index difference between active and passive region for a given pumping depth. The deviation decreases with increasing refractive index. It is relatively independent of the absorption. α_s affects mostly the width of the far field by reducing the spread of the radiation in the unpumped region.

Two mechanisms capable of producing refractive index changes of sufficient magnitude to affect the transverse mode have been identified [15]: the temperature gradient between active and passive region produces a change in $\delta\epsilon$

which is increasing with time and the gain variation from the pumped to unpumped region results in a refractive index difference through Kramers-Kronig relation.

Effectively, mode confinement (as evidenced by the alignment of the radiation along the cavity axis) is associated with higher threshold temperatures. Since the band gap decreases with temperature it is not surprising to see that a longer threshold wavelength corresponds to a longer time delay to onset of lasing although the band gap energy is not the only parameter to determine the lasing wavelength.

To summarize, in bulk materials, confined transverse modes are associated with long time delays to onset of lasing and low pumping currents while the far fields related to short time delay, high pumping conditions exhibit large angular deviations. This serves as a confirmation of the model for the time delay to threshold as a function of pumping presented in Chapter 2. In this model, the long t_d's observed have been associated not with the time needed for the radiation or the gain to build up but with the time required for the refractive index difference to increase sufficiently to bring about a significant decrease in diffraction losses.

Despite the efforts to make the measurements as soon as possible after threshold, it is apparent from the

complexity of some mode structures that multimode lasing occurs in hetero-epitaxial layers. Most convincing is the evidence provided by two types of relatively simple far-field patterns. Sample 107D (Fig. 22a), with its largest peak in the e-beam quadrant is unlike any of the single mode patterns calculated. But the simple superposition of the two neighbouring modes E_7 and E_8, with a phase offset of $5\pi/4$, reproduces well such a far-field pattern. In a number of other cases, far fields were observed experimentally which exhibited a strong emission at large angular deviation but only a very small secondary peak in the e-beam quadrant (e.g. 106C, Fig. 24c). Again, such a far field is easily produced by the juxtaposition of modes E_{10} and E_{11}, out-of-phase by $\pi/2$. In both cases, the phase of each mode varies with angle in such a way that, for a particular phase offset, the fields will cancel in one quadrant and add in the other quadrant.

On physical grounds, it is easily conceivable that a second lasing mode will exploit the gain left unused by the first mode in the vicinity of the longitudinal nodes. Hence a phase difference of $\pm\pi/2$ or $\pm 3\pi/2$ between the two modes is expected. Moreover, multimode operation will be possible provided that the gain required to excite each mode is approximately the same. Returning to our experimental examples, we note that for sample 107D (Fig. 22a), the

diffraction loss for modes E_7 and E_8 differ by only 10% while for sample 106C (Fig. 24c), the difference is 18%. Moreover, in the latter case, the phase difference is $\pi/2$. That the phase difference is not exactly $3\pi/2$ in the former example may be a reflection of the fact that each mode will have a slightly different propagation constant, hence the phase relationship may change along the axis of the crystal. With a phase difference of $5\pi/4$, the gain may be exploited more effectively.

In any case, that the superposition of two modes provides a good fit for such unexpected far field patterns appears as very convincing evidence for multimode lasing and a good justification for mode superposition in other cases where a single mode appears insufficient to explain the more complex features observed experimentally.

Note also that the gain required to excite some of the higher order transverse modes can be only slightly larger than the gain required for the lowest loss mode particularly if α_s and $\delta\varepsilon$ are small. This explains why it is not unusual to encounter far fields which are best fitted by modes other than the lowest loss mode. Moreover, the fact that the actual permittivity profile differs somewhat from the step profile and the presence of defects or inhomogeneities in the medium may favor such higher order modes.

The 12 μm thick epi-layers exhibit even less transient waveguide effect. This is reflected in the fact that there is little variations in the far-field pattern, threshold temperature, and threshold wavelength. There are a number of cases where an increase in pumping current doesn't result in lower threshold temperature. Still, there are two examples of relativity long delays to threshold. The secondary peak is more prominent in 106C (Fig. 24a,b,d) than 101D indicating that the absorption is lower so that the radiation is more evenly distributed within the epi-layer. We still observe large deviations of the major peak at 40 kV corresponding to modes which theoretically are third or fourth lowest in diffraction loss.

The thin epi-layer, 3.5 μm, always reaches threshold after a short time delay. The far fields are typical of a narrow confined layer. At threshold, little variation occurs within the range of pumping currents considered. Moreover, the threshold pumping currents are small indicating low diffraction losses. The deviation of the lasing output is well acounted for by the superposition of 2 modes.

CHAPTER 6

CONCLUSIONS

In this thesis, results of an experimental and theoretical study of optical waveguiding in electron-beam-pumped semiconductor lasers were reported. The laser threshold behaviour was shown to change significantly according to whether transient or permanent waveguiding dominates. Of particular interest were the waveguide effects on the time delay to onset of lasing and on the angular distribution of the emitted radiation at lasing threshold.

In a first part, a theoretical model for the transient waveguide effects was shown to account for a major aspect of the semiconductor laser behaviour in bulk GaAs, the long time delays to lasing threshold from the start of the pulsed excitation. According to this model, the delay to onset of lasing is determined, not by the time necessary for the gain to build up, but by the time needed for the diffraction losses to decrease to the level of the available gain. The magnitude of these losses is dependent on the temporal variation of the optical confinement which had been identified previously as being responsible also for the time-dependent angular variations of the far-field laser

radiation pattern [15]. The controlling factor is the difference in refractive index between the pumped and the unpumped regions of the laser cavity. Two effects contribute to this difference. Initially, the presence of gain in the region of the lasing wavelength causes the refractive index in the active layer to be reduced relative to that in the passive region. As time evolves, the rise in the temperature due to the incident electron beam produces a growing positive refractive index difference between the active and passive regions which opposes the negative contribution due to gain. This process eventually brings about optical confinement and in turn lasing long after a stable gain has been established, subject, of course, to the condition that the gain can overcome the residual losses.

Aside from the good theoretical fits to the experimental data for bulk GaAs afforded by the model, two other pieces of experimental evidence serve to confirm the importance of the waveguiding effects on the time-delay-to-threshold behaviour. On the basis of the model presented, a semiconductor sample which incorporates a permanent refractive index step close to the active region, sufficient to provide permanent optical confinement, would be expected to exhibit only short time delays. Effectively, the experimental observations on 0.7 μm and 3.5 μm GaInAs hetero-epitaxial layers show that lasing always occurs

within a few nanoseconds of the beginning of the pumping pulse or not at all.

Perhaps even more convincing are the measurements of the far-field radiation pattern at lasing threshold. Under low current excitation, the model predicts that a large decrease in diffraction effects will be required for the temperature and the associated refractive index change to rise sufficiently to provide the necessary optical confinement. The experimentally measured far-field patterns effectively show that long time delays are associated with an angular distribution of the emitted radiation centered practically on the laser cavity axis, indicating that the radiation in the crystal is now confined within the active layer. Conversely, under large pumping current, the time delays are short and they are associated with far-field patterns deviating at larger angle because, with the larger gain, a smaller reduction in the diffraction effects is required before lasing can occur. Those results, combined with the previously mentioned absence of long time delays in thin hetero-epitaxial layers concur to provide very strong evidence that transient waveguiding effectively controls the long time delays to lasing threshold in bulk GaAs.

This mechanism is probably not specific to electron-beam-pumped semiconductor lasers. It may apply to optically excited semiconductor lasers as well since the same pumping

geometry is used. In junction lasers, various delay mechanisms have been proposed, predicated on the existence of features such as saturable trapping centers [18], unusual distribution of the density of states close to the band edge [21] or anomalous thermalization of hot carriers [21]. In contrast, the model presented here calls only upon physical processes known to occur when a semiconductor is excited by an electron beam such as shallow penetration of the electrons, heating and concomitant spatial variations in the dielectric permittivity. It is only recently that a similar model has been applied to junction lasers [39] indicating that transient waveguide effects can also account for the long delays observed in those devices.

The time delay measurements on the GaInAs samples suggested the existence of permanent optical confinement. In the second part of this thesis, we studied theoretically and experimentally the relative importance of transient and permanent waveguide effects in such hetero-epitaxial structures. There is a refractive index step at the interface between the epi-layer and the substrate due to the change in material composition which results in optical confinement of the laser radiation within the GaInAs layer. A theoretical model using a step profile to approximate the spatial variation of the permittivity from the active to the passive region within the epitaxial layer was introduced to

investigate the dependence of the diffraction loss and the spatial distribution of the radiation on the cavity parameters. The presence of the confining surface is seen to change dramatically the dynamic properties of the cavity when positioned close to the active region. Permanent waveguiding then totally dominates the transient waveguide effects. This was reflected experimentally by the measurements on a 3.5 μm epitaxial layer which showed no long time delay to threshold nor time dependence of the far-field output.

The effects of the confining surface decrease as it is made less visible to the laser radiation. The critical factors are the thickness of the passive region, the optical losses in that same region and the refractive index step between active and passive regions. As these factors increase, the transient waveguide effects take gradually more and more importance. The analysis permits us to determine the specific conditions under which the effects of the reflecting interface become negligible. Although both the threshold gain and the far-field distribution are affected by the reflecting surface, the far field is a more suitable parameter to determine the importance of the resulting confinement because features of the angular distribution characteristic of a finite cavity persist even when the dependence of the gain on the dynamic refractive

index step has become indistinguishable experimentally from that of the bulk material. The far-field patterns were measured on hetero-epitaxial layers ranging in thickness from 3.5 to 16 μm. Features attributed to a finite cavity such as a secondary peak in the electron-beam quadrant and regularly spaced minor peaks can be recognized in many instances. However, the far fields are not generally as simple as theory would predict for the lowest-loss mode. This is quite understandable in view of the theory presented since a number of modes can share approximately the same configurational loss. Which mode or modes lase may then depend to some extent on crystalline imperfections or departure of the permittivity from the assumed step profile.

The assumption of multimode lasing is also justified by the good theoretical fits to some experimental far-field patterns which otherwise would have been quite unexpected. For instance, the theory shows that the maximum of the radiation far-field distribution for a single mode never deviates toward the electron beam. However, such deviations were observed experimentally and are well accounted for by the superposition of two modes with a phase relationship which is approximately as expected on the basis of spatial hole-burning. Note that such multimode lasing behaviour is in contrast with that of the bulk cavity where the first order mode generally exhibits a diffraction loss much lower

than any higher order modes.

The finite cavity model was derived with electron-beam-pumped hetero-epitaxial lasers in mind but there is no reason why it would not be applicable also to platelet lasers, for instance. Moreover, since the same geometry is used for optical pumping of semiconductors, the theoretical analysis presented would most likely retain its validity in that case. With some slight modification the model may be useful in the study of other transversally excited thin laser cavities such as some dye lasers.

The electron-beam-pumping of thin hetero-epitaxial layers offers the opportunity for a range of interesting experiments. Because the GaAs substrate is practically transparent at the wavelength which corresponds to the band gap energy of the GaInAs layer, it may be possible to measure directly the wavelength and time dependence of the gain in the active layer under various excitation conditions by measuring the transmission of a monochromatic beam of light incident normal to the pumped surface. This would be useful in providing a confirmation of the theoretical expression for the gain used to estimate the time delays to lasing threshold.

Also, the theory proposed for the faster-than-band-gap wavelength tuning of the emitted radiation in bulk samples [42] could now be tested on GaInAs hetero-epitaxial

lasers. This model is based on the strong wavelength dependence of the transient waveguide effects but, in the presence of permanent optical confinement, this factor would be eliminated and the laser output wavelength should now be directly related to the energy of the gain maximum.

APPENDIX A

TIME DEPENDENT TEMPERATURE PROFILE

A semi-infinite solid ($0 \leq x \leq \infty$) is initially at a uniform temperature. Starting at time $t = 0$, heat is generated within the solid at a rate $g(x',t')$ while the boundary surface at $x = 0$ is kept insulated. We wish to determine the spatial variations of the temperature as a function of time.

The solution of the problem is given by [29]

$$\Delta T(x,t) = \int_0^\infty \int_0^t \frac{\alpha}{k} \frac{g(x',t')}{[4\pi\alpha(t-t')]^{1/2}} \left[\exp\left(-\frac{(x-x')^2}{4\alpha(t-t')}\right) + \exp\left(-\frac{(x+x')^2}{4\alpha(t-t')}\right)\right] dx'dt' ,$$

where g is the heat generation rate, $\alpha = k/C$, k is the thermal conductivity and C is the specific heat.

Assume that for $t > 0$, the heat generation rate is time-independent (i.e. $g(x',t') = g(x')$). Making use of integrals given in [43], an integration over time first gives

$$\Delta T(x,t) = \frac{1}{2k} \int_0^\infty g(x') \left\{ \frac{b}{\sqrt{\pi}} \left[\exp\left(-\left(\frac{x - x'}{b}\right)^2\right) + \exp\left(-\left(\frac{x + x'}{b}\right)^2\right) \right] \right.$$

$$\left. - \left[|x - x'| \operatorname{erfc}\left(\frac{|x - x'|}{b}\right) + (x + x') \operatorname{erfc}\left(\frac{x + x'}{b}\right) \right] \right\} dx' \qquad \text{(A.1)}$$

where $b = (4\alpha t)^{1/2}$

Before the next integration we must specify the form of the heat generation rate. An expression for the electron differential energy loss in a solid is given by Klein [28]:

$$g(x) = J \frac{E}{R_B} \frac{\mu R_B}{4} (1 + \mu|a - x|) \exp(-\mu|a - x|) \ \text{Wcm}^{-3}, \qquad \text{(A.2)}$$

where J is the electron beam current density in Acm^{-2} and E is the beam energy in eV. The Bethe range, R_B, is given by $1.4025 \times 10^{-10} \ E(\text{eV})^{1.65} \ [\rho(\text{gm cm}^{-3})]^{-1}$ and the macroscopic electron absorption coefficeint "μ" is determined using the empirical observation that μR_B is a constant equal to 11 [28]. Finally, the depth of complete diffusion a is defined by $a = 4R_B(Z + 4)^{-1}$ where Z is the target atomic number.

Substitute the above expression (A.2) for g(x) into (A.1) and integrate over x' with the help of integrals in [43]. This leads directly to the following time-dependent temperature profile.

$$\Delta T(x,t) = J \frac{E}{R_B} \frac{\mu R_B}{4} \frac{1}{k} \left(\frac{b}{\mu\sqrt{\pi}} \{ 3[\exp(-(\frac{a+x}{b})^2) + \exp(-(\frac{a-x}{b})^2)] \right.$$

$$- (3 + \mu a)\exp(-\mu a - \frac{x^2}{b^2}) \} - \frac{1}{\mu^2} \{ 2\mu(a+x)\operatorname{erfc}(\frac{a+x}{b})$$

$$+ 2\mu|a-x|\operatorname{erfc}(\frac{|a-x|}{b}) - \mu x(2 + \mu a)\operatorname{erfc}(\frac{x}{b})\, e^{-\mu a}$$

$$+ (3 + \mu|a-x|)e^{-\mu|a-x|} \} + \frac{1}{2} e^{\mu^2 b^2/4} \{ [\frac{3 + \mu(a+x)}{\mu^2}$$

$$- \frac{b^2}{2}] [\operatorname{erf}(\frac{a+x}{b} - \frac{\mu b}{2}) - \operatorname{erf}(\frac{x}{b} - \frac{\mu b}{2})]\, e^{-\mu(a+x)}$$

$$+ [\frac{3 - \mu(a+x)}{\mu^2} - \frac{b^2}{2}] \operatorname{erfc}(\frac{a+x}{b} + \frac{\mu b}{2})\, e^{\mu(a+x)}$$

$$+ [\frac{3 + \mu(a-x)}{\mu^2} - \frac{b^2}{2}] [\operatorname{erf}(\frac{a-x}{b} - \frac{\mu b}{2}) + \operatorname{erf}(\frac{x}{b} + \frac{\mu b}{2})]\, e^{-\mu(a-x)}$$

$$\left. + \frac{3 - \mu(a-x)}{\mu^2} - \frac{b^2}{2}] \operatorname{erfc}(\frac{a-x}{b} + \frac{\mu b}{2})\, e^{\mu(a-x)} \} \right) \qquad (A.3)$$

Temperature profiles at 20 nsec interval are shown in Fig. 28. Since $\delta n/\delta T$ is approximately constant for GaAs over the range of refractive index which we considered, the temperature profile approximates the profile of index difference. A comparison with the sech^2 profile in Fig. 3 has shown good agreement at 20 nsec. However, unlike the carrier concentration profile, the spatial distribution of the temperature spreads with time, i.e. the confining structure broadens with respect to the gain region.

Fig. 28: Temperature profile as a function of time from the start of the pumping pulse. T is evaluated for E = 30 kV, J = .1 Acm^{-2}, C = 1.05 $Jcm^{-3}{}^{o}K^{-1}$, k = 2.4 $Wcm^{-1}{}^{o}K^{-1}$ (see Ref. [44]).

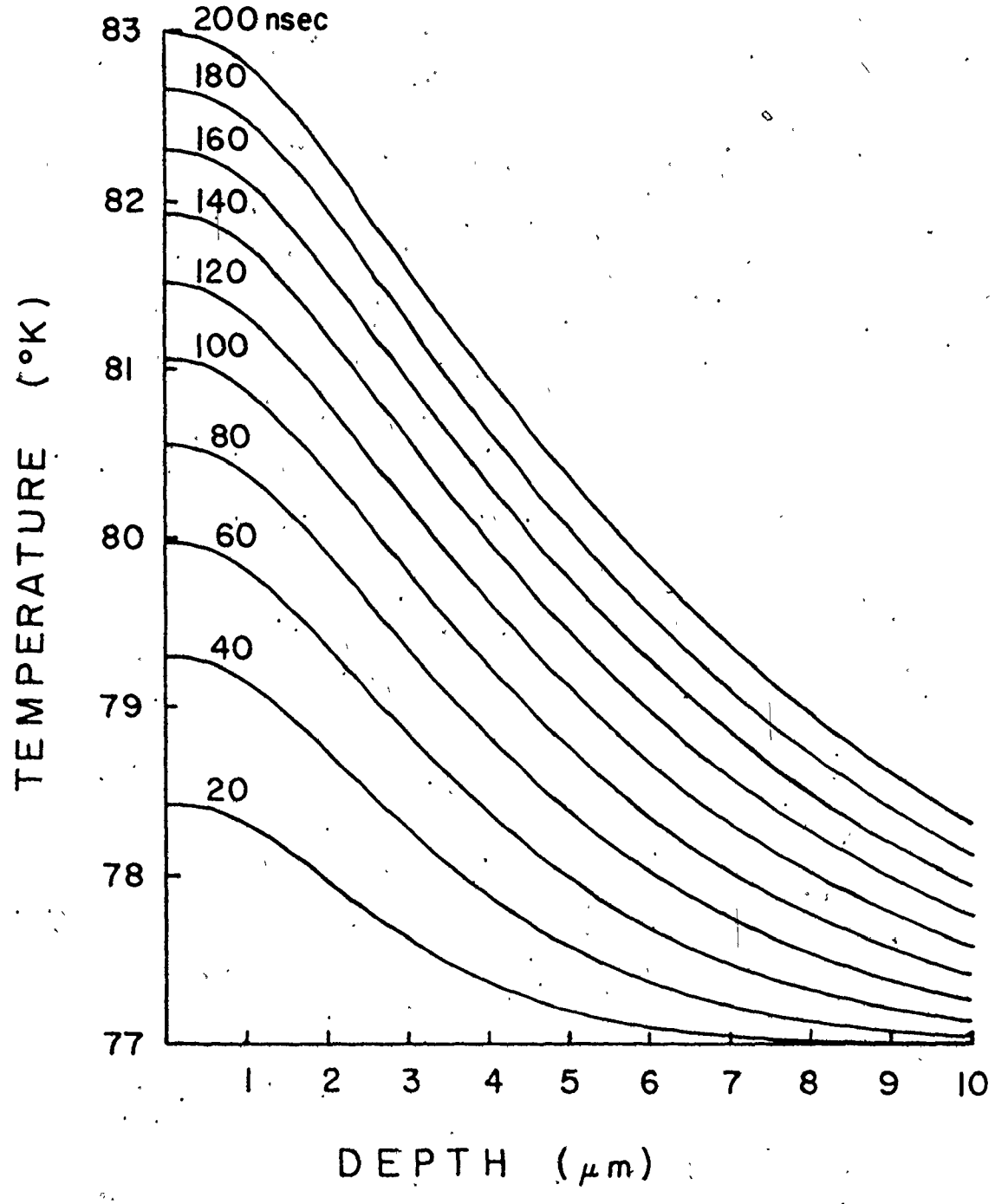
200 nsec
180
160
140
120
100
80
60
40
20
83
82
81
80
79
78
77
TEMPERATURE (°K)
1
2
3
4
5
6
7
8
9
10
DEPTH (μm)

Maxwell's equation has not been solved for such a combination of diverging spatial distributions of the permittivity but a slight increase in threshold carrier concentration (compared to the fixed profile calculation) is expected as a result of two competing effects. More gain will be required to fill the optical cavity which is widening with respect to the steady-state carrier concentration profile. This will be somewhat compensated by a reduction in diffraction loss.

APPENDIX B

CARRIER CONCENTRATION PROFILE

To evaluate the carrier concentration profile we seek a solution to the following carrier transport problem. Electron-hole pairs are generated at a constant rate g(x) within a semi-infinite one-dimensional semiconductor ($0 \leq x \leq \infty$). Surface states at the boundary x = 0 act as recombination centres. In this case, a steady-state solution is justified since the carrier lifetime is much shorter than the time delays of interest. Accordingly, the above problem can be expressed mathematically by the steady-state continuity equation (neglecting electric field effects),

$$D \frac{\delta^2 N}{\delta x^2} + g(x) - \frac{N}{\tau} = 0 \quad ,$$

subject to the boundary condition,

$$D \frac{\delta N}{\delta x} \Big|_{x=0} = s \cdot N(0) \quad .$$

N is the excess carrier density, D the diffusion coefficient, τ the lifetime, and s the surface recombination velocity.

The steady-state solution to the above equation is [45]

$$N(x) = \frac{\tau}{2L} \int_0^\infty g(x')\{\exp(-\frac{|x - x'|}{L}) + \sigma\exp(-\frac{x + x'}{L})\}\, dx' \quad , \tag{B.1}$$

where $\sigma = (1 - s\tau L^{-1})/(1 + s\tau L^{-1})$ and use is made of the relation $L = (D\tau)^{1/2}$. The distribution of carrier generation with depth is assumed to take the following form [28]

$$g(x) = \frac{J}{3eE_g} \times \frac{E}{R_B} \frac{\mu R_B}{4} (1 + \mu|a - x|)\exp(-\mu|a - x|) \quad ,$$

where E_g is the bandgap energy ($\approx$1.5 eV), e is the electronic charge, and the remaining parameters are as defined in Appendix A. After substitution in (B.1), an integration over x' yields,

$$N(x) = \frac{J}{3eE_g} \frac{E}{R_B} \frac{\mu R_B}{4} \tau \{2\mu^3L^3(\mu^2L^2 - 1)^{-2} [\exp(-\frac{|a - x|}{L}) + \sigma\exp(-\frac{a + x}{L})] - (\mu^2L^2 - 1)^{-2} [(1 + \mu|a - x|)(\mu^2L^2 - 1) + 2\mu^2L^2] \exp(-\mu|a - x|) - \frac{1}{2} [\frac{\sigma}{\mu L - 1} (1 + \mu a + \frac{\mu L}{\mu L - 1}) + \frac{1}{\mu L + 1} (1 + \mu a + \frac{\mu L}{\mu L + 1})] \exp(-\frac{x}{L} - \mu a)\} \quad .$$

This steady-state solution for the minority carrier concentration profile is shown in Fig. 29 for $J = 1\ Acm^{-2}$ and three values of the electron beam voltage.

Fig. 29: Steady-state distribution of the minority carriers at a current density of 1 Acm^{-2} for three values of the electron beam voltage (τ = 1 nsec, L = 1 μm, s = 1 x 10^6 cm sec^{-1}).

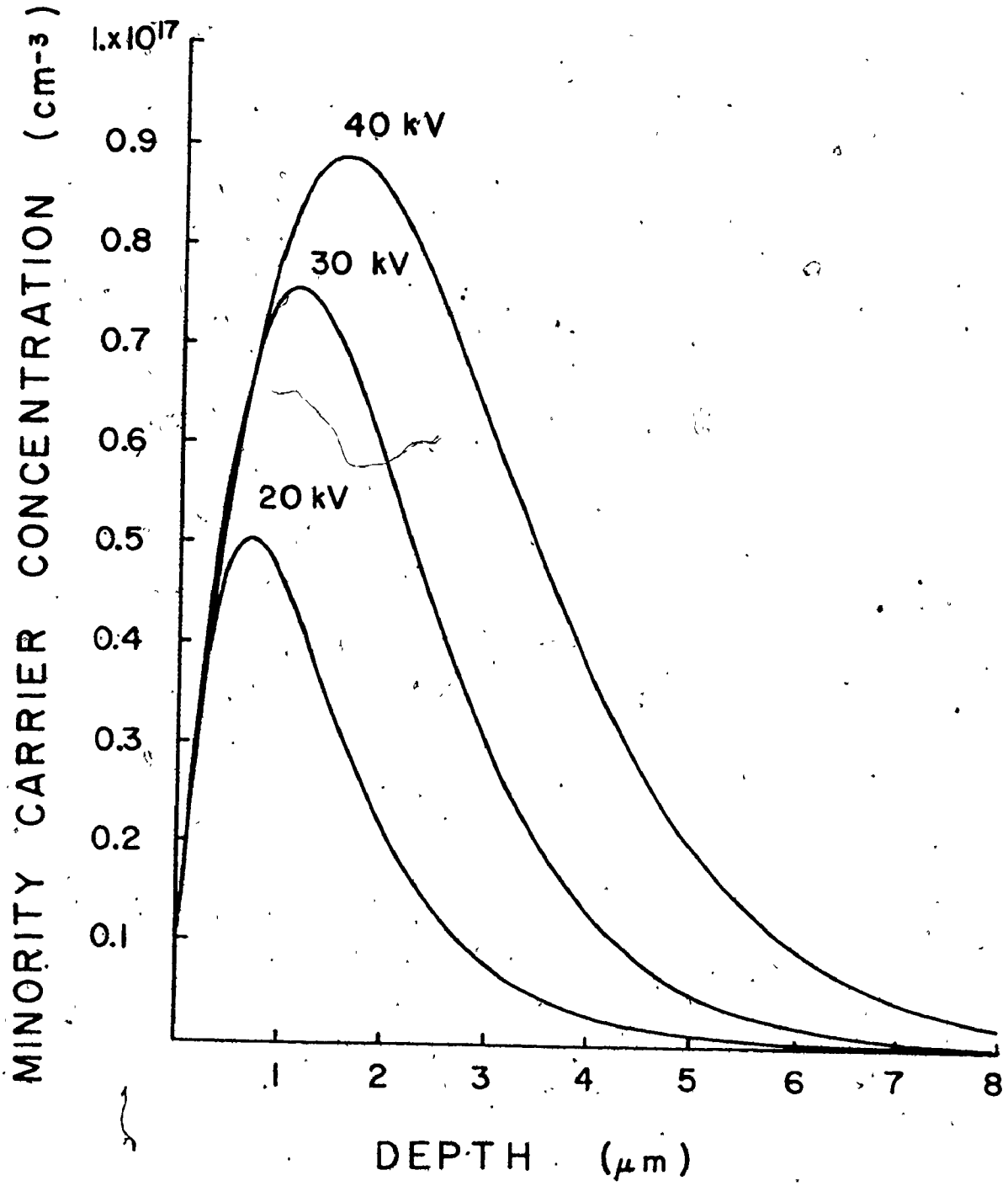
MINORITY CARRIER CONCENTRATION (cm-3)
1.x10^17
0.9
0.8
0.7
0.6
0.5
0.4
0.3
0.2
0.1
40 kV
30 kV
20 kV
1
2
3
4
5
6
7
8
DEPTH (μm)

APPENDIX C

TRANSVERSE MODE SOLUTION FOR THE SECH^2 PROFILE

The calculation of the time delay to lasing threshold is based on the evaluation of the diffraction losses in a semiconductor cavity. Under electron beam pumping, the complex permittivity varies with depth, i.e.

$$\varepsilon(x) = \begin{cases} \varepsilon_o' + \delta\varepsilon(x) + i\,\varepsilon_o'' - i\,\varepsilon''(x) & x \geq 0 \\ 1 & x < 0 \end{cases}$$

where ε_o' is the relative dielectric permittivity of the unexcited material, $\delta\varepsilon(x)$ and $\varepsilon''(x)$ describe respectively the spatial variation of the refractive index and the gain (or absorption) due to band-to-band transitions while the fixed losses in the cavity such as mirror distributed loss and free carrier absorption are included in ε_o''.

The electromagnetic field in the cavity can be represented by the function

$$E(x,z,t) = A(x,t)\,\sin\frac{\pi N z}{\ell}\,e^{-i\omega t}$$

This describes a field of oscillating frequency ω which already complies with the boundary conditions E = 0 at each extremity of the cavity of length ℓ. This function must satisfy the wave equation, that is

$$\frac{\partial A}{\partial t} = \frac{\omega}{2}\left\{\frac{i}{k^2}\frac{\partial^2 A}{\partial x^2} + \frac{\epsilon''(x) - \epsilon_o'' + i\,\delta\epsilon(x)}{\epsilon_o'} A\right\} \qquad (C.1)$$

where $k = \pi N/\ell = \omega\sqrt{\epsilon_o'}/c$ and c is the velocity of light in vacuo. The function A, the time-dependent distribution of the field amplitude along the x direction, is assumed to vary slowly in space and time compared to the wavelength and period of the radiation. An appropriate trial solution takes the form

$$A(x,t) = U(x)\, e^{-i\Omega t}$$

which, upon substitution in (C.1), gives

$$\frac{\partial^2 U}{\partial x^2} + \left(\frac{\omega}{c}\right)^2 \left\{i\,\epsilon_o'' - i\,\epsilon''(x) + \delta\epsilon(x) + 2\,\frac{\Omega\epsilon_o'}{\omega}\right\} U = 0 \qquad (C.2)$$

A profile of the form $\mathrm{sech}^2\, px$, suggested by Bogdankevich [31], approximates the spatial variations of the minority carrier concentration and the temperature. Assuming that the imaginary part of the permittivity follows the same profile, we write

$$\epsilon''(x) = (\epsilon_m'' + \epsilon_\infty'')\,\mathrm{sech}^2\, px - \epsilon_\infty''$$

where ϵ_m'' describes the gain at the semiconductor surface produced by the large electron-hole pair concentration, ϵ_∞'' represents the band-to-band absorption in the passive material at the lasing frequency and

$$p = (2d)^{-1} \ln\,(3 + 2\sqrt{2})$$

The parameter d is the depth at which the distribution is down to half of its maximum value. The spatial variation of the real part of the permittivity is related to the change in permittivity at the surface $\delta\epsilon_o$ by

$$\delta\epsilon(x) = \delta\epsilon_o \operatorname{sech}^2 px$$

Therefore, (C.2) becomes

$$\frac{\partial^2 U}{\partial (px)^2} + \left\{\frac{k^2}{p^2\epsilon_o}\left[\frac{2\Omega\epsilon_o'}{\omega} + i(\epsilon_o'' + \epsilon_\infty'')\right] - \frac{k^2}{p^2\epsilon_o}\left[-\delta\epsilon_o + i(\epsilon_m'' + \epsilon_\infty'')\right]\operatorname{sech}^2 px\right\}$$

$$U = 0$$

The solution to this equation is the hypergeometric equation [46].

$$U(x) = \cosh^{-K} px \; F\left(K + \tfrac{1}{2} + P, K + \tfrac{1}{2} - P \middle| K + 1 \middle| \tfrac{1}{2}(1 - \tanh px)\right)$$

where

$$K^2 = -\frac{k^2}{p^2\epsilon_o}\left[\frac{2\Omega\epsilon_o'}{\omega} + i(\epsilon_o'' + \epsilon_\infty'')\right]$$

$$P^2 - \frac{1}{4} = -\frac{k^2}{p^2\epsilon_o}\left[-\delta\epsilon_o + i(\epsilon_m'' + \epsilon_\infty'')\right]$$

For the solutions to stay finite as $x \to \infty$, the following condition must be satisifed.

$$K + \tfrac{1}{2} - P = -n \quad (n = 0, 1, 2 \ldots < P - \tfrac{1}{2}) \qquad (C.3)$$

Only odd values of n are allowed since the field solution must satisfy the boundary condition U(x=0) = 0.

The imaginary part of this relation is

$$\frac{2\Omega''}{\omega} = \frac{\varepsilon_m'' - \varepsilon_o''}{\varepsilon_o'} - \frac{3}{2}\frac{p^2}{k^2}\left\{\frac{1}{2}\left[\left(1 + \frac{4k^2}{p^2}\frac{\delta\varepsilon_o}{\varepsilon_o'}\right)^2 + \left(4\frac{k^2}{p^2}\frac{(\varepsilon_m''+\varepsilon_\infty'')}{\varepsilon_o'}\right)^2\right]^{1/2} - \frac{1}{2}\left(1 + \frac{4k^2}{p^2}\frac{\delta\varepsilon_o}{\varepsilon_o'}\right)\right\}^{1/2}$$

where Ω'' governs the increment or decrement of the radiation amplitude. In principle, at lasing threshold, the gain equals the losses. Setting $\Omega'' = 0$ therefore yields the relation between ε_m'' and the other optical parameters such that the gain necessary to satisfy the threshold condition can be evaluated. As in Chapter 4, it is convenient to write this relation in terms of normalized parameters. In analogy with (4.17), let

$$G = \frac{k^2}{p^2\varepsilon_o'}(\varepsilon_m'' - \varepsilon_o'') = \frac{2\pi n(.88d)^2}{\lambda_o}(\alpha_g - \alpha_o)$$

$$Q = \frac{k^2}{p^2\varepsilon_o'}(\varepsilon_\infty'' + \varepsilon_o'') = \frac{2\pi n(.88d)^2}{\lambda_o}(\alpha_s + \alpha_o)$$

$$R = \frac{k^2}{p^2\varepsilon_o'}\delta\varepsilon = \frac{\omega^2(.88d)^2}{c^2}\delta\varepsilon .$$

The lasing condition becomes

$$G = \frac{3}{2}\left\{\frac{1}{2}\left[(1+4R)^2 + 16(G+Q)^2\right]^{1/2} - \frac{1}{2}(1+4R)\right\}^{1/2} .$$

The dependence of G on R and Q has been illustrated in Fig. 18.

Finally, if (C.3) is obeyed, the hypergeometric function takes the form of a polynomial and, in particular, for the lowest-loss mode (n=1), the solution is written

$$U(x) = \cosh^{-p+\frac{3}{2}} px \tanh px$$

APPENDIX D

TRANSVERSE MODE SOLUTION TO THE STEP MODEL FOR A LASER CAVITY OF SEMI-INFINITE THICKNESS

Consider a bulk semiconductor sample excited by an electron beam. Assume that the high-energy electrons create a layer of uniform gain down to a depth d beyond which the crystal, which extends to infinity in this direction, remains unexcited [15]. The sample is bounded along the z-axis by two parallel cleaved edges. This cavity is similar to the optical structure analyzed at the beginning of Chapter 4 except that the radiation is now allowed to spread to infinity in the x-direction. The transverse mode solution will therefore be similar except that the boundary condition $A(L) = 0$ now becomes

$$A(x) \to 0 \quad \text{as} \quad x \to \infty \tag{D.1}$$

The appropriate form for the trial solution is

$$A(x) = \sin px \qquad 0 \leq x \leq d \tag{D.2}$$

$$A(x) = C \exp(-iqx) \qquad x > d \tag{D.3}$$

Substitution in the wave equation (4.13) gives

$$-p^2 = \left(\beta^2 - \frac{\omega^2}{c^2}\,\epsilon_o'\right) - i\,\frac{\omega^2}{c^2}\,(\epsilon_g'' - \epsilon_o'') - \frac{\omega^2}{c^2}\,\delta\epsilon$$

$$-q^2 = \left(\beta^2 - \frac{\omega^2}{c^2}\,\epsilon_o'\right) + i\,\frac{\omega^2}{c^2}\,(\epsilon_\ell'' + \epsilon_o'')$$

with the following boundary condition on the field and its derivative at $x = d$

$$\sin pd = C \exp(-iqd)$$

$$p = -iq \tan pd$$

Make the following substitution

$$pd = u + i\,k$$

$$qd = v + i\,s$$

and introduce the normalized parameters G, Q, R, Δ defined by (4.17c) to (4.17f) for the gain, the passive loss, the refractive index step and the change in the propagation constant. Separating real and imaginary parts leads to

$$u^2 - k^2 = \Delta + R \tag{D.4}$$

$$2ku = G \tag{D.5}$$

$$v^2 - s^2 = \Delta \tag{D.6}$$

$$2sv = -Q \tag{D.7}$$

for the wave equation in the two regions and

$$\frac{uv + ks}{v^2 + s^2} = \frac{\sinh 2k}{2(\cosh^2 k - \sin^2 u)} \tag{D.8}$$

$$\frac{kv - us}{v^2 + s^2} = \frac{-\sin 2u}{2(\cosh^2 k - \sin^2 u)} \tag{D.9}$$

for the boundary condition on the field derivative at $x = d$. (D.4) to (D.7) can be used to express v and s in terms of u and k

$$v = \left\{\tfrac{1}{2}\left[\left((u^2 - k^2 - R)^2 + Q^2\right)^{1/2} + u^2 - k^2 - R\right]\right\}^{1/2}$$

$$s = -\left\{\frac{1}{2}\left[\left((u^2 - k^2 - R)^2 + Q^2\right)^{1/2} - (u^2 - k^2 - R)\right]\right\}^{1/2}$$

A sign ambiguity arises for each square root. The positive sign must be chosen for the innermost square root because v was defined as a real number. From the solution of v and s in terms of u and k, it follows that the positive sign must be chosen also for the innermost square root in s. The negative sign of s is required to avoid a contradiction between (D.3) and (D.1). Since (D.7) specifies that v and s are of opposite sign, v must therefore be positive.

(D.8) and (D.9) form a system of two equations which is solved numerically for u and k. The solution pairs are used to calculate the gain required for lasing threshold $\alpha_g = 2ku(\lambda/2\pi nd^2) + \alpha_o$, and the transverse field distribution for various combinations of the cavity parameters: absorption in the passive region, refractive index step and thickness of the active region.

APPENDIX E

DERIVATION OF EXPRESSION FOR FAR-FIELD DIFFRACTION PATTERN

In the Fraunhofer approximation, the far-field diffraction pattern for a source E(x) is

$$E'(\theta) = \int_{-\infty}^{\infty} E(x)\, e^{i\gamma x}\, dx$$

where

$$\gamma = (2\pi/\lambda) \sin \theta.$$

For the resonator of semi-infinite thickness, the analytic integration of the above expression using the near-field distribution of (D.2) and (D.3) yields.

$$E'(\theta) = \frac{p}{p^2 - \gamma^2} + \left[\left(\frac{i\gamma}{p^2 - \gamma^2} + \frac{i}{\gamma - q}\right)\sin pd - \frac{p \cos pd}{p^2 - \gamma^2}\right]\exp(i\gamma d)$$

Similarly, for a finite cavity, the near-field distribution is given by (4.15) and leads to the following expression for the far field.

$$E'(\theta) = \frac{p}{p^2 - \gamma^2} - \frac{q \sin pd \exp(i\gamma L)}{(q^2 - \gamma^2) \sin q(d - L)} + (i\gamma \sin pd - p \cos pd)$$

$$\left[\frac{1}{p^2 - \gamma^2} - \frac{1}{q^2 - \gamma^2}\right] \exp(i\gamma d)$$

REFERENCES

[1] R.N. Hall, G.E. Fenner, J.D. Kingsley, T.J. Soltys and R.O. Carlson, Phys. Rev. Lett. 9, 366 (1962).

[2] M.I. Nathan, W.P. Dumke, G. Burns, F.H. Dill Jr., and G.J. Lasher, Appl. Phys. Lett. 1, 62 (1962).

[3] T.M. Quist, R.H. Rediker, R.J. Keyes, W.E. Krag, B. Lax, A.L. McWhorter and H.J. Ziegler, Appl. Phys. Lett. 1, 91 (1962).

[4] H. Nelson, J.I. Pankove, F. Hawrylo, G.C. Doumanis and C. Reno, Proc. IEEE 52, 1360 (1964).

[5] M.H. Pilkuhn and H. Rupprecht, J. Appl. Phys. 38, 5 (1967).

[6] I. Hayashi, M.B. Panish and P.W. Foy, IEEE J. Quant. Electron. QE-5, 211 (1969).

[7] H. Kressel and H. Nelson, RCA Rev. 30, 106 (1969).

[8] Z.I. Alferov, V.M. Andreev, D.Z. Garbuzov et al., Sov. Phys.-Semicond. 4, 1573 (1971).

[9] M.B. Panish, S. Sumski and I. Hayashi, Metallurg. Trans. 2, 795 (1971).

[10] M. Ettenberg and H. Kressel, 1975 Intern'l Electron Devices Meeting (Technical Digest) Washington 1-3 Dec. 1975 (New York 1975), pp. 487-489.

[11] T. Gonda, H. Junker and M.F. Lamorte, IEEE J. Quant. Electron. QE-1, 159 (1965).

[12] J. Shewchun, B.S. Kawasaki and B.K. Garside, IEEE J. Quant. Electron. QE-6, 133 (1970).

[13] B.K. Garside, J. Shewchun and B.S. Kawasaki, IEEE J. Quant. Electron. QE-7, 88 (1971).

[14] A. Masuyama, M. Kawabe, K. Masuda and S. Namba, IEEE J. Quant. Electron. QE-9, 324 (1973).

[15] B.K. Garside, J. Shewchun and B.S. Kawasaki, J. Appl. Phys. 43, 4050 (1972).

[16] S.J. Chua and B. Thomas, IEEE J. Quant. Electron. QE-13,652 (1977).

[17] K. Konnerth, Presented at the Solid-State Devices Research Conf., Princeton, N.J., June 21-23, 1965 (Abstract in IEEE Trans. Electron. Devices, ED-12, 506 (1965).

[18] J.C. Dyment and J.E. Ripper, IEEE J. Quant. Electron. QE-4, 155, (1968).

[19] J.I. Pankove, IEEE J. Quant. Electron. QE-4, 161 (1968).

[20] L.N. Kurbatov, V.I. Molochev, V.V. Nikitin and A.I. Sharin, Sov. J. Quant. Electron. 1, 655, (1972).

[21] M.J. Adams, S. Grundorfer, B. Thomas, C.F.L. Davies and D. Mistry, IEEE J. Quant. Electron. QE-9, 328 (1973).

[22] H. Aritome, K. Masuda and S. Namba, Japan. J. Appl. Phys. 9, 579 (1970).

[23] M. Kawabe, A. Masuyama, K. Aoki, K. Masuda and S. Namba, Japan. J. Appl. Phys. 9, 850 (1970).

[24] J.C. Dyment, J.E. Ripper and T.P. Lee, J. Appl. Phys. 43, 452 (1972).

[25] G.A. Acket, W. Nijman and H. Lam, J. Appl. Phys. 45, 3033 (1974).

[26] M. Ettenberg and C.J. Nuese, J. Appl. Phys. 46, 3500 (1975).

[27] J. Vilms and W.E. Spicer, J. Appl. Phys. 36, 2815 (1965).

[28] C.A. Klein, Applied Optics 5, 1922 (1966).

[29] M.N. Ozisik, Boundary Value Problems of Heat Conduction (International Textbook, Scranton, 1968) p. 75.

[30] G. Lasher and F. Stern, Phys. Rev. 133, A553 (1964).

[31] O.V. Bogdankevich, V.S. Letokhov and A.F. Suchkov, Sov. Phys.-Semicond. 3, 566, (1969).

[32] F. Stern, Phys. Rev. 133, A1653 (1964).

[33] D.T.F. Marple, J. Appl. Phys. 35, 1241 (1964).

[34] B.O. Seraphin and H.E. Bennett, Semiconductors and Semimetals, Edited by R.K. Willardson and A.C. Beer (Academic, London, 1967), Vol. 3, p. 499.

[35] D.E. Hill, Phys. Rev. 133, A866 (1964).

[36] B.S. Kawasaki, Electron-Beam-Pumped Semiconductor Lasers, Ph.D. Thesis, McMaster University, Hamilton, 1972.

[37] K.L. Ashley, D.L. Carr and R. Romano-Moran, Appl. Phys. Lett. 22, 23 (1973).

[38] R.E. Enstrom, P.J. Zanzucchi and J.R. Appert, J. Appl. Phys. 45, 300 (1974).

[39] F.D. Nunes, N.B. Patel and J.E. Ripper, IEEE J. Quant. Electron. QE-13, 675 (1977).

[40] O.V. Bogdankevich, V.A. Goncharov, B.M. Lavrushin, V.S. Letokhov and A.F. Suchkov, Sov. Phys.-Semicond. 1, 4 (1967).

[41] M.J. Adams and M. Cross, Electron. Lett. 7, 569 (1971).

[42] B.S. Kawasaki, B.K. Garside and J. Shewchun, Appl. Phys. Lett. 21, 477 (1972).

[43] T. Harrett, Solid-State Electron. 13, 388 (1970).

[44] W. Engeler and M. Garfinkel, Solid-State Electron. 8, 585 (1965).

[45] W. van Roosbroeck, J. Appl. Phys. 26, 380 (1955).

[46] P.M. Morse and H. Feshbach, Methods of Theoretical Physics, (McGraw-Hill, New York, 1953), Chap. 5, and p. 768.